

High-Performance Nanomaterials as Phosphors for Light-Emitting Diodes

Guest Editors: Su Chen, Jian Xu, Yongsheng Wang, and Katsumi Kishino





High-Performance Nanomaterials as Phosphors for Light-Emitting Diodes

Journal of Nanomaterials

High-Performance Nanomaterials as Phosphors for Light-Emitting Diodes

Guest Editors: Su Chen, Jian Xu, Yongsheng Wang,
and Katsumi Kishino



Copyright © 2013 Hindawi Publishing Corporation. All rights reserved.

This is a special issue published in "Journal of Nanomaterials." All articles are open access articles distributed under the Creative Commons Attribution License, which permits unrestricted use, distribution, and reproduction in any medium, provided the original work is properly cited.

Editorial Board

- | | | |
|--------------------------------|----------------------------------|------------------------------|
| Katerina E. Aifantis, USA | Do K. Kim, Korea | Titipun Thongtem, Thailand |
| Nageh K. Allam, USA | Alan K. T. Lau, Hong Kong | Somchai Thongtem, Thailand |
| Margarida Amaral, Portugal | Burtrand Lee, USA | Alexander Tolmachev, Ukraine |
| Xuedong Bai, China | Jun Li, Singapore | Valeri P. Tolstoy, Russia |
| Lavinia Balan, France | Benxia Li, China | Tsung-Yen Tsai, Taiwan |
| Enrico Bergamaschi, Italy | Xing-Jie Liang, China | Takuya Tsuzuki, Australia |
| Theodorian Borca-Tasciuc, USA | Shijun Liao, China | Raquel Verdejo, Spain |
| C. Jeffrey Brinker, USA | Gong-Ru Lin, Taiwan | Mat U. Wahit, Malaysia |
| Christian Brosseau, France | Tianxi Liu, China | Zhenbo Wang, China |
| Xuebo Cao, China | Jun Liu, USA | Ruibing Wang, Canada |
| Shaiful Chowdhury, USA | Songwei Lu, USA | Shiren Wang, USA |
| Kwang-Leong Choy, UK | Daniel Lu, China | Cheng Wang, China |
| Cui ChunXiang, China | Jue Lu, USA | Yong Wang, USA |
| Miguel A. Correa-Duarte, Spain | Ed Ma, USA | Jinquan Wei, China |
| Shadi A. Dayeh, USA | Gaurav Mago, USA | Ching-Ping Wong, Hong Kong |
| Ali Eftekhari, USA | Santanu K. Maiti, India | Xingcai Wu, China |
| Claude Estournés, France | Sanjay R. Mathur, Germany | Guodong Xia, Hong Kong |
| Alan Fuchs, USA | Vikas Mittal, UAE | Ping Xiao, UK |
| Lian Gao, China | Weihai Ni, Germany | Zhi Li Xiao, USA |
| Russell E. Gorga, USA | Sherine Obare, USA | Yangchuan Xing, USA |
| Hongchen Chen Gu, China | Atsuto Okamoto, Japan | Shuangxi Xing, China |
| Mustafa O. Guler, Turkey | Abdelwahab Omri, Canada | Nanping Xu, China |
| John Z. Guo, USA | Edward A. Payzant, USA | Doron Yadlovker, Israel |
| Smrati Gupta, Germany | Kui-Qing Peng, China | Yingkui Yang, China |
| Michael Harris, USA | Anukorn Phuruangrat, Thailand | Khaled Youssef, USA |
| Zhongkui Hong, China | Mahendra Rai, India | Kui Yu, Canada |
| Michael Z. Hu, USA | Suprakas Sinha Ray, South Africa | William W. Yu, USA |
| David Hui, USA | Ugur Serincan, Turkey | Haibo Zeng, China |
| Y.-K. Jeong, Republic of Korea | Huaiyu Shao, Japan | Tianyou Zhai, China |
| Sheng-Rui Jian, Taiwan | Donglu Shi, USA | Renyun Zhang, Sweden |
| Wanqin Jin, China | Vladimir Sivakov, Germany | Bin Zhang, China |
| Rakesh K. Joshi, UK | Marinella Striccoli, Italy | Yanbao Zhao, China |
| Zhenhui Kang, China | Bohua Sun, South Africa | Lianxi Zheng, Singapore |
| Fathallah Karimzadeh, Iran | Saikat Talapatra, USA | Chunyi Zhi, Hong Kong |
| Alireza Khataee, Iran | Nairong Tao, China | |

Contents

Recent Advances in Stimuli-Responsive Photofunctional Materials Based on Accommodation of Chromophore into Layered Double Hydroxide Nanogallery, Wu Li, Dongpeng Yan, Rui Gao, Jun Lu, Min Wei, and Xue Duan
Volume 2013, Article ID 586462, 14 pages

Influence of Different Carboxylic Acid Ligands on Luminescent Properties of Eu(Lc)₃phen (Lc = MAA, AA, BA, SA) Complexes, Jing Zhang, Le Zhang, Yan Chen, Xiaogu Huang, Lixi Wang, and Qitu Zhang
Volume 2013, Article ID 768535, 8 pages

Concentration Dependence of Luminescent Properties for Sr₂TiO₄:Eu³⁺ Red Phosphor and Its Charge Compensation, Zhou Lu, Le Zhang, Lixi Wang, and Qitu Zhang
Volume 2012, Article ID 698434, 7 pages

Study on Pore Distribution and Formation Rule of Sepiolite Mineral Nanomaterials, Qingguo Tang, Fei Wang, Mengran Tang, Jinsheng Liang, and Chongyan Ren
Volume 2012, Article ID 382603, 6 pages

An Investigation of Electronic Structure and Aromaticity in Medium-Sized Nanoclusters of Gold-Doped Germanium, Xiao-Jun Li, Hong-Jiang Ren, and Li-Ming Yang
Volume 2012, Article ID 518593, 8 pages

Effective Red Compensation of Sr₂SiO₄ : Dy³⁺ Phosphor by Codoping Mn²⁺ Ions and Its Energy Transfer, Le Zhang, Zhou Lu, Pengde Han, Lixi Wang, and Qitu Zhang
Volume 2012, Article ID 848274, 7 pages

Review Article

Recent Advances in Stimuli-Responsive Photofunctional Materials Based on Accommodation of Chromophore into Layered Double Hydroxide Nanogallery

Wu Li, Dongpeng Yan, Rui Gao, Jun Lu, Min Wei, and Xue Duan

State Key Laboratory of Chemical Resource Engineering, Beijing University of Chemical Technology, Beijing 100029, China

Correspondence should be addressed to Dongpeng Yan; yandongpeng001@163.com

Received 29 October 2012; Accepted 27 December 2012

Academic Editor: Su Chen

Copyright © 2013 Wu Li et al. This is an open access article distributed under the Creative Commons Attribution License, which permits unrestricted use, distribution, and reproduction in any medium, provided the original work is properly cited.

The assembly of photofunctional molecules into host matrices has become an important strategy to achieve tunable fluorescence and to develop intelligent materials. The stimuli-responsive photofunctional materials based on chromophores-assembled layered double hydroxides (LDHs) have received much attention from both academic and industry fields as a result of their advantages, such as high photo/thermal stability, easy processing, and well reversibility, which can construct new types of smart luminescent nanomaterials (e.g., ultrathin film and nanocomposite) for sensor and switch applications. In this paper, external environmental stimuli have mainly involved physical (such as temperature, pressure, light, and electricity) and chemical factors (such as pH and metal ion); recent progress on the LDH-based organic-inorganic stimuli-responsive materials has been summarized. Moreover, perspectives on further development of these materials are also discussed.

1. Introduction

The functional material that can respond to different external stimuli is the basis for developing a new generation of intelligent device. Stimuli-responsive organic photofunctional (such as luminescent) materials have attracted significant attention from both fundamental research as well as industry during the last few years, because of their remarkable and sensitive response signal. These photofunctional materials have potential applications in the fields of fluorescent switches and optical recording sensors [1]. Generally, the mechanisms for changing in photofunction of organic materials consist of occurrence of chemical reactions and alteration of the molecular packing mode [2, 3]. Recently, controlling and tuning the molecular packing mode become a main strategy for the design of intelligent luminescent materials, because the solid-state chemical reaction frequently involves relatively low conversion efficiency. Since 2005, several new types of organic luminescent materials with stimuli-responsive properties (such as piezochromic, deformation-induced chromic, photochromic, thermochromic, and humidity colorimetric luminescent systems) have been developed [4–7]. However,

to meet the requirements of responsive luminescent devices or optical sensors, the assembly of ordered thin films with the chromophores on two-dimensional (2D) surfaces remains a challenge, and examples are rather rare.

For an idealized orderly system, the photoactive molecules with regular molecular orientation and intermolecular packing mode are more prone to exhibit systematically responsive behaviors upon external stimuli. Therefore, the control of high orientation of organic molecules is of critical importance to design and fabricate responsive luminescent materials. As well, from a perspective of luminescent efficiency, the aggregates of luminescent molecules are usually readily formed in the solid state, which can lead to an emission shift, line broadening, and even luminescence quenching. Moreover, the thermal/chemical stability and service lifetime of organic materials are generally low for optoelectronic device application [8]. Therefore, how to further enhance the optical performance and stability also became major goals. In addition, from a viewpoint of practical application, fast response, high reversibility, and stable repeatability are all necessary for such responsive materials as sensors and switches.

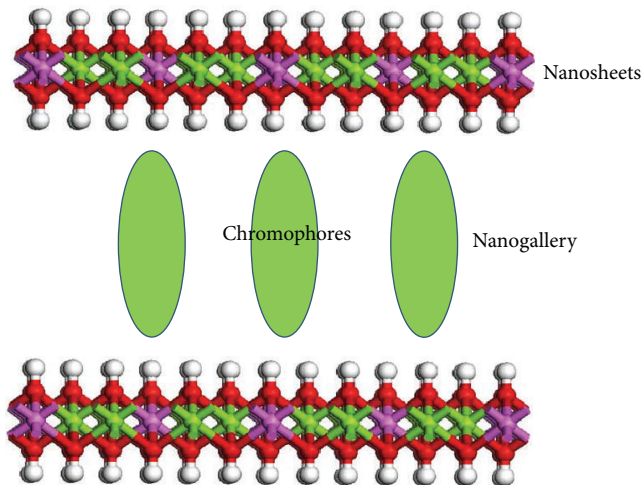


FIGURE 1: A typical scheme for chromophores assembled into Mg-Al-LDH nanogallery.

One effective way to realize the regulation and orientation of the organic chromophores is the incorporation of organic photofunctional molecules into solid host matrices, which can also supply a stable environment to enhance the thermo and photostabilities of organic species. In this sense, layered double hydroxides (LDHs) are typical layered host materials, which can be described by the general formula: $[M^{II}_{1-x}M^{III}_x(OH)_2]^{z+}A^{n-}_{z/n}\cdot yH_2O$ (M^{II} and M^{III} are divalent and trivalent metals ions, respectively; A^{n-} is an anion) [9]. The structure of the LDH layer is analogous to that of the brucite with edge-sharing $M(OH)_6$ octahedra, in which partial substitution of M^{3+} for M^{2+} induces positively charged host layers, balanced by the interlayer anions. Different from most of the cationic clays, the charge density and elemental composition of LDHs can be changed during the synthesis process, favoring finely controlling properties of the host layer. To meet the demands in applications, hundreds of suitable anions have been rationally chosen and intercalated into LDHs for constructing new types of host-guest nanomaterials [10].

The LDH features 2D channel at the nanometer level, and the nanogallery is usually in the range of 0.3–4 nm [11]; therefore, most of anionic organic photoactive guests can be incorporated into LDH hosts to obtain inorganic-organic hybrid nanomaterials (as shown in Figure 1). These systems show specific physical and chemical performances compared with their individual counterparts, which is beneficial for the fabrication of novel optoelectronic and photofunctional materials: (1) chromophore guest molecules immobilized in the LDH host matrix exhibit optical and thermal stability, environmental compatibility, and low operational risk [12]. (2) The orientation and arrangement of the chromophores can be tuned by changing the layer charge density and chemical composition, which can further adjust the optical properties of the nanocomposites [13, 14]. (3) LDH host matrix provides chromophore molecules with a confined and

stable environment, which reduces molecular thermal agitation (intermolecular collisions, vibrations, and rotations) by host-guest interactions, and the fluorescence quenching is therefore reduced [15, 16]. Recently, according to the principle of molecular design and supramolecular assembly, the inorganic-organic nanomaterials (both powders and thin films) based on the accommodation of chromophore guests into LDH host have been largely developed and have gradually become a fascinating field in luminescent hybrid materials [17, 18]. For example, the polyanion-assembled LDH films exhibit a better UV light resistance ability than the pure polyanion/polycation film. By the use of *in-situ* photoluminescence technique, [15] it was found that the normalized fluorescence intensity of the anionic poly(*p*-phenylene) (APPP) assembled LDH was larger than that of the APPP/PDDA (poly(dimethyldiallylammonium chloride)) counterpart, demonstrating that the presence of the inorganic LDH nanosheets leads to an enhanced optical stability of the conjugated anions compared with typical organic/organic films. A previous review on LDH-based fluorescent materials has mainly summarized the preparation method and tunable photoluminescent properties [19]. Recently, the host-guest stimuli-responsive luminescent materials have also been studied successively, since the orientation mode of the interlayer chromophores and host-guest interaction can be changed upon external stimuli [20, 21]. In addition, new physical/chemical phenomena have also been obtained based on the theoretical calculations for these hybrid nanomaterials. We believe it is timely and necessary to introduce these new advances to give a better understanding and supply new insights for the design of organic-inorganic intelligent nanomaterials. In this paper, we focus our attention on recent progress of the stimuli-responsive photofunctional materials for optical/luminescent switch and sensor applications by assembling photofunctional molecules into LDH nanogallery; by selecting representative stimuli-responsive examples, two types of environmental stimuli—physical stimuli (such as light, pressure, heat, electricity and polarization) and chemical stimuli (pH value and heavy metal ions)—were mainly introduced. Finally, perspectives on future development for these materials are also discussed.

2. LDH-Based Physical Stimuli-Responsive Materials

2.1. Heat- and Pressure-Responsive Materials. Temperature and pressure are the most common and natural environmental factors; therefore, temperature- and pressure-induced chromic (known as thermochromic and piezochromic) materials can be potentially used in memory chips and security inks. Stilbene-type compounds have attracted considerable interests due to their excellent optical and electronic properties [22, 23]. Yan et al. [24] have fabricated an inorganic-organic ultrathin film (UTF) system with thermochromic luminescence (TCL) based on the layer-by-layer (LBL) assembly of anionic stilbene derivative (bis(2-sulfonatostyryl)biphenyl, donated as BSB) and LDH nanosheets. The thickness of the BSB/LDH UTF can be

finely controlled in the range from 23 nm (8 bilayers) to 67 nm (32 bilayers), indicating that the average thickness of one BSB/LDH unit is about 2.2 nm. The UTF undergoes a remarkable change in luminescence color upon increasing temperature. On heating the BSB/LDH from 20 to 100°C, the emissive band moves from 444 to 473 nm with a gradual decrease in the luminescence intensity. The emission color changes from blue to bluish green on heating the UTF, and the color change is also visible to the naked eye as shown in the inset of Figure 2(a). When the UTF was cooled to 20°C over 2 min, the fluorescence emission can recover its original blue color completely together with the associated reverse spectral changes. The reversible change in luminescence color can also be repeated (Figure 2(a), inset). For the excited states of the UTF, the fluorescence decay at high temperature is slower than that at low temperature (Figure 2(b)), and this behavior can be assigned to the formation of an excimer in the UTF. The fluorescence lifetime of the UTFs at 100°C is 1.9 ns, about twice the value at 20°C (0.9 ns). These changes in fluorescence lifetime are repeatedly observed on cycling between two typical temperatures (Figure 2(b), inset).

In-situ FTIR measurement shows that, as the temperature increases, the most significant change is that the bands at 1652 and 1630 cm⁻¹ broaden and become unresolved for the UTF, suggesting that the skeleton vibration increases dramatically at high temperature and the system becomes relatively disordered compared with that at low temperature. No characteristic band disappears in the whole range, demonstrating no chemical reaction occurs during the heating process. Further molecular dynamic simulation confirms that the TCL performance is mainly associated with the variations in orientation and molecular packing of BSB confined between the LDH nanosheets. Based on TCL performance, it is anticipated that the UTFs can be potentially used as luminescent sensors and molecular thermometers.

The study on the reversible thermochromic materials has attracted more attention due to its wide applications such as optical data storage, security markers for notes and documents, and color-variable clothing [26]. 4-(4-anilinophenylazo)benzenesulfonate (AO5) is a typical azo dye with thermochromic property, which has been used as a thermal sensor, pH indicator, and molecular memory storage due to its tautomerism between the azo A form and hydrazone H form (Figure 3). Such tautomeric equilibrium is sensitive to the external microenvironment (e.g., substituents and solvents). An effective way to enhance the thermochromic performances of this dye is to choose a suitable host matrix for tuning its molecular environment. Wang et al. [25] have fabricated transparent thin films based on AO5 and sodium dodecylbenzene sulfonate (SDS) cointercalated in LDH, which show a fast and repeatable thermochromic behavior. By the use of temperature-dependent UV/visible absorption spectrophotometer, it was observed that the 10% AO5-LDH thin film shows the highest thermochromic efficiency.

At ambient temperature, the AO5-LDH thin film has a maximal absorption at 363 nm (Figure 4(a)). Upon increasing temperature, a spectral change occurs with a decrease in the intensity of the band at 363 nm, and a new band

appears with increasing intensity at 445 nm. Visually, a color change from light yellow to reddish orange can be observed upon heating the 10% AO5-LDH film from 35 to 65°C. As the film is cooled to 35°C, it recovers its original color with the associated converse spectral changes. Figure 4(b) shows the temperature-dependent absorbance at 445 nm over a complete heating-cooling cycle, confirming the reversibility of the thermochromic performance. Moreover, the film material also shows high thermostability and photostability as a result of the host-guest structure. As the temperature range for the thermochromism covers the body temperature of human beings and the atmosphere, it can be expected that this AO5-LDH film has potential applications in the field of physiological and environmental temperature designation and warning.

Conjugated polydiacetylenes (PDAs) have attracted great attention during the past few years, owing to their significant functionality and wide applicability in colorimetric detection systems [27, 28]. It is highly desirable to achieve sensor and array devices with high stability, reusability, and environmental compatibility by the immobilization of PDAs. Recently, Shi et al. [29] have prepared the 1,3-diacetylene (DA) anion-intercalated LDH nanocomposite films with the aid of a photolithography technique. UV irradiation of the colorless DA-LDH film results in the formation of patterned blue/colorless image (Figure 5(a) A, B). Heating the film at 130°C results in the transition to yellow/colorless patterned image, while it transfers to red/colorless patterned image as the film is cooled down (Figure 5(a) C, D). The heat-treatment at 130°C shows an orange-yellow/colorless fluorescence image, which displays a bluish green/colorless fluorescence image when the sample is cooled (Figure 5(b) C, D). For the corresponding film with physical mixture of PDA and LDH, no thermal response can be observed for optical image. By the analysis of *in-situ* Raman spectroscopy, the thermochromic behavior of PDAs/LDH is attributed to strong hydrogen bond interactions between LDH and PDAs.

To date, compared with those of temperature-sensitive materials, the study of piezochromic luminescence (PCL) materials remains in an early stage [30]. The design of PCL materials is of importance to monitor the change in pressure, especially under extreme conditions. It has been recognized that alternating the molecular arrangement mode is a promising strategy to tune the fluorescence of an organic compound. During last 10 years, efforts have been put in the development of pure organic fluorophores with PCL properties, and these materials usually involve an aggregation-induced emission mechanism [31, 32]. However, the rational design and preparation of organic-inorganic hybrid PCL materials remain a considerable challenge.

Recently, we have fabricated a new type of PCL material by the assembly of an organic fluorophore (2,2'-(1,2-ethenediyl)bis[5-[4-(diethylamino)-6-[(2,5-disulfophenyl)amino]-1,3,5-triazin-2-yl] amino] benzene sulfonate anion, BTZB) into the nanogalleries of LDHs [33]. Such strategy for construction of PCL material is based on the fact that the LDH nanosheets are flexible enough to deform over interlayer bulky guests, and slipping of LDH layer can occur

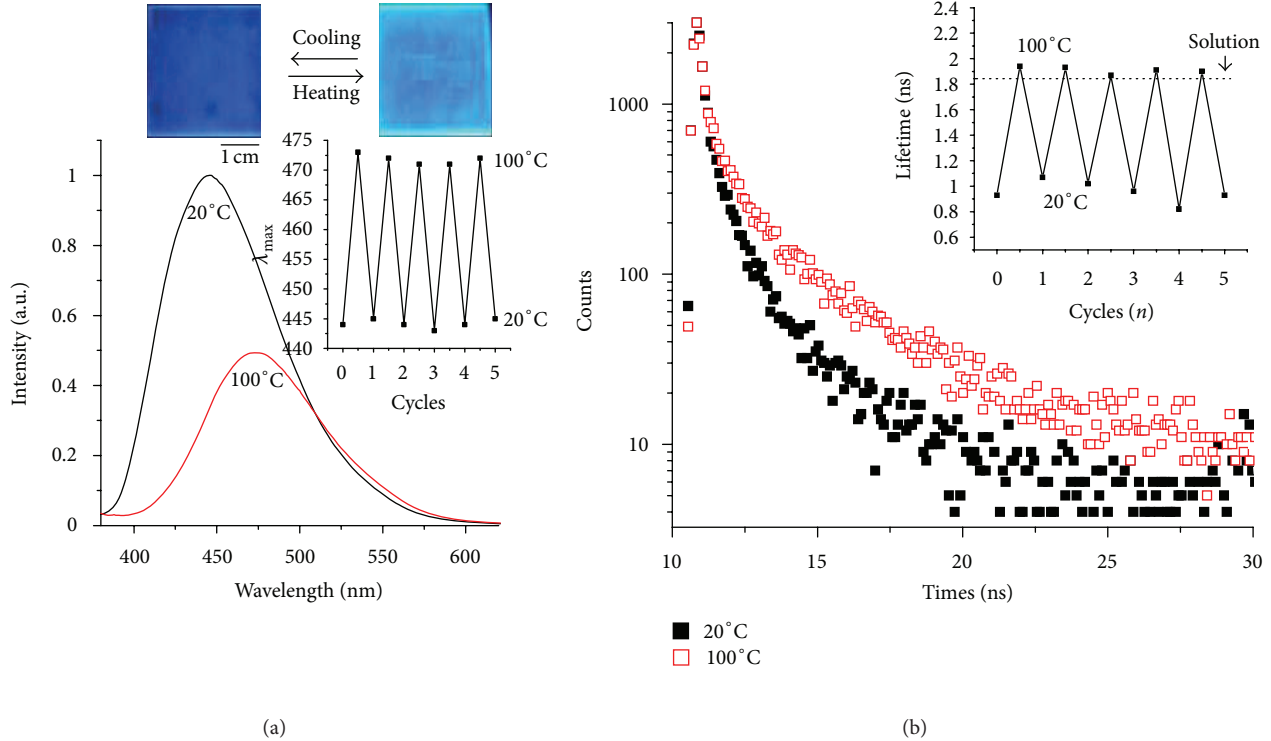


FIGURE 2: TCL of the BSB/LDH UTF at 20 and 100°C. (a) Fluorescence spectra (inset: the reversible fluorescence response over five consecutive cycles, and photographs of the UTF before and after heating). (b) Fluorescence decay curve (inset: fluorescence lifetimes over five consecutive cycles) [24].

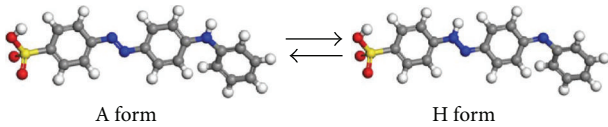


FIGURE 3: Tautomeric equilibrium between the A form and H form of AO5 [25].

on increasing the external pressure, which can further influence the host-guest interactions [21]. In addition, the long-chain BTZB anion has four rotatable aromatic amine units, and thus its molecular conformation and intermolecular interactions can be tuned more easily by external perturbations than the rigid molecules. Upon increasing pressure, BTZB/LDH nanocomposites exhibit luminescent redshift with a concomitant broadening of the emission, while the pristine BTZB shows no PCL at all. The most significant PCL behavior is present in the BTZB/Mg₂Al-LDH sample, and the maximum emissive wavelength moves from 452 to 515 nm under different stimuli (Figures 6(a) and 6(b)). The typical photographs of the BTZB/Mg₂Al-LDH pellet under UV light (Figure 6(a), inset) display a visual luminescent change from blue to green upon increasing pressure. The redshift of spectra may be attributed to the formation of J-type aggregates in the nanogallery of LDH. An appreciable change in the UV-vis absorption band of BTZB/Mg₂Al-LDH nanocomposites was also observed upon compression as shown in Figure 6(c).

Once the pressed BTZB/Mg₂Al-LDH sample was ground into powder, heated at 100°C, and then cooled down, the luminescent peak at 515 nm moved back to 452 nm completely. In addition, the reversible luminescent color change can be readily repeated to switch between two pressures. The reversible changes in fluorescence properties can be recycled at least 3 times. Therefore, it can be concluded that the BTZB-intercalated LDH material exhibits reversible optical responses (luminescent color, absorption band, and fluorescent lifetime) upon changing external pressure; molecular dynamics and periodic density functional theoretical studies demonstrate that the PCL performance originates from changes in the relative orientation and aggregation state of the interlayer BTZB. Such materials may serve as the fluorescent antiforgery devices.

2.2. Photoinduced-Responsive Materials. The photoinduced *cis-trans* isomerization of organic photofunctional materials (such as Schiff base and azobenzene derivative) has presented many interesting features, and their applications range from electronics to nonlinear devices [34–37]. In the solid state of these materials, the penetration between adjacent functional group and strong π-π stacking of chromophores may lead to a lack of sufficient free volume for the isomerization and lead to irreversibility or low efficiency of the process. This is one of the main bottlenecks in developing optical devices with superior optical properties based on the molecular isomerization. LDH nanosheets can provide the organic

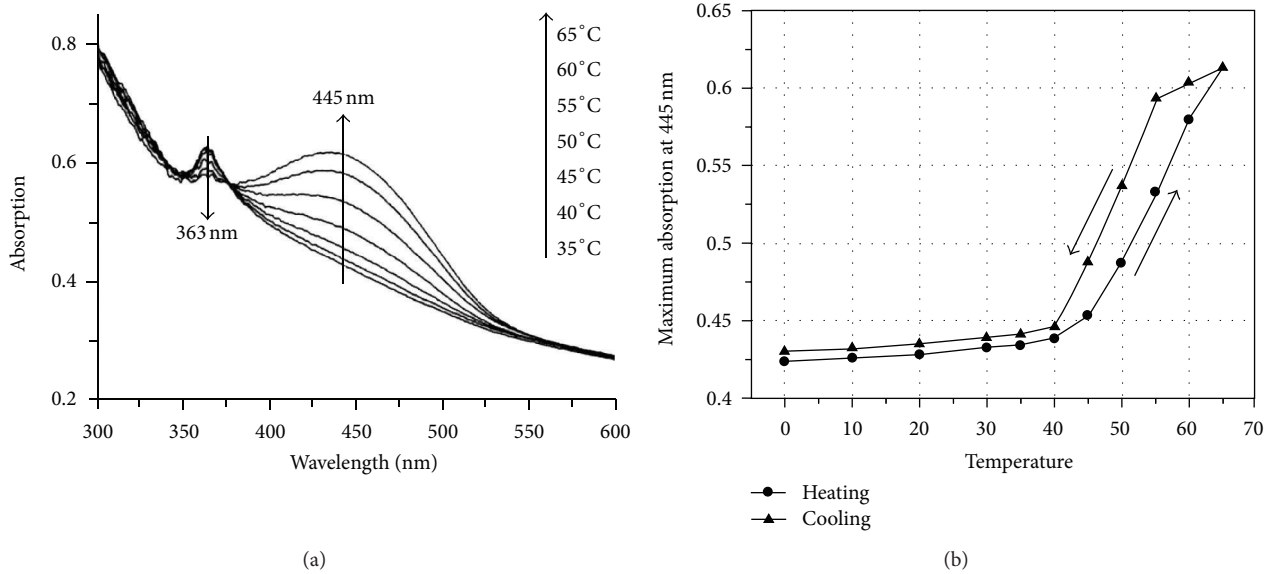


FIGURE 4: (a) *In-situ* absorption spectra of the 10% AO5-LDH film during heating in the temperature range 35–65°C. (b) The correlation between the absorbance of the band at 445 nm and temperature over a heating-cooling cycle [25].

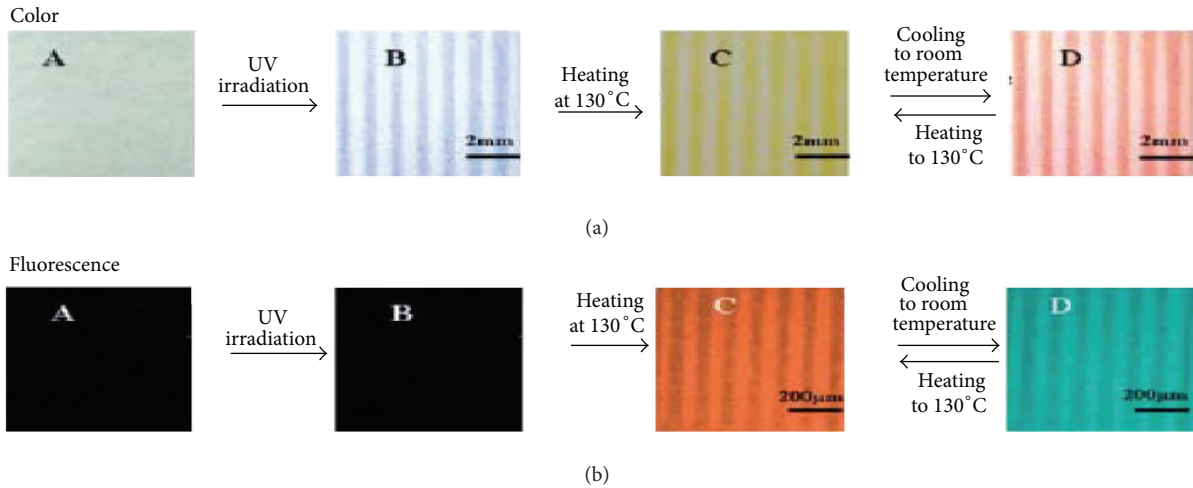


FIGURE 5: PDA-LDH film induced by UV irradiation and its thermochromic behavior (a) and fluorescent transition (b): (A) the DA-LDH film, (B) the PDA-LDH film obtained by UV irradiating (A), (C) the film by heating (B) at 130°C for 1 min, (D) the film by cooling (C) to room temperature [29].

chromophores with a rigid and ordered microenvironment, in which the severe interpenetration of the *cis-trans* groups may be restrained by the isolating effect of the 2D nanosheets. An ordered distribution and alignment of the *cis-trans* groups with sufficient available free space in the nanogallery between the LDH nanosheets can also facilitate their photoisomerization efficiency. In pioneering works, Tagaya et al. [38–40] have prepared sulfonated indolinespirobenzopyran (SP) intercalated into the Mg/Al and Zn/Al LDHs, which was premodified by toluene-*p*-sulfonic acid (PTS). The new intercalated nanocomposites exhibited reversible photoisomerization between SP and merocyanine (MC) as shown in the Figure 7. It was also noted that the presence of PTS play a key role in the reversible photoisomerization.

Han et al. [41] have reported the fabrication of hybrid ultrathin photoresponsive films based on LBL self-assembly of LDH nanosheets and the azobenzene-containing polymer (PAZO). By irradiating the sample with UV light, there is a progressive decrease in the maximum intensity of $\pi-\pi^*$ transition band, and the $\pi-\pi^*$ band nearly disappears after sufficient irradiation time, indicating an almost 100% *trans*-to-*cis* photoreaction. The $\pi-\pi^*$ absorption band increases again with irradiation by visible light ($\lambda > 450$ nm), indicative of the *cis-trans* back-isomerization of azobenzene. Furthermore, alternate irradiation with UV and visible light results in a reversible switching between the *trans*- and *cis*-state of the azobenzene group with significant changes in film color. The thin film of azobenzene derivative-intercalated LDH

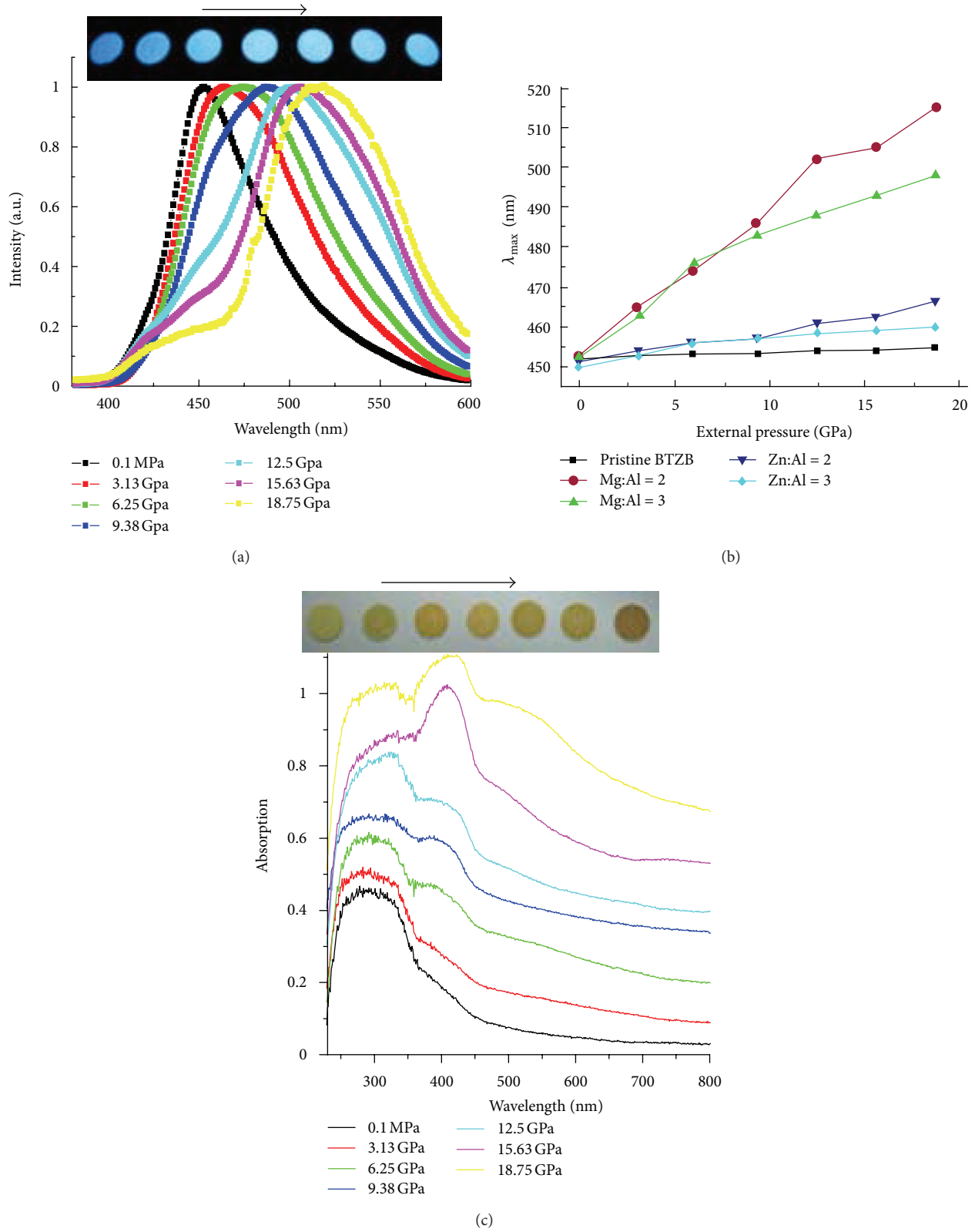


FIGURE 6: (a) Fluorescent spectra of the BTZB/Mg₂Al-LDH at different pressures (inset: fluorescent photographs under 365 nm UV light; the arrow shows the direction of the increasing pressure); (b) maximum emissive wavelength of BTZB/LDHs at different pressures; (c) UV-vis spectra of the BTZB/Mg₂Al-LDH at different pressures [33].

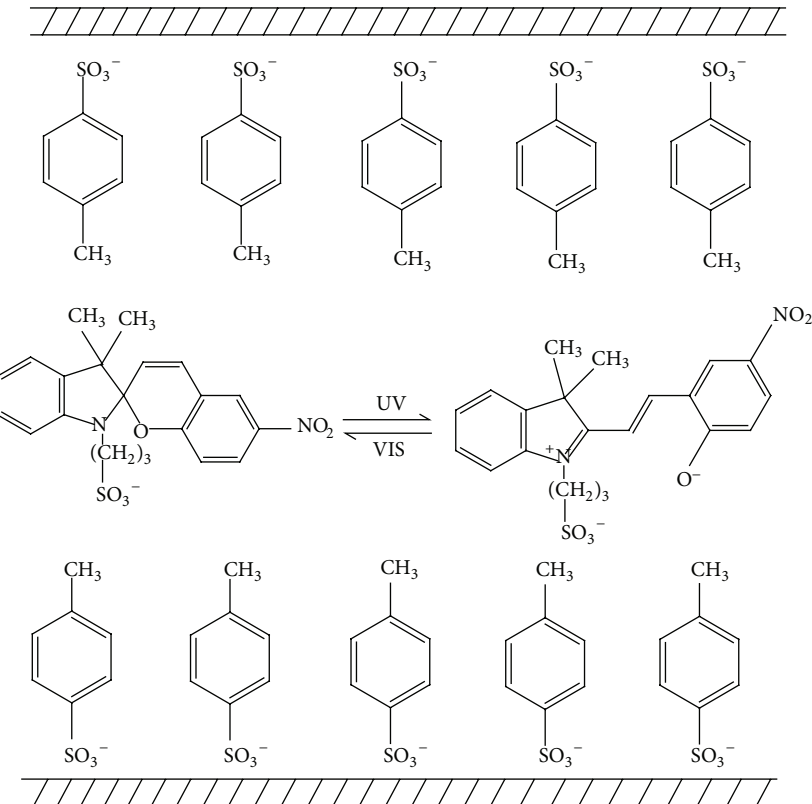


FIGURE 7: Possible mechanism for reversible photoisomerization of MC in LDH [40].

nanogallery can also influence the surface properties based on the photoisomerization. For example, Chen et al. [42] have fabricated a hybrid film with a fluorine-containing azobenzene within the LDH on a porous anodic alumina/aluminum substrate. Irradiation with UV light led to a switch in wettability of the film from superhydrophobic to hydrophilic as shown in Figure 8, and this process could be reversed by subsequent irradiation with visible light. Such behavior can be assigned to the difference between the dipole moments of *trans*- and *cis*-azobenzene isomers: the film containing the more polar *cis*-isomer will become more hydrophilic, while the *trans*-isomer makes the surface hydrophobic.

Wang et al. [43] have fabricated optically transparent thin films with photochromic properties by means of co-intercalation of azomethine-H anions (AMH) and 1-pentanesulfonate (PS) with different molar ratios into the nanogallery of a Zn-Al-LDH. XRD and SEM show that the film exhibits well-defined c-axis orientation. Fluorescence spectra demonstrate that the sample with 2% AMH molar percentage, with respect to the total organic material, exhibits the optimal luminescent intensity. It was observed that the fluorescence lifetime of *trans*-keto tautomer in the 2% AMH-LDH film is shorter than that of AMH solution, indicating the *trans*-keto tautomer of AMH is less stable in the 2D confined environment, and the ground state of the enol tautomer is well stabilized in the LDH nanogallery. The results demonstrate an effective method for the preparation of photochromic thin film materials by co-intercalation of chromophore and dispersant into an

inorganic 2D host matrix, which can be potentially applied in the field of photoelectronic devices.

2.3. Polarized and Electric-Induced Responsive Luminescence. The device with polarized emission can significantly enhance the quality of the back light of liquid-crystal displays [44, 45]. The LDH nanosheets with a 2D layered structure are intrinsically anisotropic; the luminescent guest with preferred orientation between LDH nanogallery can exhibit special anisotropic emission characteristics. Several examples have demonstrated that the ordered assembly of luminescent molecules into the LDH is undoubtedly favorable to produce a uniform orientation of transition dipole moment for polarized emission [12, 15, 46]. Based on the difference in the emissive colors of the chromophores at different polarization direction, it is possible to develop a new type of color-switching materials upon stimuli by polarized light. Recently, we have fabricated four types of heterogeneous multicolor luminescent UTF materials (blue/red, blue/yellow, blue/green, and red/green emission) by using different photofunctional anions [bis(*N*-methylacridinium)@polyvinylsulfonate ion pairs and anionic derivatives of poly(*p*-phenylene) (APP), poly(phenylenevinylene) (APPV), and poly(thiophene) (APT)] and LDH nanosheets as building blocks [47]. The strategy for fabricating multicolor luminescent UTFs involves the stepwise assembly of individual luminescent species and LDH nanosheets. Therefore,

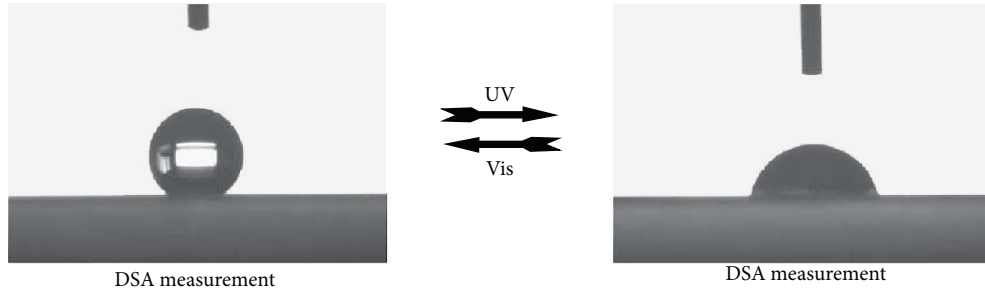


FIGURE 8: Shapes of a water droplet on the LDH hybrid film surface showing reversible superhydrophobicity and hydrophilicity induced by UV and visible irradiation [42].

the composition and loading of the luminescent species are finely controlled by adjusting the assembly sequence and cycle number, which is beneficial to the tunable multicolor emission. By changing the polarization direction of the two-color UTFs with a single excitation wavelength, it was observed that the intensity ratios for the two luminescence spectral regions were different, suggesting that the relative intensities of the two luminescence colors and the overall emission color are tuned by changing the polarization direction. For the $(\text{APPP/LDH})_{12}/(\text{APPV/LDH})_9$ UTF, the ratio of the intensities of luminescence at 410 and 550 nm (I_{410}/I_{550}) was 1.25 for the I_{VV} polarization, while it was only 0.71 for the I_{VH} polarization (Figure 9(a)). For the $(\text{APPP/LDH})_{12}/(\text{APT/LDH})_9$ UTF, the intensity ratio I_{410}/I_{575} had values of 1.65 (I_{VV} polarization mode) and 0.94 (I_{VH} polarization mode), respectively (Figure 9(b)). The variation in intensity ratio with polarization mode can be associated with the orientation and arrangement of the chromophores in the UTFs. We anticipate that these polarized-responsive luminescent UTFs can act as a possible color conversion layer in flat-panel displays for future lighting devices.

From a stimuli-responsive perspective, the electroluminescence (EL) can be regarded as an electric-induced responsive luminescence behavior of device. Quantum dots (QDs), with their tunable photoluminescence and band gap, are expected to play an important role in future displays [48, 49]. However, EL devices based on QDs have often suffered from relative low efficiency, short lifetimes, or the need of specialized deposition technique. Bendall et al. [50] have developed an all-inorganic EL device based on highly luminescent CdTe QD assembled LDH nanosheets by using a simple wet chemical process. The operating conditions were chosen to mimic the situation within an automotive environment, and the architecture of the device is shown in Figure 10. EL emission peak of the device is located at 637 nm. Compared with the photoluminescence (PL) emission peak of the bare QD, no shift in the peak position is detected for the EL peak, and no significant change in the peak width occurs. Such evidence demonstrates that the emission is solely due to the CdTe QD. The advantage of this device is that the operating temperatures can be over 80°C due to the all-inorganic materials. The authors believe the devices will have applications within harsh environments such as automobile

lighting and entertainment or outdoor signaling. The ease of fabrication will also provide simple and low cost light sources.

3. LDH-Based Chemical Stimuli-Responsive Properties

3.1. pH-Responsive Luminescent Materials. The pH fluorescence chemosensors play critical roles in studying physiological activities influenced by pH value, widely used in fields of analytical chemistry, bioanalytical chemistry, cytobiology, and medical science [53, 54]. The traditional solid host matrix (e.g., sol-gel polymer) has some inherent demerits, such as relatively poor thermal or optical stability as well as toxicity, which have limited the practical application in pH sensors to date. LDHs with a stable interlayer structure have highly enhanced the optical/thermal stability and environmental compatibility of the interlayer chromophore molecules and can be used as a new host matrix in more potential applications. Yan et al. [51] have fabricated a luminescent ordered UTF based on anionic polythiophene (APT) and Mg-Al-LDH nanosheets by the LBL assembly method. The dependence of the maximum emission wavelength (λ_{max}) on the pH value is divided into three main zones: the λ_{max} decreases sharply from 591 to 578 nm as the pH value is decreased from 14 to 12; it decreases very slightly from 578 to 574 nm when the pH value decreases from 12 to 8; finally, when the pH value is decreased from 8 to 4, the λ_{max} undergoes a decrease from 574 to 562 nm, which shows a nearly linear relationship with the pH. The sensitivity of the fluorescence performance of the APT/LDH UTFs to pH value can be attributed to the varying extent of protonation and deprotonation of APT between the LDH nanosheets. Typical photographs of the luminescence of the UTF under two pH conditions are shown in the inset of Figure 11, from which it can be observed that the UTF shows bright red luminescence and a relatively dark orange color at pH = 13 and pH = 4, respectively, under UV illumination. The APT/LDH UTF also exhibits reversible emissive response at different pH values, indicating its potential application as a pH-sensitive luminescence sensor.

Base on the example above, it can be known that the selection of a suitable fluorescent compound with high response to H⁺ in solution is of great importance for fabricating pH-sensitive optical materials. Shi et al. [55] have reported

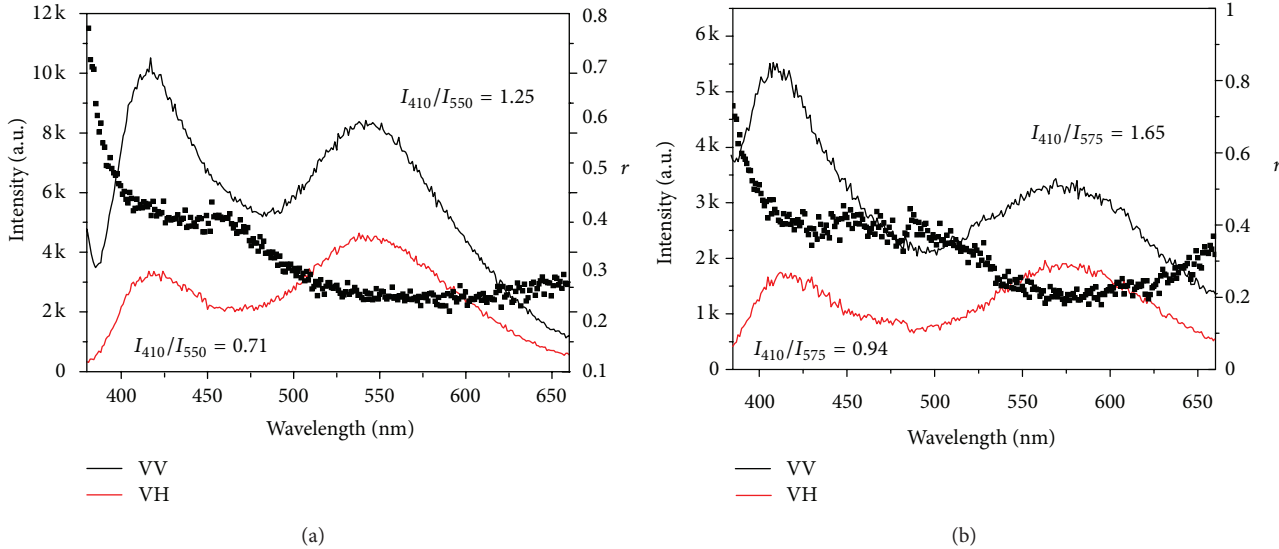


FIGURE 9: Polarized fluorescence profiles with glancing incidence geometry in the VV and VH modes and the anisotropy value (*r*) for two-color luminescent UTFs: (a) the (APPP/LDH)₁₂/(APPV/LDH)₉ UTF; (b) the (APPP/LDH)₁₂/(APT/LDH)₉ UTF [47].

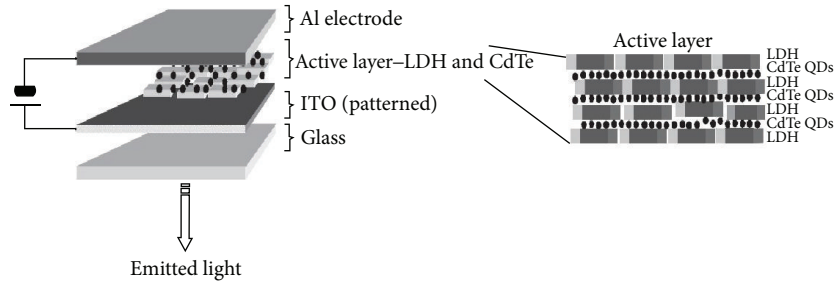


FIGURE 10: (a) Schematic of the architecture of the device, which is based on a ‘sandwich’ structure with alternating LDH nanosheets and CdTe QDs [50].

a highly oriented photoluminescent film with film thickness of 300 nm based on the fluorescein and 1-heptanesulfonic acid sodium co-intercalated into LDH matrix. The film exhibits a broad linear dynamic range for solution with pH value from 5.02 to 8.54. Good repeatability and reversibility have also been demonstrated: its relative standard deviation (RSD) is less than 1.5% in 20 consecutive cycles.

3.2. Metal Ion Responsive Luminescent Materials. The recognition of heavy metal ions (HMIs) is important in the fields of chemistry, biotechnology, medicine, and environmental science [56]. For instance, HMIs dispersed in an aqueous solution system (such as Hg²⁺ and Cd²⁺) can induce severe pollutions, which give rise to toxication and several diseases of organisms [57]. Thus, fast and effective detection of HMIs has drawn much attention from both scientific and engineering viewpoints during the last few years. The determination of HMIs has been generally carried out based on atomic absorption spectrometry [58] and inductively coupled plasma spectroscopy technique [59], which not only have good sensitivity and fast measurement capabilities, but

also require expensive instruments, well-controlled experimental conditions, and complicated procedures. Due to the high sensitivity, selectivity, fast response, low cost, and easy signal detection, the fluorescence-based chemical analysis should be a good method for determining and monitoring contaminants. In this sense, organic luminescent molecules have recently become good candidates to detect the metal ion, based on the selective quenching effects of the metal ions in the solution of the luminescent molecules [60]. For example, Tao et al. [61] have reported that the synthesized π -conjugated polymer exhibits a selective fluorescence quenching by Cu²⁺. Cao et al. [62] found that a metal-organic framework powder exhibited fluorescence quenching by the solutions of HMIs. To date, most of the reported organic luminescence systems used for detecting metal ions are in the form of solution or powder systems, whereas this is unfavorable for its facile manipulation and cycling utility. Moreover, most of the luminescent dye solutions can induce environmental pollution and even operational risk, which are detrimental to human health. Therefore, there continues to be a challenge to develop new types of solid luminescent film systems to meet

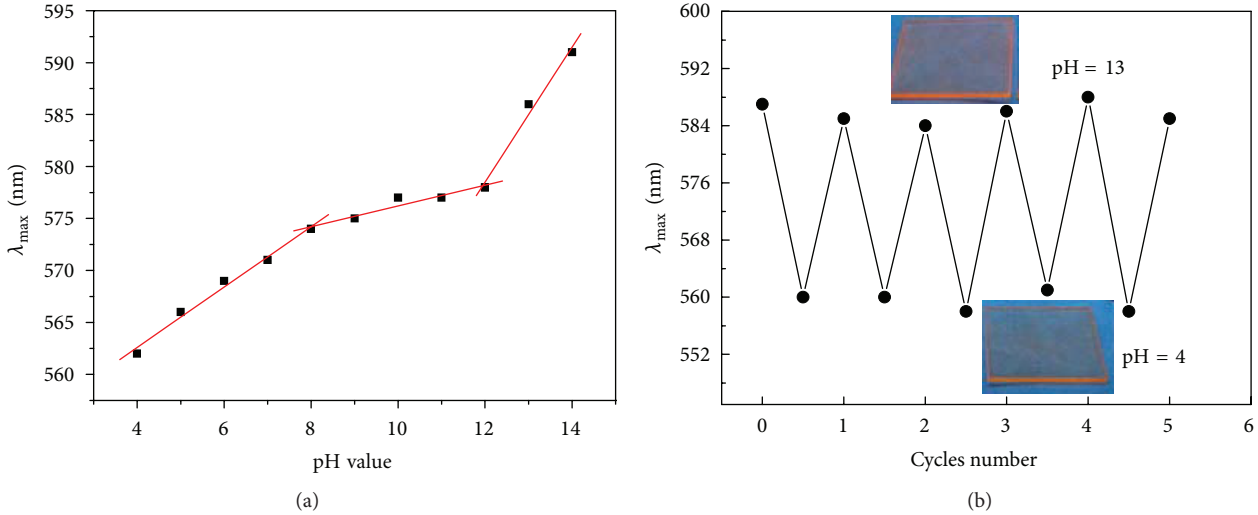


FIGURE 11: (a) Variation of the maximum photoemission wavelength of the APT/LDH film with different pH values; (b) the reversible photoemission response upon alternation between pH = 4 and pH = 13 (the inset show the luminescence photographs of the film at the two pH conditions) [51].

the need for the integration of high selectivity for the HMIs and efficient manipulation.

Mercury is considered one of the most toxic elements which are widely distributed in air, water, and soil [63, 64]. As a consequence of this pollution, mercury can accumulate in the human body, which causes a wide variety of diseases, even in a low concentration, such as digestive, kidney, and neurological disorders. Sun et al. [65] have reported that an optical thin film can serve as chemosensor based on 1-amino-8-naphthol-3,6-disulfonic acid sodium (H-acid) intercalated LDH. The H-acid/LDH film chemosensor was immersed into Hg^{2+} aqueous solutions with different concentrations at pH value 7.0 for 10 min then was washed thoroughly, and dried at 60°C for 20 min. It was found that the fluorescence intensity increases at first to a maximum and then decreases along with the increase of pH value. With the presence of other metal ions and common anions (Cr^{3+} , Mn^{2+} , Co^{2+} , Ni^{2+} , Cu^{2+} , Zn^{2+} , Ag^+ , Cd^{2+} , Mg^{2+} , Ca^{2+} , Li^+ , Na^+ , K^+ , Al^{3+} , Pb^{2+} , Cl^- , and NO_3^-), which are possible competitive ions in practical determination, the results show no significant effect on the results, demonstrating a strong resistance to interference. This film can be potentially used as a chemosensor for the detection of Hg^{2+} ion in the environmental and biological field. Yan et al. [66] have prepared the UTJs with blue luminescence based on a styrylbiphenyl derivative (BTBS) and Mg-Al-LDH nanosheets. The luminescence spectra of the (BTBS-LDH)₃₂ UTJ measured after immersing it in different metal cationic aqueous solutions (Hg^{2+} , Cu^{2+} , Pb^{2+} , Cd^{2+} , Cr^{3+} , Ca^{2+} , Mn^{2+} , Co^{2+} , Zn^{2+} , and Fe^{3+}) with varying concentrations (from 10^{-5} to 10^{-2} M) showed the fluorescence intensity of the UTJ decreases systematically upon increasing the ion concentration, and the Hg^{2+} has the most significant effect on the luminescence quenching of the UTJs with a detection limit of $2.3 \times 10^{-7} \text{ mol}\cdot\text{L}^{-1}$. After the UTJ was

treated with 0.01 M EDTA aqueous solution for 30 s, followed by thorough washing and drying, the fluorescence intensity can nearly recover to its initial state with 5 cycles at least.

Magnesium ion, being the most abundant intracellular divalent cation, plays a major role in many cellular processes including stabilization of DNA conformation, ion transport through the membrane, and signal transduction. Additionally, the activity of magnesium in blood and serum is an important clinical parameter that needs to be monitored in different situations. All these provide sufficient impetus to fabricate chemical sensors for the detection of magnesium [67, 68]. Jin et al. [69] have prepared a 8-aminonaphthalene-1,3,6-trisulfonate (ANTS)/LDH fluorescent film by an electrophoretic deposition (EPD) method. The ANTS/LDH film shows a good fluorescent response for Mg^{2+} ion. In addition, the linear correlation (R^2) between the fluorescence intensity of the ANTS/LDH and the concentration of Mg^{2+} is 0.996, with a detection limit of 2.37×10^{-7} M. The results exhibited that ANTS/LDH film has a considerable fluorescence selectivity for Mg^{2+} ions, with no significant response to other metal ions (Ca^{2+} , Na^+ , K^+ , Fe^{3+} , Co^{2+} , Ni^{2+} , or Cu^{2+}), which indicated a high fluorescence selectivity for Mg^{2+} ions.

Compared with intensity-based sensors, ratiometric fluorescence systems are preferred in bioimaging applications because such measurement involves the change of intensity ratio of emission at two wavelengths, which eliminates interferences from environment and increases the selectivity and sensitivity effectively. For example, Ji et al. [52] have built a fluorescence sensor for Be^{2+} with high selective response by alternate assembly of Beryllon II and Mg-Al-LDH nanosheets on quartz substrates using the LBL deposition technique. The Beryllon II/LDH UTJs displays ratiometric fluorescence response for Be^{2+} (Figure 12(a)) with a linear response range in 1.0×10^{-7} – 1.9×10^{-6} mol·L⁻¹ and a detection limit of

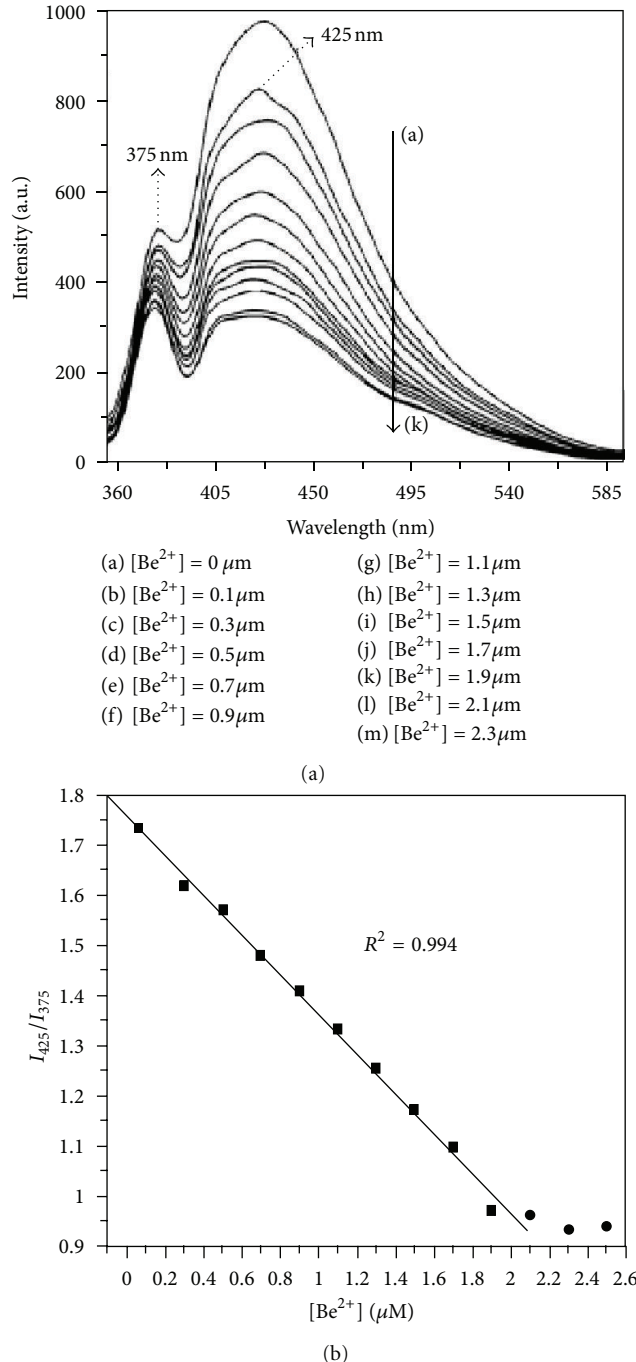


FIGURE 12: (a) Emission spectra of the (Beryllon II/LDH)₂₀ UTF upon increasing Be²⁺ concentration at pH = 11; (b) Be²⁺ titration curve of the chemosensor for emission ratio at 425–375 nm (I_{425}/I_{375}) [52].

$4.2 \times 10^{-9} \text{ mol}\cdot\text{L}^{-1}$ (Figure 12(b)). Evaluated with other competitive species (Zn^{2+} , Al^{3+} , Co^{2+} , Mg^{2+} , Cd^{2+} , Ca^{2+} , Hg^{2+} , Cu^{2+} , Pb^{2+} , Ni^{2+} , and Mn^{2+}), the Beryllon II/LDH UTF displays a good selectivity towards Be²⁺. A high thermodynamic affinity of Be²⁺ toward typical N and S-chelate ligands and fast metal-to-ligand binding kinetics lead to the complexation of Be²⁺ with Beryllon II in the UTF, which is the result of fluorescence quenching.

4. Conclusions and Outlook

The assembly of photoactive chromophore within the nanogallery of LDH can provide a facile way to develop new types of stimuli-responsive materials with host-guest structures, which also present enhanced properties (such as high photo-/optical stability and good operability). By designing and choosing the suitable photoactive chromophores and LDH layers as basic building blocks, these organic-inorganic

hybrid nanomaterials (ultrathin films and nanocomposites) have presented promising applications in the field of switches of piezochromic, photochromic, thermochromic, and polarized luminescence as well as pH/metal sensors. To meet the need of practical application, further studies should be put in how to finely regular and control the arrangement and orientation of the guest chromophore and how to maintain the uniform and ordered thin film system. In addition, challenges for stimuli-responsive host-guest materials include how to further enhance the photo-/thermosomerization efficiency and repeatability. Moreover, despite several researches on single-stimulus-responsive property of such materials, development on multistimuli-responsive smart materials still remains in its fancy and has been very seldom studied. This can be an important strategy and direction to develop multifunctional materials. Last but not least, the response time and on/off ratio of these switches and sensors for real-time applications should also be taken in account in next step researches.

Acknowledgments

This work was supported by the National Natural Science Foundation of China, the 973 Program (Grant no. 2011CBA00504), 111 Project (Grant no. B07004), and Program for Changjiang Scholars and Innovative Research Team in University (PCSIRT: IRT1205).

References

- [1] M. Irie, T. Fukaminato, T. Sasaki, N. Tamai, and T. Kawai, "A digital fluorescent molecular photoswitch," *Nature*, vol. 420, no. 6917, pp. 759–760, 2002.
- [2] C. Löwe and C. Weder, "Oligo(p-phenylene vinylene) excimers as molecular probes: deformation-induced color changes in photoluminescent polymer blends," *Advanced Materials*, vol. 14, no. 22, pp. 1625–1629, 2002.
- [3] T. Mutai, H. Tomoda, T. Ohkawa, Y. Yabe, and K. Araki, "Switching of polymorph-dependent ESIPT luminescence of an imidazo[1,2-a]pyridine derivative," *Angewandte Chemie—International Edition*, vol. 120, no. 49, pp. 9664–9666, 2008.
- [4] J. Kunzelman, M. Kinami, B. R. Crenshaw, J. D. Protasiewicz, and C. Weder, "Oligo(p-phenylene vinylene)s as a "new" class of piezochromic fluorophores," *Advanced Materials*, vol. 20, no. 1, pp. 119–122, 2008.
- [5] T. Fukaminato and M. Irie, "Reversible fluorescence wavelength shift based on photoinduced aggregate formation," *Advanced Materials*, vol. 18, no. 24, pp. 3225–3228, 2006.
- [6] N. Chandrasekharan and L. A. Kelly, "A dual fluorescence temperature sensor based on perylene/exciplex interconversion," *Journal of the American Chemical Society*, vol. 123, no. 40, pp. 9898–9899, 2001.
- [7] J. Kunzelman, B. R. Crenshaw, and C. Weder, "Self-assembly of chromogenic dyes—a new mechanism for humidity sensors," *Journal of Materials Chemistry*, vol. 17, no. 29, pp. 2989–2991, 2007.
- [8] C. Xia and R. C. Advincula, "Decreased aggregation phenomena in polyfluorenes by introducing carbazole copolymer units," *Macromolecules*, vol. 34, no. 17, pp. 5854–5859, 2001.
- [9] V. Rives, *Layered Double Hydroxides: Present and Future*, Nova Science, New York, NY, USA, 2001.
- [10] F. Li and X. Duan, "Applications of layered double hydroxide," *Structure and Bonding*, vol. 119, pp. 193–223, 2006.
- [11] S. P. Newman and W. Jones, "Synthesis, characterization and applications of layered double hydroxides containing organic guests," *New Journal of Chemistry*, vol. 22, no. 2, pp. 105–115, 1998.
- [12] D. P. Yan, J. Lu, M. Wei, D. G. Evans, and X. Duan, "Sulforhodamine B intercalated layered double hydroxide thin film with polarized photoluminescence," *Journal of Physical Chemistry B*, vol. 113, no. 5, pp. 1381–1388, 2009.
- [13] D. P. Yan, J. Lu, J. Ma, M. Wei, D. G. Evans, and X. Duan, "Benzocarbazole anions intercalated layered double hydroxide and its tunable fluorescence," *Physical Chemistry Chemical Physics*, vol. 12, no. 45, pp. 15085–15092, 2010.
- [14] W. Shi, M. Wei, J. Lu et al., "Molecular orientation and fluorescence studies on naphthalene acetate intercalated Zn₂Al layered double hydroxide," *Journal of Physical Chemistry C*, vol. 112, no. 50, pp. 19886–19895, 2008.
- [15] D. P. Yan, J. Lu, M. Wei et al., "Poly(p-phenylene) anionic derivative/layered double hydroxides ordered ultra thin films with blue luminescence by layer-by-layer assembly," *Angewandte Chemie—International Edition*, vol. 48, no. 17, pp. 3073–3076, 2009.
- [16] D. P. Yan, J. Lu, J. Ma et al., "Anionic poly(p-phenylenevinylene)/layered double hydroxide ordered ultrathin films with multiple quantum well structure: a combined experimental and theoretical study," *Langmuir*, vol. 26, no. 10, pp. 7007–7014, 2010.
- [17] S. Li, J. Lu, M. Wei, D. G. Evans, and X. Duan, "Tris(8-hydroxyquinoline-5-sulfonate)aluminum intercalated Mg-Al layered double hydroxide with blue luminescence by hydrothermal synthesis," *Advanced Functional Materials*, vol. 20, no. 17, pp. 2848–2856, 2010.
- [18] D. P. Yan, J. Lu, M. Wei, J. Ma, D. G. Evans, and X. Duan, "A combined study based on experiment and molecular dynamics: perylene tetracarboxylate intercalated in a layered double hydroxide matrix," *Physical Chemistry Chemical Physics*, vol. 11, no. 40, pp. 9200–9209, 2009.
- [19] D. P. Yan, J. Lu, M. Wei, D. G. Evans, and X. Duan, "Recent advances in photofunctional guest/layered double hydroxide host composite systems and their applications: experimental and theoretical perspectives," *Journal of Materials Chemistry*, vol. 21, pp. 13128–13139, 2011.
- [20] I. McCulloch, M. Heeney, C. Bailey et al., "Liquid-crystalline semiconducting polymers with high charge-carrier mobility," *Nature Materials*, vol. 5, no. 4, pp. 328–333, 2006.
- [21] M. A. Thyveetil, P. V. Coveney, H. C. Greenwell, and J. L. Suter, "Role of host layer flexibility in DNA guest intercalation revealed by computer simulation of layered nanomaterials," *Journal of the American Chemical Society*, vol. 130, no. 37, pp. 12485–12495, 2008.
- [22] L. Tian, F. He, H. Zhang et al., "Thermal cycloaddition facilitated by orthogonal π-π organization through conformational transfer in a swivel-cruciform oligo (phenylenevinylene)," *Angewandte Chemie—International Edition*, vol. 46, no. 18, pp. 3245–3248, 2007.
- [23] H. Meier, "Conjugated oligomers with terminal donor-acceptor substitution," *Angewandte Chemie—International Edition*, vol. 44, no. 17, pp. 2482–2506, 2005.
- [24] D. P. Yan, J. Lu, M. Wei, J. Ma, D. G. Evans, and X. Duan, "Reversibly thermochromic, fluorescent ultrathin films

- with a supramolecular architecture," *Angewandte Chemie—International Edition*, vol. 50, no. 3, pp. 720–723, 2011.
- [25] X. Wang, J. Lu, W. Shi et al., "A thermochromic thin film based on host-guest interactions in a layered double hydroxide," *Langmuir*, vol. 26, no. 2, pp. 1247–1253, 2010.
- [26] M. Inouye, K. Tsuchiya, and T. Kitao, "New thermo-response dyes: coloration by the claisen rearrangement and intramolecular acid-base reaction," *Angewandte Chemie—International Edition*, vol. 31, no. 2, pp. 204–205, 1992.
- [27] A. Sarkar, S. Okada, H. Matsuzawa, H. Matsuda, and H. Nakanishi, "Novel polydiacetylenes for optical materials: beyond the conventional polydiacetylenes," *Journal of Materials Chemistry*, vol. 10, no. 4, pp. 819–828, 2000.
- [28] H. J. Cho, K. Seo, C. J. Lee, H. Yun, and J. Y. Chang, "Rodlike mesogenic molecules consisting of two diacetylenic groups: mesomorphic behavior and photoimaging," *Journal of Materials Chemistry*, vol. 13, no. 5, pp. 986–990, 2003.
- [29] W. Y. Shi, Y. J. Lin, S. He et al., "Patterned fluorescence films with reversible thermal response based on the host-guest superarchitecture," *Journal of Materials Chemistry*, vol. 21, pp. 11116–11122, 2011.
- [30] Z. G. Chi and J. R. Xu, "New thermally stable piezofluorochromic aggregation-induced emission compounds," *Organic Letters*, vol. 13, no. 4, pp. 556–559, 2011.
- [31] X. Zhang, Z. Chi, H. Li et al., "Piezofluorochromism of an aggregation-induced emission compound derived from tetraphenylethylene," *Chemistry*, vol. 6, no. 3, pp. 808–811, 2011.
- [32] Z. Chi, X. Zhang, B. Xu et al., "Recent advances in organic mechanofluorochromic materials," *Chemical Society Reviews*, vol. 41, no. 10, pp. 3878–3896, 2012.
- [33] D. P. Yan, J. Lu, J. Ma et al., "Layered host-guest materials with reversible piezochromic luminescence," *Angewandte Chemie—International Edition*, vol. 50, no. 31, pp. 7037–7040, 2011.
- [34] J. Zhang, Q. Zou, and H. Tian, "Photochromic materials: more than meets the eye," *Advanced Materials*, vol. 25, no. 3, pp. 378–399, 2012.
- [35] T. F. Tan, P. L. Chen, H. M. Huang, and J. B. Meng, "Synthesis, characterization and photochromic studies in film of heterocycle-containing spirooxazines," *Tetrahedron*, vol. 61, no. 34, pp. 8192–8198, 2005.
- [36] H. Durr, "Perspective in photochromism-based on the 1-5-electrocyclization of heteroanalogous pentadienyl anions," *Angewandte Chemie—International Edition*, vol. 28, pp. 413–431, 1989.
- [37] E. H. Kang, T. Bu, P. Jin, J. Sun, Y. Yang, and J. Shen, "Layer-by-layer deposited organic/inorganic hybrid multilayer films containing noncentrosymmetrically orientated azobenzene chromophores," *Langmuir*, vol. 23, no. 14, pp. 7594–7601, 2007.
- [38] H. Tagaya, T. Kuwahara, S. Sato, J. I. Kadokawa, M. Karasu, and K. Chiba, "Photoisomerization of indolinespirobenzopyran in layered double hydroxides," *Journal of Materials Chemistry*, vol. 3, no. 3, pp. 317–318, 1993.
- [39] T. Kuwahara, H. Tagaya, and K. Chiba, "Photochromism of spirobypyan dye in Li-Al layered double hydroxide," *Microporous Materials*, vol. 4, no. 2-3, pp. 247–250, 1995.
- [40] H. Tagaya, S. Sato, T. Kuwahara, J. I. Kadokawa, K. Masa, and K. Chiba, "Photoisomerization of indolinespirobenzopyran in anionic clay matrices of layered double hydroxides," *Journal of Materials Chemistry*, vol. 4, no. 12, pp. 1907–1912, 1994.
- [41] J. B. Han, D. P. Yan, W. Y. Shi et al., "Layer-by-layer ultrathin films of azobenzene-containing polymer/layered double hydroxides with reversible photoresponsive behavior," *Journal of Physical Chemistry B*, vol. 114, no. 17, pp. 5678–5685, 2010.
- [42] T. Chen, S. Xu, F. Zhang, D. G. Evans, and X. Duan, "Formation of photo- and thermo-stable layered double hydroxide films with photo-responsive wettability by intercalation of functionalized azobenzenes," *Chemical Engineering Science*, vol. 64, no. 21, pp. 4350–4357, 2009.
- [43] X. R. Wang, J. Lu, D. P. Yan, M. Wei, D. G. Evans, and X. Duan, "A photochromic thin film based on salicylideneaniline derivatives intercalated layered double hydroxide," *Chemical Physics Letters*, vol. 493, no. 4-6, pp. 333–339, 2010.
- [44] C. Weder, C. Sarwa, A. Montali, C. Bastiaansen, and P. Smith, "Incorporation of photoluminescent polarizers into liquid crystal displays," *Science*, vol. 279, no. 5352, pp. 835–837, 1998.
- [45] B. Zhou, Y. Lin, L. Monica Veca, K. A. Shiral Fernando, B. A. Harruff, and Y. P. Sun, "Luminescence polarization spectroscopy study of functionalized carbon nanotubes in a polymeric matrix," *Journal of Physical Chemistry B*, vol. 110, no. 7, pp. 3001–3006, 2006.
- [46] D. P. Yan, S. Qin, L. Chen et al., "Thin film of sulfonated zinc phthalocyanine/layered double hydroxide for achieving multiple quantum well structure and polarized luminescence," *Chemical Communications*, vol. 46, no. 45, pp. 8654–8656, 2010.
- [47] D. P. Yan, J. Lu, M. Wei et al., "Heterogeneous transparent ultrathin films with tunable-color luminescence based on the assembly of photoactive organic molecules and layered double hydroxides," *Advanced Functional Materials*, vol. 21, no. 13, pp. 2497–2505, 2011.
- [48] G. Mingyuan, C. Lesser, S. Kirstein, E. Möhwald, A. L. Rogach, and H. Weller, "Electroluminescence of different colors from polycation/CdTe nanocrystal self-assembled films," *Journal of Applied Physics*, vol. 87, no. 5, pp. 2297–2302, 2000.
- [49] W. Chung, K. Park, H. J. Yu, J. Kim, B. H. Chun, and S. H. Kim, "White emission using mixtures of CdSe quantum dots and PMMA as a phosphor," *Optical Materials*, vol. 32, no. 4, pp. 515–521, 2010.
- [50] J. S. Bendall, M. Paderi, F. Ghigliotti et al., "Layer-by-layer all-inorganic quantum-dot-based LEDs: a simple procedure with robust performance," *Advanced Functional Materials*, vol. 20, no. 19, pp. 3298–3302, 2010.
- [51] D. P. Yan, J. Lu, J. Ma, M. Wei, D. G. Evans, and X. Duan, "Fabrication of an anionic polythiophene/layered double hydroxide ultrathin film showing red luminescence and reversible pH photoresponse," *AIChE Journal*, vol. 57, no. 7, pp. 1926–1935, 2011.
- [52] X. L. Ji, W. Y. Shi, S. T. Zhang, M. Wei, D. G. Evans, and X. Duan, "A ratiometric fluorescence sensor for Be²⁺ based on Beryllon II/layered double hydroxide ultrathin films," *Analytica Chimica Acta*, vol. 728, pp. 77–85, 2012.
- [53] I. Roy and M. N. Gupta, "Smart polymeric materials: emerging biochemical applications," *Chemistry & Biology*, vol. 10, no. 12, pp. 1161–1171, 2003.
- [54] E. S. Gil and S. M. Hudson, "Stimuli-responsive polymers and their bio-conjugates," *Progress in Polymer Science*, vol. 29, no. 12, pp. 1173–1222, 2004.
- [55] W. Y. Shi, S. He, M. Wei, D. G. Evans, and X. Duan, "Optical pH sensor with rapid response based on a fluorescein-intercalated layered double hydroxide," *Advanced Functional Materials*, vol. 20, no. 22, pp. 3856–3863, 2010.

- [56] H. N. Kim, Z. Guo, W. Zhu, J. Yoon, and H. Tian, "Recent progress on polymer-based fluorescent and colorimetric chemosensors," *Chemical Society Reviews*, vol. 40, no. 1, pp. 79–93, 2011.
- [57] S. Yoon, E. W. Miller, Q. He, P. H. Do, and C. J. Chang, "A bright and specific fluorescent sensor for mercury in water, cells, and tissue," *Angewandte Chemie—International Edition*, vol. 46, no. 35, pp. 6658–6661, 2007.
- [58] J. V. Cizdziel and S. Gerstenberger, "Determination of total mercury in human hair and animal fur by combustion atomic absorption spectrometry," *Talanta*, vol. 64, no. 4, pp. 918–921, 2004.
- [59] S. C. Hight and J. Cheng, "Determination of methylmercury and estimation of total mercury in seafood using high performance liquid chromatography (HPLC) and inductively coupled plasma-mass spectrometry (ICP-MS): method development and validation," *Analytica Chimica Acta*, vol. 567, no. 2, pp. 160–172, 2006.
- [60] M. Wang, G. Zhang, D. Zhang, D. Zhu, and B. Z. Tang, "Fluorescent bio/chemosensors based on silole and tetraphenylethene luminogens with aggregation-induced emission feature," *Journal of Materials Chemistry*, vol. 20, no. 10, pp. 1858–1867, 2010.
- [61] X. Tao, Y. Liu, and K. S. Schanze, "A conjugated polyelectrolyte-based fluorescence sensor for pyrophosphate," *Chemical Communications*, no. 28, pp. 2914–2916, 2007.
- [62] Y. Cao, Y. Cui, Q. Zheng, S. Xiang, G. Qian, and B. Chen, "A microporous luminescent metal-organic framework for highly selective and sensitive sensing of Cu²⁺ in aqueous solution," *Chemical Communications*, vol. 46, no. 30, pp. 5503–5505, 2010.
- [63] I. Onyido, A. R. Norris, and E. Buncel, "Biomolecule-mercury interactions: modalities of DNA base-mercury binding mechanisms. Remediation strategies," *Chemical Reviews*, vol. 104, no. 12, pp. 5911–5929, 2004.
- [64] N. S. Bloom, A. K. Grout, and E. M. Prestbo, "Development and complete validation of a method for the determination of dimethyl mercury in air and other media," *Analytica Chimica Acta*, vol. 546, no. 1, pp. 92–101, 2005.
- [65] Z. Y. Sun, L. Jin, S. T. Zhang et al., "An optical sensor based on H-acid/layered double hydroxide composite film for the selective detection of mercury ion," *Analytica Chimica Acta*, vol. 702, no. 1, pp. 95–101, 2011.
- [66] D. P. Yan, J. Lu, M. Wei, D. G. Evans, and X. Duan, "Luminescent ultrathin film of the anionic styrylbiphenyl derivatives/layered double hydroxide and its reversible sensing for heavy metal ions," *Physical Chemistry Chemical Physics*, vol. 14, no. 24, pp. 8591–8598, 2012.
- [67] M. Ishida, Y. Naruta, and F. Tani, "A Porphyrin-related macrocycle with an embedded 1,10-phenanthroline moiety: fluorescent magnesium(II) ion sensor," *Angewandte Chemie—International Edition*, vol. 49, no. 1, pp. 91–94, 2010.
- [68] J. L. Lopez, A. Tárraga, A. Espinosa et al., "A new multifunctional ferrocenyl-substituted ferrocenophane derivative: optical and electronic properties and selective recognition of Mg²⁺ ions," *Chemistry*, vol. 10, no. 7, pp. 1815–1826, 2004.
- [69] L. Jin, Z. J. Guo, Z. Y. Sun, A. Li, Q. Jin, and M. Wei, "Assembly of 8-aminonaphthalene-1,3,6-trisulfonate intercalated layered double hydroxide film for the selective detection of Mg²⁺," *Sensors and Actuators B*, vol. 161, pp. 714–720, 2012.

Research Article

Influence of Different Carboxylic Acid Ligands on Luminescent Properties of Eu(Lc)₃phen (Lc = MAA, AA, BA, SA) Complexes

Jing Zhang, Le Zhang, Yan Chen, Xiaogu Huang, Lixi Wang, and Qitu Zhang

College of Materials Science and Engineering, Nanjing University of Technology, Nanjing, Jiangsu 210009, China

Correspondence should be addressed to Qitu Zhang; njzqt@126.com

Received 27 September 2012; Accepted 28 December 2012

Academic Editor: Su Chen

Copyright © 2013 Jing Zhang et al. This is an open access article distributed under the Creative Commons Attribution License, which permits unrestricted use, distribution, and reproduction in any medium, provided the original work is properly cited.

A series of rare earth europium complexes with different carboxylic acid ligands Eu(Lc)₃phen (Lc = MAA, AA, BA, SA) were synthesized. The complexes were characterized by FTIR, TG-DSC, XRD, UV absorption spectra, and photoluminescence spectra (PL) to study the structure, thermal stability, the energy absorption, and luminescent properties of the complexes. The results showed that the series complexes are all with good crystallization and relatively high thermal stability. The differences of the luminescent properties of complexes are caused by the different ligand structures. The absorption intensity of the carboxylic acid ligands, BA, was the strongest, followed by the MAA and AA and SA was the weakest. Therefore, the fluorescence intensity of the Eu(BA)₃phen was the strongest, followed by the Eu(MAA)₃phen and Eu(AA)₃phen and the Eu₂(SA)₃phen₂ was the weakest. All complexes showed good luminescence properties.

1. Introduction

Rare earth organic complexes have become a family of luminescent materials. They are widely applied in laser, electroluminescent, photoluminescence, and so forth, especially as the emission layer for organic light emitting diode (OLED) [1–3]. As early as 1942, Weissman [4] reported that europium β -diketone complexes exhibited luminescence when the rare earth organic complex was irradiated by ultraviolet light. After that, the rare earth complexes containing β -diketonates have been deeply studied about applications for luminescence. Recently, there has been a great interest in the study of rare earth and carboxylic acid complexes due to their low cost, good thermal stability, long luminescence time, color purity, and intense luminescence [5–9]. Moreover, it was found that luminescent properties could be improved by changing the molecular structure and the electrically neutral ligand [10–14]. This is because the electrically neutral ligand can substitute H₂O to enhance the luminescence intensity [15, 16]. From the previous experimental results, it can be concluded that 1,10-Phenanthroline monohydrate is better than 2,2'-dipyridyl as the electrically neutral ligand [17].

From the coordination chemistry point of view, the complexes contained europium ions tend to multiple coordination structure. The organic anions as the carboxylic acid ligands (first ligands) to satisfy charge balance. Electrically neutral ligands (second ligands) meet Ln ion coordination number. Liu et al. [18] described that the luminescence intensity of Eu(TTA)₃phen and Eu(TTA)₃Dipy is stronger than that of Eu(DMB)₃phen and Eu(DMB)₃Dipy. Yan et al. [11] studied the luminescent properties of the rare earth organic complexes containing terbium ions with different carboxylic acid ligands. The results show that different carboxylic acid ligands have a certain influence on the fluorescence intensity. Therefore, the efficiency of luminescence of organic rare earth complexes can be improved by adjusting the carboxylic acid ligands.

This paper focuses on the influence of different carboxylic acid ligands on luminescent properties of series rare earth organic complexes. In order to compare the luminescent properties with different complexes, some carboxylic acids containing specific radical group were selected. Methacrylic acid (MAA) contains methyl, and benzoic acid (BA) contains benzene ring. In addition, succinate was selected as

TABLE 1: The europium content in the Eu(Lc)₃phen complexes.

	Eu(MAA) ₃ phen	Eu(AA) ₃ phen	Eu(BA) ₃ phen	Eu ₂ (SA) ₃ phen ₂
Theoretical value	25.09%	26.83%	21.21%	28.82%
Experimental value	24.65%	26.69%	21.20%	28.10%

the carboxylic acid ligand. We compared the monocarboxylic acid and dicarboxylic acid as the carboxylic acid ligands on the luminescence properties. In this paper, four rare earth europium binary complexes Eu(MAA)₃phen, Eu(AA)₃phen, Eu(BA)₃phen, and Eu₂(SA)₃phen₂ were synthesized to study the influence of carboxylic acid ligand on the luminescent properties of binary complexes.

2. Experimental

2.1. Reagent and Synthesis of Binary Europium Complexes. Solution of rare earth chloride (0.25 mol/L) was prepared from high purity Eu₂O₃ (>99.99%, the others are analytical grade) by dissolving in concentrated hydrochloric acid (6 mol/L). MAA (methacrylic acid, 1.5 mol/L), AA (acrylic acid, 1.5 mol/L), BA (benzoic acid, 0.5 mol/L), and SA (succinic acid, 0.375 mol/L) were added in anhydrous ethanol and the pH adjusted to 7.0 with ammonium hydroxide.

All samples were synthesized by the coprecipitation method. With the synthesis method of Eu(MAA)₃phen, for example. MAA in anhydrous ethanol (15 mL) was dropwise added into the stirred solution of europium chloride in anhydrous ethanol (30 mL), and then the pH value of the mixture was adjusted to 6-7 using ammonium hydroxide. The mixture was stirred for 30 minutes, and then the solution of 1,10-Phenanthroline monohydrate (phen) in anhydrous ethanol (0.1 mol/L, 15 mL) was added dropwise. The resulting solution was stirred at room temperature for 3 hours and standing overnight. The precipitate was filtered and washed with anhydrous ethanol by 3 times, and finally dried at 80°C, to obtain Eu(MAA)₃phen. The preparation method of different carboxylic acid ligand complexes is basically same.

2.2. Measurement. The FT-IR spectra were recorded in the 4000–400 cm⁻¹ region by the NICOLET 5700 with KBr plates. The thermal gravimetric analyses (TG) and differential scanning calorimetry (DSC) of the complexes measured by the STA449C Thermo Gravimetric Analyzer (Netzsch, Germany) were made in N₂ with a heating rate 10°C/min in the range of 50 ~ 800°C. X-ray diffraction analysis of the samples was carried out using an X-ray diffractometer (model D/MAX2500, Rigak, Japan) with Cu K α radiation ($\lambda = 1.5406 \text{ \AA}$) in the range of 5° ~ 80° with a step size of 0.02°. The absorption spectra were recorded using UV-Vis spectrophotometer (Shimadzu UV-3101). They were measured in 1 × 10⁻⁵ mol/L DMSO solution at room temperature. The photoluminescence spectra of the rare earth organic complexes were measured using a Horiba Jobin Yvon fluorescence spectrophotometer (FL3-221, France) at room temperature.

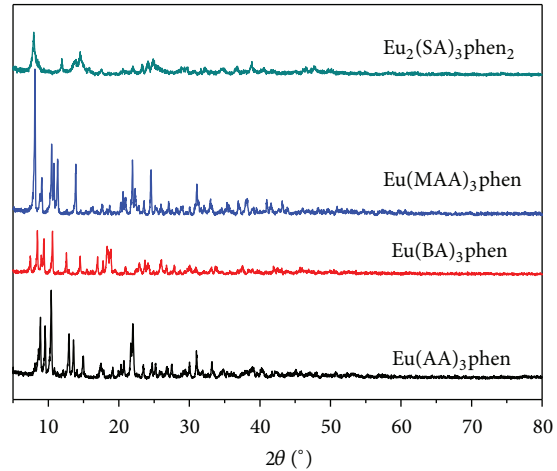


FIGURE 1: X-ray diffraction diagrams of complexes.

3. Results and Discussion

3.1. Structure of Eu(Lc)₃phen Powders. The europium content was determined by the EDTA titration, and the results were shown in Table 1. We have synthesized Eu(Lc)₃phen (Lc = MAA, AA, BA, SA) complexes successfully, as the theoretical values and experimental values are similar.

Figure 1 reports the XRD patterns of four complexes: (1) Eu₂(SA)₃phen₂, (2) Eu(MAA)₃phen, (3) Eu(BA)₃phen, and (4) Eu(AA)₃phen. The main peaks of the complexes appear from 5° to 25° (2θ). Several intense diffraction peaks can be seen from the X-ray diffraction diagrams of the four complexes, indicating that the complexes are crystal.

Moreover, all diffraction peaks of the four complexes appear before 45°, the higher *d*-values were determined by large values of the interplanar spacing. Therefore, it has decrease effect between the europium ions itself.

Figure 2 reports the FT-IR spectra of the ligands and the four complexes. FTIR spectra of Eu(MAA)₃phen, Eu(AA)₃phen, Eu(BA)₃phen, and Eu₂(SA)₃phen₂ complexes have been recorded in the 400–4000 cm⁻¹ region. The IR spectra data is shown in Table 2.

It can be found that the characteristic peaks of $\nu_{\text{C=O}}$ in the MAA, AA, BA, and SA disappeared at about 1737 cm⁻¹, 1724 cm⁻¹, 1687 cm⁻¹, and 1694 cm⁻¹, respectively. The presence of carboxylate groups in the series complexes was definitely confirmed by both the symmetric stretching bands (ν_{sCOO^-}) at about 1427 cm⁻¹ and the asymmetric stretching bands (ν_{asCOO^-}) at about 1562 cm⁻¹. These results showed that the carbonyl groups were coordinated with the europium ions [19]. In addition, the stretching vibration peak ($\nu_{\text{C=N}}$) at about 1643 cm⁻¹ in phen shifted from 1643

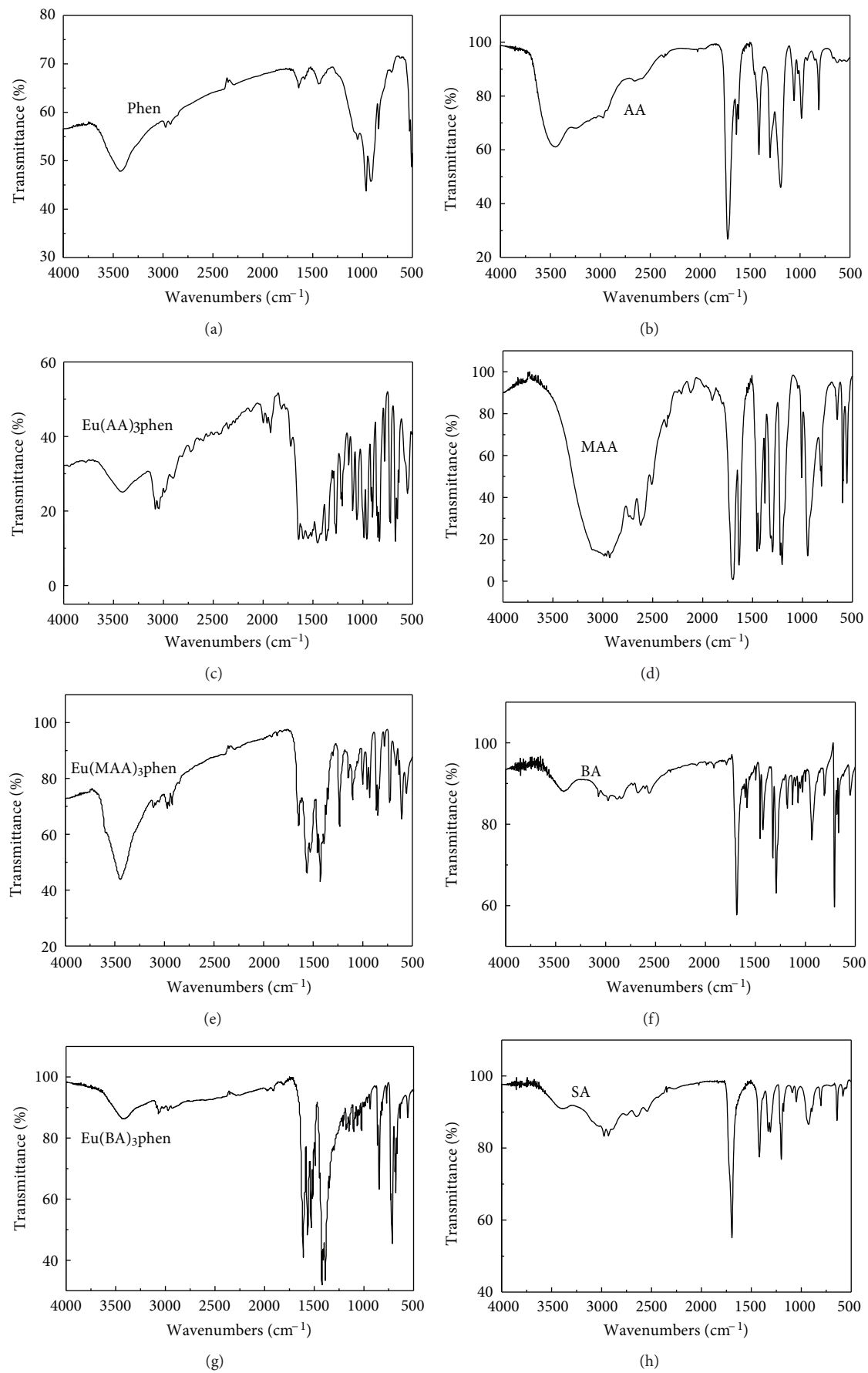
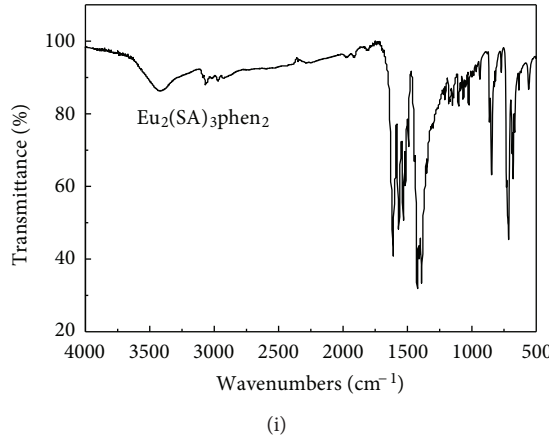


FIGURE 2: Continued.

FIGURE 2: FT-IR spectra of ligands and Eu(Lc)₃phen complexes.TABLE 2: Character FT-IR bands (cm^{-1}) of the ligands and their complexes.

Ligands and complexes	$\nu_{\text{O-H}}$	$\nu_{\text{C=O}}$	$\nu_{\text{as(-COO-)}}$	$\nu_{\text{s(-COO-)}}$	$\nu_{\text{C-N}}$	$\nu_{\text{C=C}}$	$\nu_{\text{C-H}}$
MAA	2969	1737			1640		
AA	3447	1724			1636		
BA	3418	1687			1601		
SA	3386	1694					
phen	3391				1643	1587	853,728
Eu(MAA) ₃ phen	3445		1562	1427	1645	1529	848,019
Eu(AA) ₃ phen	3409		1597	1453	1643	1547	848,723
Eu(BA) ₃ phen	3413		1567	1422	1611	1531	850,705
Eu ₂ (SA) ₃ phen ₂	3415		1569	1427		1533	851,664

to 1645 cm^{-1} . The stretching vibration peak ($\nu_{\text{C=C}}$) changed from 1587 cm^{-1} in phen to 1529 cm^{-1} in coordinated Eu(MAA)₃phen, 1547 cm^{-1} in coordinated Eu(AA)₃phen, 1531 cm^{-1} in coordinated Eu(BA)₃phen and 1533 cm^{-1} in coordinated Eu₂(SA)₃phen₂, respectively. The absorption band ($\nu_{\text{C-H}}$) shifted from 853 cm^{-1} in the phen to 848 cm^{-1} in the series complexes. These results indicated that europium ions are bonded with nitrogen atoms of the heterocyclic ligand phen [20]. The stretching vibration peak ($\nu_{\text{O-H}}$) at about 3445 cm^{-1} was observed in the series complexes, implying that the complexes contain water molecules [1].

From the IR spectra, the complexes of Eu(MAA)₃phen, Eu(AA)₃phen, Eu(BA)₃phen and Eu₂(SA)₃phen₂ with different MAA, AA, BA, and SA as the carboxylic acid ligands have been successfully synthesized.

3.2. Thermal Properties of Eu(Lc)₃phen Powders. The thermal stability of rare earth organic complexes was studied by the TG-DSC analyses. Figure 3 shows the TG-DSC curves of Eu(AA)₃phen. Eu(AA)₃phen began to decompose from about 190°C and decomposed completely at about 800°C . The TG curve exhibited a little mass loss from 50 to 190°C , indicating that the series complexes have little water. A loss step with weight loss rate of 28.06% arose in the range of $285\text{--}326^\circ\text{C}$, which was caused by the skeleton fracture of

the complex. It indicates that the complex has been partially decomposed which may be from the decomposition of free ligand AA and part decomposition of phen. It arose an exothermic peak at 340°C accompanied by a slow weight loss process. This may be generated by further heat of the intermediate products produced in the decomposition process of complexes [11]. The complexes began to turn into violent decomposition at 426.9°C taking off the AA and phen with weight loss to 25.07%. The DSC curves tend to be flat when closed to 800°C . Complexes decomposed completely with residue of rare earth oxides. Residual quantity bigger than the theoretical value may because of it was tested in the nitrogen atmosphere. In the environment which is lack of oxygen, the carbon atom in the complexes cannot completely transform into CO₂ or CO which carbonization phenomenon occurs [21].

The similar thermal analysis curves show the series complexes have similar thermal decomposition process. The thermal decomposition temperature of Eu(MAA)₃phen, Eu(AA)₃phen, Eu(BA)₃phen, and Eu₂(SA)₃phen₂ is about 210°C , 190°C , 200°C , and 180°C . The results show that these series complexes have good thermal stability.

3.3. Energy Absorption of Eu(Lc)₃phen Powders. Figure 4 shows the UV-Vis absorption spectra of five different ligands. The UV absorption of the phen is significantly stronger than

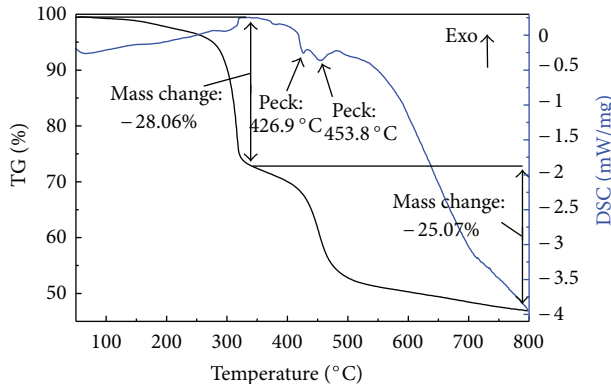
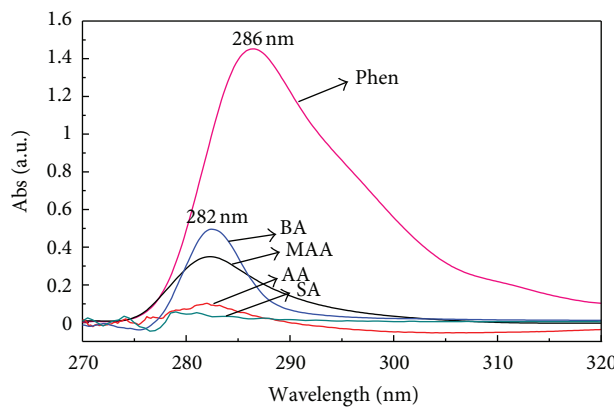
FIGURE 3: TG-DSC curves of $\text{Eu}(\text{AA})_3\text{phen}$.

FIGURE 4: The UV-Vis absorption spectra of ligands.

the various carboxylic acid ligands. A large absorption peak occurred at 286 nm and a weak absorption peak at 324 nm. It can be seen that the maximal peaks were located at 282 nm for carboxylic acid ligands, which was attributed to the $\pi \rightarrow \pi^*$ transition [22]. The ligand BA absorption in the ultraviolet region is relatively the strongest, followed by the MAA and AA, and SA was the weakest. It implies that most of the energy absorption comes from phen, which suggests that the antenna effect of phen is more efficient than that of carboxylic acid ligands.

From the UV-Vis absorption of the complexes, phen in the complexes is not only a coligand to transfer energy, but also the main components of the absorption energy, providing additional energy for the complex fluorescence emission.

The UV-Vis absorption spectra of $\text{Eu}(\text{Lc})_3\text{phen}$ complexes are shown in Figure 5. As the absorption of rare earth ions is weak in the ultraviolet region, it is overlapped by the absorption of the ligand. The complex absorption peak relative to the ligand is slightly red shifted and the intensity increases. The absorption intensity order in the ultraviolet region is BA > MAA > AA > SA, the corresponding complexes of UV-Vis absorption intensity of $\text{Eu}(\text{AA})_3\text{phen} > \text{Eu}(\text{MAA})_3\text{phen} > \text{Eu}(\text{BA})_3\text{phen} > \text{Eu}_2(\text{SA})_3\text{phen}_2$ in the complexes. This phenomenon attributes to the mutual effect

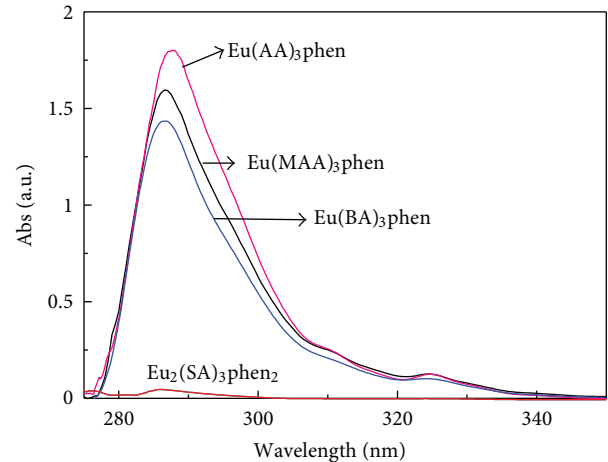


FIGURE 5: The UV-Vis absorption spectra of complexes.

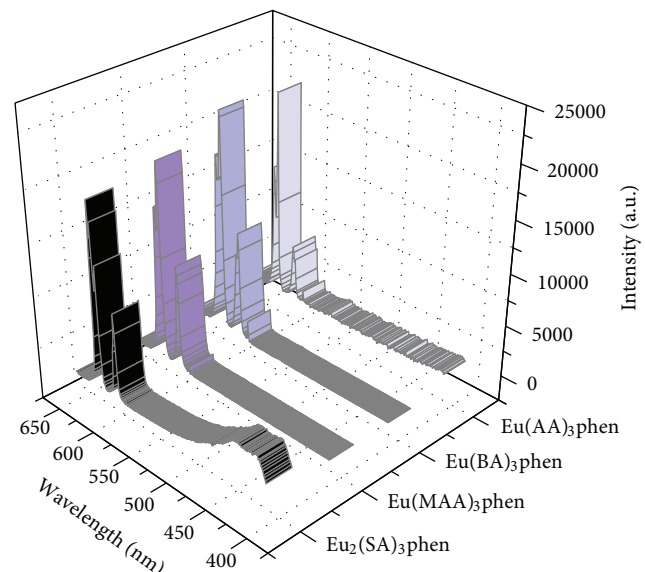


FIGURE 6: Complexes in optimal excitation wavelength stimulated emission spectrum.

of the carboxylic acid ligands and the electrically neutral ligand.

3.4. Luminescence of $\text{Eu}(\text{Lc})_3\text{phen}$ Powders. Figure 6 shows the emission spectra of $\text{Eu}(\text{MAA})_3\text{phen}$, $\text{Eu}(\text{AA})_3\text{phen}$, $\text{Eu}(\text{BA})_3\text{phen}$, and $\text{Eu}_2(\text{SA})_3\text{phen}_2$ complexes under the excitation of optimal excitation wavelength. The strongest excitation wavelengths of $\text{Eu}(\text{MAA})_3\text{phen}$, $\text{Eu}(\text{AA})_3\text{phen}$, $\text{Eu}(\text{BA})_3\text{phen}$, and $\text{Eu}_2(\text{SA})_3\text{phen}_2$ were 342 nm, 344 nm, 349 nm, and 368 nm, respectively. In the emission spectra, the positions of emission peaks of all complexes were almost the same. They all emitted the typical sharp emission bands at 590 and 614 nm, corresponding to the transitions of the ${}^5\text{D}_0 \rightarrow {}^7\text{F}_1$, ${}^5\text{D}_0 \rightarrow {}^7\text{F}_2$ of Eu^{3+} ion [23]. The local symmetry of the crystal field around the Eu^{3+} will cause

peak splitting. Therefore, in Figure 6, emission peak appears at 620 nm from the 614 nm due to the formation of split peak. Adding different carboxylic acid ligands changes the luminescence intensity of complexes without changing their positions of emission peaks.

Different carboxylic acid ligands caused that the coordination environment has changed, luminescence intensity of these four complexes subjected to the impacted. In addition, the luminescence intensity of Eu(BA)₃phen and Eu(AA)₃phen is stronger than that of Eu(MAA)₃phen and Eu₂(SA)₃phen₂.

From the front UV-Vis absorption spectrum, it is indicated that different carboxylic acid ligands and phen provided additional energy for the series complexes. Phen is the main source of energy for the complexes. The lowest triplet state energy level of the MAA and AA is at about 24800 cm⁻¹. And the lowest triplet state energy level of the phen is at about 22132 cm⁻¹. They are close to the excited state energy level of europium ion (17300 cm⁻¹ for the ⁵D₀ level) [24]. So the energy can be transferred to the excited states of europium ions effectively. The structure of the ligand plays an important role in the luminescence properties of complexes. Generally, the higher rigidity of the ligand is conducive to enhance fluorescence efficiency of the complexes [25, 26]. Benzoic acid has high conjugated rigid. Consequently, the fluorescence intensity of Eu(BA)₃phen is the highest.

Although succinic acid and its complex exhibited weak absorption in the ultraviolet region but the dicarboxylic acid has better transfer efficiency relative to a monobasic acid. It compensated for the lack of fluorescence properties to some extent caused by the weak ligand absorption [27]. Succinic acid is capable of delivering more efficient energy to complexes. It is also conducive to enhance the fluorescence intensity of the complexes.

4. Conclusion

In this paper, series of rare earth Europium complexes with different carboxylic acid ligands Eu(Lc)₃phen (Lc = MAA, AA, BA, SA) were synthesized. The complexes with good crystallization showed relatively high thermal stability and their decomposition temperatures were above 180°C. The energy of the series rare earth organic complexes mainly depends on the absorption of the carboxylic acid ligands and 1,10-Phenanthroline monohydrate. The ability to absorb energy of carboxylic acid ligands is BA > MAA > AA > SA. The ability to absorb energy of the formatted complexes was Eu(AA)₃phen > Eu(MAA)₃phen > Eu(BA)₃phen > Eu₂(SA)₃phen₂. The steric hindrance effect and level matches between the carboxylic acid ligands and heterocyclic ligand have a significant impact on the energy absorption efficiency of complexes. The fluorescence intensity of the series rare earth complexes was Eu(BA)₃phen > Eu(AA)₃phen > Eu(MAA)₃phen > Eu₂(SA)₃phen₂. All complexes show excellent luminescence characteristics. These results indicated that the series europium (III) complexes have great potential as the emission layer for organic molecular-based light-emitting diodes.

Acknowledgments

Authors would like to thank the generous financial support from National Defense Fundamental Research of China (6134502), Priority Academic Program Development of Jiangsu Higher Education Institutions (PAPD), Research and Innovation Program for College Graduates of Jiangsu Province (CXZZ12_0410), and National Natural Science Foundation of China (51202111).

References

- [1] X. Liu, S. Gao, L. Wang, L. Shen, J. Jiang, and J. Gao, "Synthesis, luminescent properties, and theoretical study of novel Sm³⁺ and Dy³⁺ complexes containing β -diketone and 1,10-phenanthroline," *Rare Metals*, vol. 30, no. 1, pp. 28–32, 2011.
- [2] Q. P. Li and B. Yan, "Multi-walled carbon nanotube-based ternary rare earth (Eu³⁺, Tb³⁺) hybrid materials with organically modified silica-oxygen bridge," *Journal of Colloid and Interface Science*, vol. 380, no. 1, pp. 67–74, 2012.
- [3] T. J. Moelbroek, P. Gamez, A. Pevec et al., "Efficient, stable, tunable, and easy to synthesize, handle and recycle luminescent materials: [H₃NMe₂]₃[Ln(III)(2,6-dipicolinolate)₃] (Ln = Eu, Tb, or its solid solutions)," *Dalton Transactions*, vol. 39, no. 28, pp. 6483–6487, 2010.
- [4] S. I. Weissman, "Intramolecular energy transfer the fluorescence of complexes of Europium," *The Journal of Chemical Physics*, vol. 10, no. 4, pp. 214–217, 1942.
- [5] P. Shukla, V. Sudarsan, R. K. Vatsa, S. K. Nayak, and S. Chattopadhyay, "Effect of symmetric substitution on the phenyl groups of Eu³⁺-dibenzoyl methane complexes on their luminescence properties," *Journal of Luminescence*, vol. 130, no. 10, pp. 1952–1957, 2010.
- [6] X. Zhao, K. Huang, F. Jiao, Z. Li, and X. Peng, "Fluorescence enhancement and cofluorescence in complexes of terbium(III) with trimellitic acid," *Rare Metals*, vol. 25, no. 2, pp. 144–149, 2006.
- [7] Y.-J. Gu, B. Yan, and Y.-Y. Li, "Ternary europium mesoporous polymeric hybrid materials Eu(β -diketonate)₃pvpd-SBA-15(16): host-guest construction, characterization and photoluminescence," *Journal of Solid State Chemistry*, vol. 190, pp. 36–44, 2012.
- [8] M. Hilder, P. C. Junk, U. H. Kynast, and M. M. Lezhnina, "Spectroscopic properties of lanthanoid benzene carboxylates in the solid state: part 1," *Journal of Photochemistry and Photobiology A*, vol. 202, no. 1, pp. 10–20, 2009.
- [9] N. Kerbellec, D. Kustaryono, V. Haquin, M. Etienne, C. Daiguebonne, and O. Guillou, "An unprecedented family of lanthanide-containing coordination polymers with highly tunable emission properties," *Inorganic Chemistry*, vol. 48, no. 7, pp. 2837–2843, 2009.
- [10] B. Li, Q. Y. Chen, Y. C. Wang, J. Huang, and Y. Li, "Synthesis, characterization and fluorescence studies of a novel europium complex based sensor," *Journal of Luminescence*, vol. 130, no. 12, pp. 2413–2417, 2010.
- [11] Y. Chen, J. Zhang, L. Zhang, P. Han, L. Wang, and Q. Zhang, "Synthesis and co-luminescence properties of Tb³⁺-methacrylic acid-1, 10-phenanthroline complexes doped with Eu³⁺ ions," *Rare Metals*, vol. 31, no. 5, pp. 479–483, 2011.
- [12] M. Pope, H. P. Kallmann, and P. Magnante, "Electroluminescence in organic crystals," *The Journal of Chemical Physics*, vol. 38, no. 8, pp. 2042–2043, 1963.

- [13] L. M. Zhao and B. Yan, "Novel polymer-inorganic hybrid materials fabricated with in situ composition and luminescent properties," *Journal of Non-Crystalline Solids*, vol. 353, no. 52-54, pp. 4654–4659, 2007.
- [14] Y. Xu, H. Wang, C. L. Song, H. F. Zhou, and B. S. Xu, "Synthesis and luminescence characteristics of near-white light-emitting copolymer," *Chinese Journal of Luminescence*, vol. 31, no. 2, pp. 274–278, 2010.
- [15] Y. Luo, S. Li, J. Li, X. Chen, and R. Tang, "Synthesis, fluorescence properties of Tb(III) complexes with novel mono-substituted β -diketone ligands," *Journal of Rare Earths*, vol. 28, no. 5, pp. 671–675, 2010.
- [16] W. G. Quirino, C. Legnani, M. Cremona, P. P. Lima, S. A. Junior, and O. L. Malta, "White OLED using β -diketones rare earth binuclear complex as emitting layer," *Thin Solid Films*, vol. 494, no. 1-2, pp. 23–27, 2006.
- [17] G. W. Lü, Y. Li, W. H. Li, Y. Z. Xu, and W. M. Du, "The luminescence character of Eu complexes with derivatives of benzoic acid and different second ligands," *Spectroscopy and Spectral Analysis*, vol. 23, no. 2, pp. 307–310, 2003.
- [18] D. Liu, C. Bao, Y. Zhao, and A. Wu, "Synthesis and luminescence properties of rare earth and organic ligands ternary complexes," *China Light & Lighting*, vol. 7, pp. 5–9, 1998.
- [19] L. Yu and H. Liu, "The progress of photoluminescent properties of rare-earth-ions-doped phosphate one-dimensional nanocrystals," *Journal of Nanomaterials*, vol. 2010, Article ID 461309, 6 pages, 2010.
- [20] W. J. Chai, W. X. Li, X. J. Sun, T. Ren, and X. Y. Shi, "Fluorescence enhancement of lanthanide(III) perchlorate by 1,10-phenanthroline in bis(benzoylmethyl) sulfoxide complexes and luminescence mechanism," *Journal of Luminescence*, vol. 131, no. 2, pp. 225–230, 2011.
- [21] X. Liu, J. Jiang, S. Yong, Y. Guo, K. Yang, and L. Wang, "Synthesis and fluorescence properties of Eu(III), Tb(III) and Sm(III) with beta-diketone and 2, 2'-bipyridine," *Journal of Rare Earths*, vol. 30, no. 6, pp. 520–523, 2012.
- [22] V. Divya, R. O. Freire, and M. L. P. Reddy, "Tuning of the excitation wavelength from UV to visible region in Eu³⁺- β -diketonate complexes: comparison of theoretical and experimental photophysical properties," *Dalton Transactions*, vol. 40, no. 13, pp. 3257–3268, 2011.
- [23] S. V. Eliseeva and J.-C. G. Bünzli, "Lanthanide luminescence for functional materials and bio-sciences," *Chemical Society Reviews*, vol. 39, no. 1, pp. 189–227, 2010.
- [24] S. Sato and M. Wada, "Relations between intramolecular energy transfer efficiencies and triplet state in rare earth β -diketone chelates," *Bulletin of the Chemical Society of Japan*, vol. 43, no. 7, pp. 1955–1962, 1970.
- [25] Y. Ruan, Q. Xiao, W. Luo, R. Li, and X. Chen, "Optical properties and luminescence dynamics of Eu³⁺-doped terbium orthophosphate nanophosphors," *Nanotechnology*, vol. 22, no. 27, Article ID 275701, 2011.
- [26] X. Wang, Q. Yan, P. Chu et al., "Analysis on fluorescence of dual excitable Eu(TTA)₃DPBT in toluene solution and PMMA," *Journal of Luminescence*, vol. 131, no. 8, pp. 1719–1723, 2011.
- [27] S. Fang, C. Wang, M. Hu et al., "Preparation and characterization of a series of novel Eu^{III}-complex-polyurethane acrylate materials based on mixed 6-hydroxy-1-naphthoate and 1, 10-phenanthroline ligands," *Journal of Applied Polymer Science*, vol. 125, no. 5, pp. 3404–3409, 2012.

Research Article

Concentration Dependence of Luminescent Properties for $\text{Sr}_2\text{TiO}_4:\text{Eu}^{3+}$ Red Phosphor and Its Charge Compensation

Zhou Lu, Le Zhang, Lixi Wang, and Qitu Zhang

College of Materials Science and Engineering, Nanjing University of Technology, Jiangsu, Nanjing 210009, China

Correspondence should be addressed to Qitu Zhang, zhqt@njut.edu.cn

Received 10 October 2012; Revised 12 December 2012; Accepted 13 December 2012

Academic Editor: Su Chen

Copyright © 2012 Zhou Lu et al. This is an open access article distributed under the Creative Commons Attribution License, which permits unrestricted use, distribution, and reproduction in any medium, provided the original work is properly cited.

$\text{Sr}_2\text{TiO}_4:\text{Eu}^{3+}$ phosphors using M^+ ($M = \text{Li}^+$, Na^+ , and K^+) as charge compensators were prepared by the solid-state reaction. The powders were investigated by powder X-ray diffraction (XRD) and photoluminescence spectra (PL) to study the phase composition, structure, and luminescent properties. The results showed that Li^+ ion was the best charge compensator. The phase was Sr_2TiO_4 when the doping concentration was small ($x \leq 10.0\%$). When x reached 15.0%, the phase turned into $\text{Sr}_3\text{Ti}_3\text{O}_7$ because of the structure damage. The phosphor could be effectively excited by ultraviolet (365, 395 nm) and blue light (465 nm), and then it emitted intense red light that peaked at around 620 nm (${}^5\text{D}_0 \rightarrow {}^7\text{F}_2$). In addition, the emission of 700 nm (${}^5\text{D}_0 \rightarrow {}^7\text{F}_4$) enhanced the red light color purity. The CIE chromaticity coordinates of samples with the higher red emission were between (0.650, 0.344) and (0.635, 0.352). Doped layered titanate $\text{Sr}_2\text{TiO}_4:\text{Eu}^{3+}$ is a promising candidate red phosphor for white LEDs which can be suited for both near-UV LED chip and blue LED chip.

1. Introduction

White light-emitting diodes (LEDs) are considered to be next-generation lighting devices. They have many advantages such as energy saving, environment friendliness, and small size [1–3]. Phosphor conversion method is a principal method in all the technologies to achieve white light owing to its easy achievement, high efficiency, and low cost.

The combination of blue chip and yellow phosphors has already been developed and is commercially available, but the lack of red emitting makes the color rendering index (CRI) lower [4]. The other tricolor white LEDs consisting of red, green, and blue (RGB) phosphors excited with a UV chip emitting 400 nm also have challenges. The luminescence intensity of commercial red phosphors is much weaker than green and blue phosphors. For excellent color render index, both methods need efficient red phosphors that should have the excitation wavelength matching with the emission of the blue LEDs ($\lambda_{\text{em}} = 440\text{--}470\text{ nm}$) or the UV LEDs ($\lambda_{\text{em}} = 350\text{--}410\text{ nm}$). Therefore, the development of a red phosphor with high luminance and satisfactory chemical

stability is a key technology for achieving warm white LEDs.

As a result, a kind of red phosphor with perovskite structure attracts much attention [5–7]. Perovskite structure $\text{MTiO}_3:\text{Pr}^{3+}$ ($M = \text{Ca}$, Sr , and Ba) phosphors emitted intense red light at 610 nm when excited by UV-light [8, 9]. Its intensity was greatly enhanced by adding charge compensation agents such as Al^{3+} , Li^+ , and Na^+ [10–12]. The optimized excitation wavelength of $\text{CaTiO}_3:\text{Eu}^{3+}$ was 400 nm, suitable for near-ultraviolet (N-UV) LED chip and emitted red light at 618 nm [13, 14]. However, the intensity is not so high that more-efficient red phosphors are needed to achieve an acceptable efficiency for white LEDs. Layered perovskite compounds have longer distance between layers so that they have bigger doping concentration. Therefore, layered perovskite compounds are good host materials for phosphors. Sr_2TiO_4 is a typical layered perovskite compound. According to these, trivalent Europium ion-activated Sr_2TiO_4 phosphor is prepared by solid-state reaction, and its luminescence properties are investigated to see whether it has the potential to be a red phosphor for N-UV or blue light LED chip.

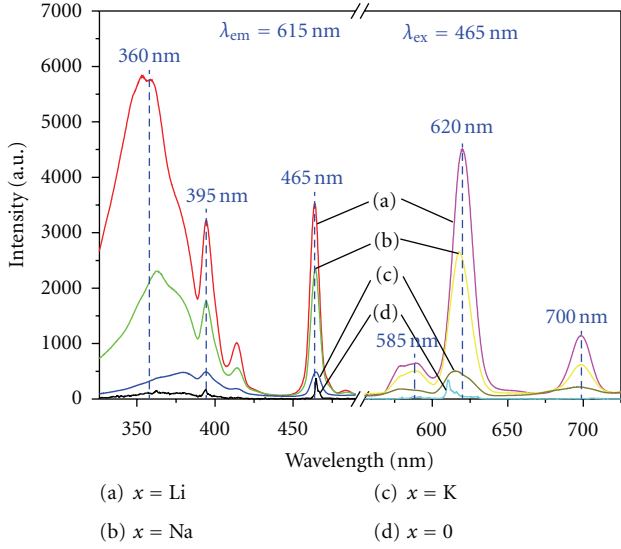


FIGURE 1: PL ($\lambda_{\text{ex}} = 465 \text{ nm}$) and PLE ($\lambda_{\text{em}} = 615 \text{ nm}$) spectra of $(\text{Sr}_{0.8}\text{Eu}_{0.1}\text{M}_{0.1})_2\text{TiO}_4$ phosphor with different charge compensation agents: (a) M = Li (b) M = Na, (c) M = K, and (d) without agents.

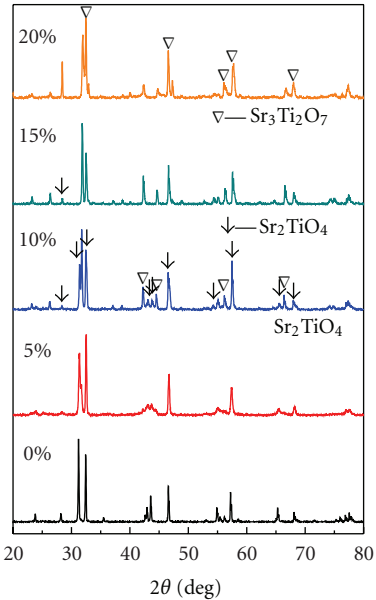


FIGURE 2: XRD patterns of $(\text{Sr}_{1-x}\text{Eu}_x\text{Li}_x)_2\text{TiO}_4$ powders (x (mol%) = 0.0, 5.0, 10.0, 15.0, 20.0).

2. Experimental

2.1. Sample Preparation. All powder samples were synthesized through the solid-state reaction technique. High-purity SrCO_3 , TiO_2 (analytical grade) and Eu_2O_3 (>99.99%) were mixed thoroughly in alcohol by ball milling and then dried. Appropriate amounts of Li_2CO_3 , Na_2CO_3 , or K_2CO_3 (analytical grade) were added as the charge compensators. The synthesis was performed at 1100°C for 2 h under air atmosphere in electric tube furnace. Series of

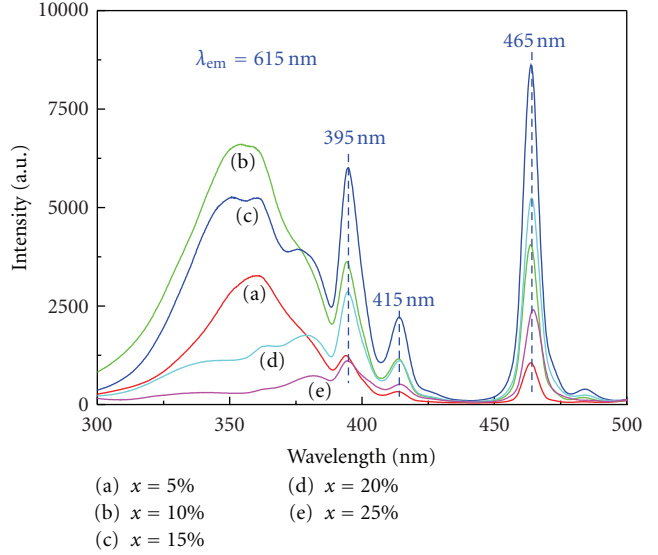


FIGURE 3: (a) Excitation spectra ($\lambda_{\text{em}} = 615 \text{ nm}$) of $(\text{Sr}_{1-x}\text{Eu}_x\text{Li}_x)_2\text{TiO}_4$: (a) $x = 5.0\%$, (b) $x = 10.0\%$, (c) $x = 15.0\%$, (d) $x = 20.0\%$, (e) $x = 25.0\%$, and (b) Gaussian peak fitting of the $(\text{Sr}_{0.7}\text{Eu}_{0.15}\text{Li}_{0.15})_2\text{TiO}_4$ phosphor powder.

$(\text{Sr}_{1-2x}\text{Eu}_x\text{M}_x)_2\text{TiO}_4$ ($\text{M} = \text{Li}^+, \text{Na}^+, \text{K}^+$; x (mol%) = 5.0, 10.0, 15.0, 20.0, 25.0) powders were prepared. SrCO_3 and Eu_2O_3 come from Sinopharm Chemical Reagent Co., Ltd., and Li_2CO_3 , Na_2CO_3 , K_2CO_3 and TiO_2 come from Shanghai Lingfeng Chemical Reagent CO., LTD.

2.2. Characterization. The crystalline phases of synthesized powders were determined by X-ray diffraction (XRD, D/Max2500, Rigaku, Japan) using $\text{Cu K}\alpha$ radiation ($\lambda = 1.5406 \text{ \AA}$) in the range of $5^\circ - 80^\circ$ with a step size of 0.02° . The photoluminescence spectra of the phosphors were measured using a fluorescent spectrophotometer (FL3-221, HORIBA, Jobin Yvon, France) at room temperature.

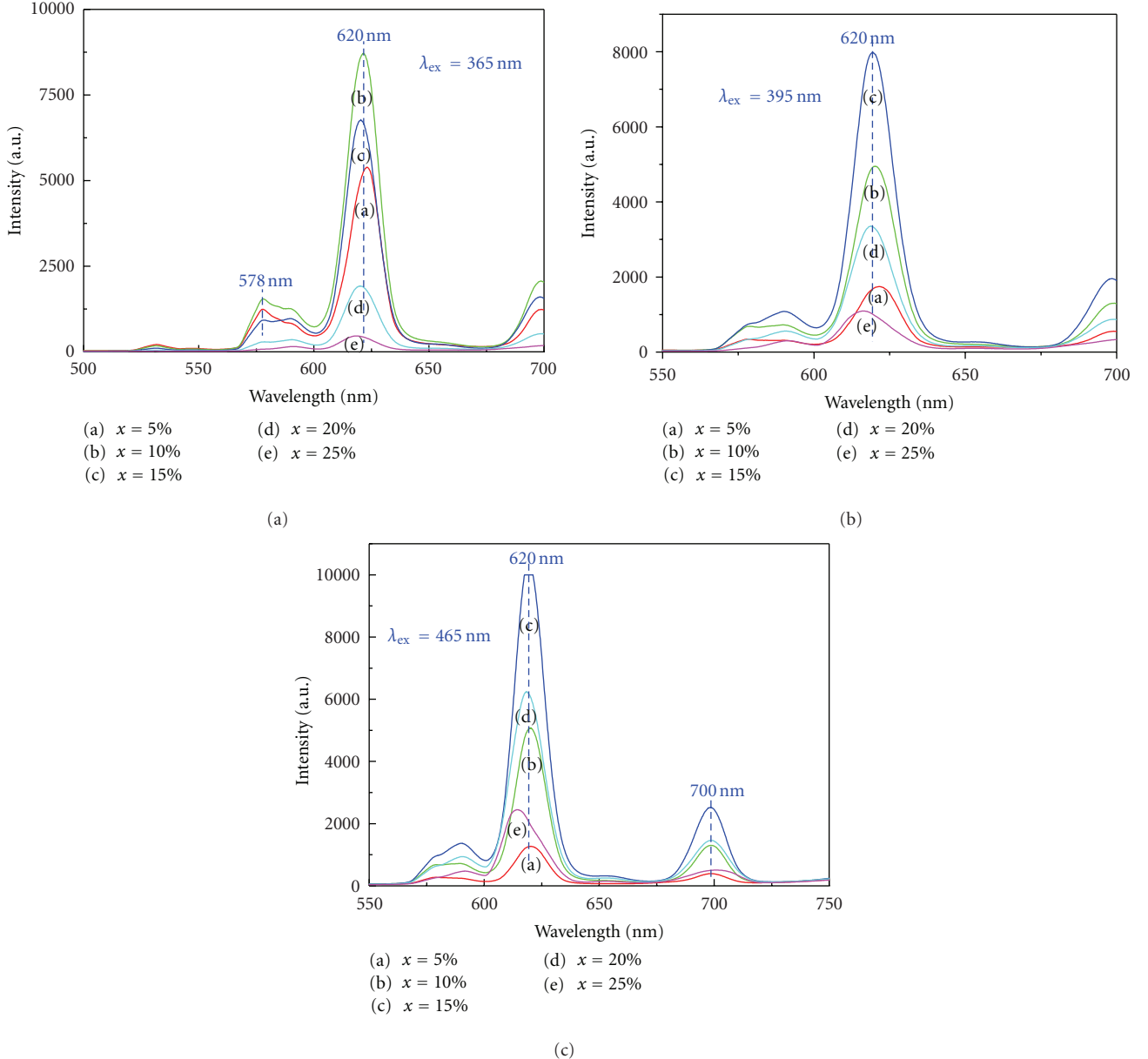


FIGURE 4: Emission spectra (a) $\lambda_{\text{ex}} = 365$ nm, (b) $\lambda_{\text{ex}} = 395$ nm, and (c) $\lambda_{\text{ex}} = 465$ nm of $(\text{Sr}_{1-x}\text{Eu}_x\text{Li}_x)_2\text{TiO}_4$ (a) $x = 5.0\%$, (b) $x = 10.0\%$, (c) $x = 15.0\%$, (d) $x = 20.0\%$, (e) $x = 25.0\%$.

3. Results and Discussion

3.1. The Choice of Charge Compensators. Eu³⁺ ions are expected to replace Sr²⁺ ions. It would be difficult to keep charge balance in the lattice. Therefore, Eu³⁺ ions may not be fully introduced into Sr²⁺ sites in order to keep charge balance. Eu³⁺ may exist in Eu₂O₃ state, and it would lead to the decrease of emission intensity. This problem can be solved by adding charge compensators. Li⁺, Na⁺, and K⁺ ions are always chosen as charge compensators for phosphors [15, 16]. Because the radii of Li⁺, Na⁺, and K⁺ are small which are easy to enter into lattice, and they are all of +1 valence which is convenient for charge compensation. Therefore, Li⁺, Na⁺, and K⁺ were added in the same molar

weight as Eu³⁺ to act as the charge compensators to improve the luminescence intensity of Sr₂TiO₄:Eu³⁺.

Figure 1 shows the excitation and emission spectra of $(\text{Sr}_{0.8}\text{Eu}_{0.1}\text{M}_{0.1})_2\text{TiO}_4$ phosphor with different charge compensators. The shape and positions were similar in the PL and PLE spectra for all the samples. Excitation and emission intensities were enhanced obviously after adding charge compensators. Before adding charge compensators, Eu^{3+} could not substitute Sr^{2+} sites totally in order to maintain chemically neutral $\text{Sr}_2\text{TiO}_4:\text{Eu}^{3+}$ phosphor. Some Eu^{3+} could not act as activated ions, and the impurity phase could interdict the energy transfer between matrix and activated ions and restrain the Sr_2TiO_4 grains growth during the

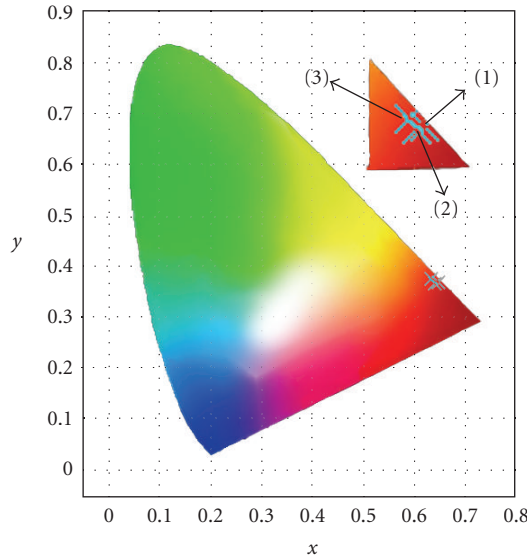


FIGURE 5: The CIE chromaticity coordinates of red phosphors: (1) $(\text{Sr}_{1-x}\text{Eu}_x\text{Li}_x)_2\text{TiO}_4$ ($\lambda_{\text{ex}} = 365 \text{ nm}$), (2) $(\text{Sr}_{0.7}\text{Eu}_{0.15}\text{Li}_{0.15})_2\text{TiO}_4$ ($\lambda_{\text{ex}} = 395 \text{ nm}$), (3) $(\text{Sr}_{0.7}\text{Eu}_{0.15}\text{Li}_{0.15})_2\text{TiO}_4$ ($\lambda_{\text{ex}} = 465 \text{ nm}$).

sintering process [17]. After adding charge compensators, Eu^{3+} ions were able to be fully introduced into Sr^{2+} sites, and charge compensators and vacancy could substitute Sr^{2+} sites so that SrO and Eu_2O_3 could react with TiO_2 to a great extent. In addition, Li_2CO_3 , Na_2CO_3 , and K_2CO_3 can act as flux agents to promote the formation of luminescence materials polycrystal. Compared with Na^+ and K^+ , the intensity was enhanced greatly when adding Li^+ as charge compensator. These phenomena are assigned to the fact that the ionic radius of Li^+ (0.92 Å) to the one of Sr^{2+} (1.31 Å) is the smallest, the one of Na^+ (1.24 Å) being second, and the one of K^+ (1.55 Å) is the biggest so that it develops the distortion grade different, which impacts on the luminous properties and crystal structures [18]. Thus, Li^+ is selected as charge compensator in the following experiments.

3.2. XRD of $(\text{Sr}_{1-x}\text{Eu}_x\text{Li}_x)_2\text{TiO}_4$ (x (mol%) = 0.0, 5.0, 10.0, 15.0, 20.0) Powders. Figure 2 shows the XRD patterns of Eu^{3+} ions doped Sr_2TiO_4 phosphors with different Li^+ concentration as charge compensator. At first, when the doping concentration was small ($x = 5.0\%$), all the peaks were indexed by Sr_2TiO_4 without any impurity. After x reached 10.0%, there appeared some $\text{Sr}_3\text{Ti}_2\text{O}_7$ peaks, but Sr_2TiO_4 was the major phase. When $x = 15.0\%$, $\text{Sr}_3\text{Ti}_2\text{O}_7$ turned to be the major phase, because the structure of Sr_2TiO_4 was damaged with the increase of Eu^{3+} and Li^+ . Until x came to 20.0%, the phase composition consisted of $\text{Sr}_3\text{Ti}_2\text{O}_7$ and some impurities, because the content of Sr^{2+} was too little and the radius of Li^+ was too small to support the whole structure. After doping Eu^{3+} , peaks shifted to higher 2θ values relatively, which indicated that Eu^{3+} had occupied the sites of Sr^{2+} , because the radius of Eu^{3+} is 1.12 Å ($\text{CN} = 9$), smaller than that of Sr^{2+} (1.31 Å, $\text{CN} = 9$). When

Eu^{3+} occupied the site of Sr^{2+} , the lattice would shrink so that the diffraction peaks would shift to high diffraction angles compared to pure Sr_2TiO_4 and $\text{Sr}_3\text{Ti}_2\text{O}_7$ [19].

3.3. Luminescent Properties of $(\text{Sr}_{1-x}\text{Eu}_x\text{Li}_x)_2\text{TiO}_4$ (x (mol%) = 5.0, 10.0, 15.0, 20.0) Phosphors. Figure 3(a) presents the excitation spectra of $(\text{Sr}_{1-x}\text{Eu}_x\text{Li}_x)_2\text{TiO}_4$ under different Eu^{3+} concentrations ($\lambda_{\text{em}} = 615 \text{ nm}$). The excitation spectra consisted of a wide excitation band from 325 to 425 nm and some sharp line peaks of characteristic transitions of Eu^{3+} . The broad band was a charge transfer band (CTB) which was caused by several charge transition. Figure 3(b) shows the results of Gaussian peak fitting of the PLE spectra of $(\text{Sr}_{0.7}\text{Eu}_{0.15}\text{Li}_{0.15})_2\text{TiO}_4$. Peak 1 (350 nm) was ascribed to the O → Ti of phase $\text{Sr}_3\text{Ti}_2\text{O}_7$, peak 2 (380 nm) was ascribed to the O → Ti of phase Sr_2TiO_4 , and peak 3 (362 nm) was ascribed to the O → Eu. The sum of deconvoluted curves (red dash line) was almost fitted with observed line (black solid line). The other intense 395, 465 and weak 415 nm excitation peaks related the intra-4f transitions from ground state 7F_0 to 5L_6 , 5D_2 , and 5D_3 , respectively. The shape and position were similar except that the intensity of absorption varied with the increase of Eu^{3+} concentration. What interests us is that the intensity of CTB is stronger than that of intra-4f transitions at lower Eu^{3+} concentration ($x \leq 10.0\%$), and it mainly performs wide band absorption of matrix. Then the intensity of CTB decreases with the increase of Eu^{3+} doping concentration. However, characteristic sharp line spectra increase continuously until $x = 15.0\%$, and it performs 395 and 465 nm intense linear excitation peaks. With the increase of Eu^{3+} and Li^+ , the phase composition changes from Sr_2TiO_4 to $\text{Sr}_3\text{Ti}_2\text{O}_7$ to some impurities, and impurity is bad for luminescence intensity. However, both intensity of CTB and intra-4f transitions are high when Eu^{3+} doped in layered titanate, and there is reason to believe that $\text{Sr}_2\text{TiO}_4:\text{Eu}^{3+}$ and even $\text{Sr}_3\text{Ti}_2\text{O}_7:\text{Eu}^{3+}$ are promising red phosphors for white LEDs.

Figures 4(a), 4(b), and 4(c) are the emission spectra of $(\text{Sr}_{1-x}\text{Eu}_x\text{Li}_x)_2\text{TiO}_4$ excited by 365, 395, and 465 nm, respectively. The shape and position of the emission spectra were similar, and they all emitted dominated intense 620 nm (${}^5D_0 \rightarrow {}^7F_2$) red light and weak 578 nm (${}^5D_0 \rightarrow {}^7F_1$), 700 nm (${}^5D_0 \rightarrow {}^7F_4$) light. ${}^5D_0 \rightarrow {}^7F_2$ and ${}^5D_0 \rightarrow {}^7F_4$ are electric dipole transitions of Eu^{3+} , which are very sensitive to the local environment around the Eu^{3+} , and depend on the symmetry of the crystal field. As we know, the transitions are forbidden when Eu^{3+} occupies centrosymmetric sites. The structure of Sr_2TiO_4 is tetragonal K_2NiF_4 type, and perovskite layers are interleaved with SrO layers. In Sr_2TiO_4 , all Sr ions occupy positions between the perovskite layers (9-oxygen-ion-coordinated sites with C_{4v} symmetry) [20]. Therefore, it indicates that Eu^{3+} has occupied the noncentrosymmetrical sites of Sr^{2+} . Compared with usual luminescence of Eu^{3+} (594, 615 nm) [21], the luminescence of Eu^{3+} in layered perovskite has some red shift which performs better red light color purity and higher luminescent intensity. In addition, the emission of 700 nm in some degree enhances red light color purity, too. Those are

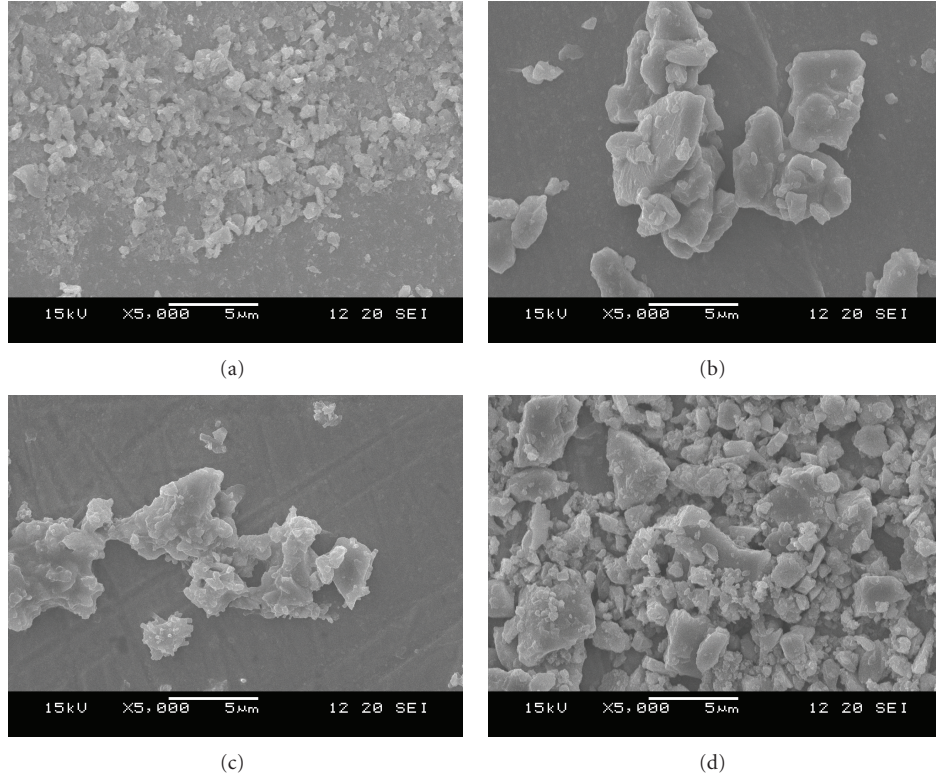


FIGURE 6: SEM micrographs of $(\text{Sr}_{1-x}\text{Eu}_x\text{Li}_x)_2\text{TiO}_4$ phosphor powders: (a) $x = 5.0\%$, (b) $x = 10.0\%$, (c) $x = 15.0\%$, and (d) $x = 20.0\%$.

more beneficial to make it become a red light compensation material for white LEDs.

The emission intensity was found to increase with the increase of Eu^{3+} concentration up to 10.0 mol% ($\lambda_{\text{ex}} = 365 \text{ nm}$). While excited at 395 and 465 nm, the best doping concentration was 15.0 mol%. Because, when $x = 10.0\%$, the phase is Sr_2TiO_4 and TiO_4^{4-} group has strong absorption at UV light region [22], it has the strongest luminescence intensity when excited at 365 nm. However, when $x = 15.0\%$, the phase is $\text{Sr}_3\text{Ti}_2\text{O}_7$. The crystal system of $\text{Sr}_3\text{Ti}_2\text{O}_7$ is tetragonal, and double perovskite layers are interleaved with SrO layers. In $\text{Sr}_3\text{Ti}_2\text{O}_7$, some Sr ions occupy positions between the perovskite layer (9-oxygen-ion-coordinated sites with C_{4v} symmetry), and the other Sr ions occupy positions in the center of the perovskite layer (12-oxygen-ion-coordinated sites with D_{4h} symmetry) [20]. In spite of the 12-oxygen-ion-coordinated sites in $\text{Sr}_3\text{Ti}_2\text{O}_7$, 9-oxygen-ion-coordinated sites are vast majority; therefore, it emits characteristic intense red light of Eu^{3+} which is sensitive to the surrounding symmetry of the crystal field. Usually, Eu^{3+} doping concentration is less than 5.0% in normal phosphor. However, the doping concentration of Eu^{3+} is up to or even over 10.0% in Sr_2TiO_4 and $\text{Sr}_3\text{Ti}_2\text{O}_7$ host. The main reason is that layered perovskite has SrO layers interleaved in perovskite layers, and it makes bigger space between layers so that they have bigger doping concentration which leads to the higher luminescence intensity. In conclusion, layered titanate is a good matrix for phosphors, and Eu^{3+} doped

layered titanate is a good red phosphor for white LEDs which can be suited for both near-UV LED chip and blue LED chip.

The samples that are emitting most intense red light respectively excited at 365, 395, and 465 nm are chosen to calculate their CIE chromaticity coordinates. The corresponding CIE chromaticity coordinates using symbol “ x ” to indicate their positions are shown in Figure 5, and they change between (0.650, 0.344) and (0.635, 0.352), which is due to the variability of the relative intensities of 620 nm and 700 nm mainly. They are all close to coordinates of the “ideal red” which is (0.67, 0.33) [23]. In addition, their CIE chromaticity coordinates are rather close the edge of CIE diagram, indicating that this kind of phosphors shows better color purity in solid-state lighting.

3.4. SEM of $(\text{Sr}_{1-x}\text{Eu}_x\text{Li}_x)_2\text{TiO}_4$ (x (mol%) = 5.0, 10.0, 15.0, 20.0) Phosphor Powders. It is well known that crystallinity and surface morphology of phosphors has a strong effect on the luminescence properties. Figure 6 shows the SEM morphology of $(\text{Sr}_{1-x}\text{Eu}_x\text{Li}_x)_2\text{TiO}_4$ with different Eu^{3+} concentration. The particles enlarged with the increase of Eu^{3+} and Li^+ concentration, and all presented irregular polygon. The particle size was about 1 μm when $x = 5.0\%$ and kept around 5 μm when x reached 10.0%, 15.0%, and 20.0% which corresponded with the requirements of particle size to phosphor. It has been established that Li^+ was conducive to the formation of crystalline phase, and it is mainly because of the function of Li_2CO_3 flux [24]. However, the special doping

concentration of active Eu³⁺ also has some influence on the particle size [25].

4. Conclusions

In this paper, Sr₂TiO₄:Eu³⁺, M⁺ (M = Li⁺, Na⁺, and K⁺) phosphors were synthesized through the solid-state reaction. M⁺ as charge compensators led to the increase of emission intensity, and Li⁺ was confirmed to be the best charge compensator. The excitation spectra consisted of a wide excitation band and some sharp line peaks of characteristic transitions of Eu³⁺ when Eu³⁺ doping concentration is low ($x \leq 10.0\%$), the phase is Sr₂TiO₄, and the intensity excited by CTB (365 nm) is stronger than that of intra-4f transitions. After x reached 15.0%, the structure damaged and the phase became Sr₃Ti₂O₇. The intensity excited by CTB became weaker and characteristic emission peaks of Eu³⁺ stronger when excited at 395 and 465 nm. Because Sr₂TiO₄ has strong absorption at UV light region, while Sr₃Ti₂O₇ has two layers and there are more noncentersymmetrical Sr²⁺ sites for substituting. Those phosphors all exhibited intense 620 nm (⁵D₀ → ⁷F₂) red light and weak 578 nm (⁵D₀ → ⁷F₁), 700 nm (⁵D₀ → ⁷F₄) light. The CIE chromaticity coordinates of three samples that are emitting most intense red light change between (0.650, 0.344) and (0.635, 0.352), close to coordinates of the “ideal red” which is (0.67, 0.33). The particle size meets the demands of phosphor. Doped layered titanate Sr₂TiO₄:Eu³⁺ is a promising candidate red phosphor for white LEDs which can be suited for both near-UV LED chip and blue LED chip.

Acknowledgments

The authors would like to thank the generous financial support from National Defense Fundamental Research of China (6134502), Priority Academic Program Development of Jiangsu Higher Education Institutions (PAPD), Research and Innovation Program for College Graduates of Jiangsu Province (CXZZ12.0410), and National Natural Science Foundation of China (51202111).

References

- [1] S. Ye, F. Xiao, Y. X. Pan, Y. Y. Ma, and Q. Y. Zhang, “Phosphors in phosphor-converted white light-emitting diodes: recent advances in materials, techniques and properties,” *Materials Science and Engineering R*, vol. 71, no. 1, pp. 1–34, 2010.
- [2] P. Walterteit, O. Brandt, A. Trampert et al., “Nitride semiconductors free of electrostatic fields for efficient white light-emitting diodes,” *Nature*, vol. 406, no. 6798, pp. 865–868, 2000.
- [3] B. W. D’Andrade and S. R. Forrest, “White organic light-emitting devices for solid-state lighting,” *Advanced Materials*, vol. 16, no. 18, pp. 1585–1595, 2004.
- [4] Z. L. Wang, Y. L. Zhang, L. Xiong, X. F. Li, J. M. Guo, and M. L. Gong, “A potential red-emitting phosphor with high color-purity for near-UV light emitting diodes,” *Current Applied Physics*, vol. 12, no. 4, pp. 1084–1087, 2012.
- [5] P. Psuja, D. Hreniak, and W. Strek, “Rare-earth doped nanocrystalline phosphors for field emission displays,” *Journal of Nanomaterials*, vol. 2007, Article ID 81350, 7 pages, 2007.
- [6] V. Sivakumar and U. V. Varadaraju, “Synthesis, phase transition and photoluminescence studies on Eu³⁺-substituted double perovskites—a novel orange-red phosphor for solid-state lighting,” *Journal of Solid State Chemistry*, vol. 181, no. 12, pp. 3344–3351, 2008.
- [7] T. C. Ozawa, K. Fukuda, K. Akatsuka, Y. Ebina, and T. Sasaki, “Preparation and characterization of the Eu³⁺ doped perovskite nanosheet phosphor: La_{0.90}Eu_{0.05}Nb₂O₇,” *Chemistry of Materials*, vol. 19, no. 26, pp. 6575–6580, 2007.
- [8] R. Fujiwara, H. Sano, M. Shimizu, and M. Kuwabara, “Quantitative analysis of UV excitation bands for red emissions in Pr³⁺-doped CaTiO₃, SrTiO₃ and BaTiO₃ phosphors by peak fitting,” *Journal of Luminescence*, vol. 129, no. 3, pp. 231–237, 2009.
- [9] S. Okamoto and H. Yamamoto, “Luminescent properties of praseodymium-doped alkaline-earth titanates,” *Journal of Luminescence*, vol. 102–103, pp. 586–589, 2003.
- [10] R. Chen, F. Song, D. Chen, and Y. Peng, “Improvement of the luminescence properties of CaTiO₃:Pr obtained by modified solid-state reaction,” *Powder Technology*, vol. 194, no. 3, pp. 252–255, 2009.
- [11] P. T. Diallo, P. Boutinaud, R. Mahiou, and J. C. Cousseins, “Red luminescence in Pr³⁺-doped calcium titanates,” *Physica Status Solidi A*, vol. 160, no. 1, pp. 255–263, 1997.
- [12] N. Suriyamurthy and B. S. Panigrahi, “Investigations on luminescence of rare earths doped CaTiO₃:Pr³⁺ phosphor,” *Journal of Rare Earths*, vol. 28, no. 4, pp. 488–492, 2010.
- [13] J. Fu, Q. Zhang, Y. Li, and H. Wang, “Preparation and photoluminescence characteristics of a new promising red NUV phosphor CaTiO₃:Eu³⁺,” *Journal of Alloys and Compounds*, vol. 485, no. 1–2, pp. 418–421, 2009.
- [14] J. Fu, Q. Zhang, Y. Li, and H. Wang, “Highly luminescent red light phosphor CaTiO₃:Eu³⁺ under near-ultraviolet excitation,” *Journal of Luminescence*, vol. 130, no. 2, pp. 231–235, 2010.
- [15] H. Liu, Y. Hao, H. Wang, J. Zhao, P. Huang, and B. Xu, “Luminescent properties of R⁺ doped Sr₂TiO₄:Eu³⁺ (R⁺ = Li⁺, Na⁺ and K⁺) red-emitting phosphors for white LEDs,” *Journal of Luminescence*, vol. 131, no. 11, pp. 2422–2426, 2011.
- [16] L. S. Zhao, J. Liu, Z. C. Wu, and S. P. Kuang, “Optimized photoluminescence of Sr₂TiO₄:Eu³⁺ red-emitting phosphor by charge compensation,” *Spectrochimica Acta A*, vol. 87, pp. 228–231, 2012.
- [17] J. Liu, H. Lian, and C. Shi, “Improved optical photoluminescence by charge compensation in the phosphor system CaMoO₄:Eu³⁺,” *Optical Materials*, vol. 29, no. 12, pp. 1591–1594, 2007.
- [18] Y. J. Chen, F. B. Cao, Y. W. Tian, L. J. Xiao, and L. K. Li, “Optimized photoluminescence by charge compensation in a novel phosphor system,” *Physica B*, vol. 405, no. 1, pp. 435–438, 2010.
- [19] C. Jiang, L. Fang, M. Shen, F. Zheng, and X. Wu, “Effects of Eu substituting positions and concentrations on luminescent, dielectric, and magnetic properties of SrTiO₃ ceramics,” *Applied Physics Letters*, vol. 94, no. 7, Article ID 071110, 2009.
- [20] Y. Inaguma, D. Nagasawa, and T. Katsumata, “Photoluminescence of praseodymium-doped Sr_{n+1}TinO_{3n+1} (n = 1, 2, ∞),” *Japanese Journal of Applied Physics*, vol. 44, pp. 761–764, 2005.
- [21] T. Anh, P. Benalloul, C. Barthou, L. T. Giang, N. Vu, and L. Minh, “Luminescence, energy transfer, and upconversion mechanisms of Y₂O₃ nanomaterials doped with Eu³⁺, Tb³⁺, Tm³⁺, Er³⁺, and Yb³⁺ ions,” *Journal of Nanomaterials*, vol. 2007, Article ID 48247, 10 pages, 2007.

- [22] G. Blasse and A. Bril, "Fluorescence of Eu³⁺-activated sodium lanthanide titanates (NaLn_{1-x}Eu_xTiO₄)," *The Journal of Chemical Physics*, vol. 48, no. 8, pp. 3652–3656, 1968.
- [23] L. Zhang, Y. Li, J. Liu, P. Han, and Q. Zhang, "Preparation of homogeneous and ordered double-perovskite Sr₂CaMoO₆:Eu³⁺ phosphors and its luminescent properties," *Journal of Nanjing University of Technology*, vol. 34, no. 5, pp. 30–37, 2012.
- [24] H. K. Yang, J. W. Chung, B. K. Moon et al., "Synthesis and enhanced luminescence properties of Li-doped CaTiO₃:Pr³⁺ ceramic phosphors," *Solid State Sciences*, vol. 13, no. 7, pp. 1420–1423, 2011.
- [25] L. Lin and B. Yan, "Rare earth titanates ceramics Na₂La₂Ti₃O₁₀: Pr³⁺ and RE₂Ti₂O₇: Pr³⁺ (R = Gd, Y): sol-gel synthesis, characterization and luminescence," *Journal of Materials Science*, vol. 22, no. 6, pp. 672–678, 2011.

Research Article

Study on Pore Distribution and Formation Rule of Sepiolite Mineral Nanomaterials

Qingguo Tang,¹ Fei Wang,^{1,2} Mengran Tang,³ Jinsheng Liang,¹ and Chongyan Ren¹

¹ Institute of Power Source & Ecomaterials Science, Hebei University of Technology, Tianjin 300130, China

² Jiangsu Provincial Key Laboratory of Palygorskite Science and Applied Technology, Huaiyin Institute of Technology, Huai'an 223003, China

³ College of Engineering and Computing, Florida International University, Miami, FL 33174, USA

Correspondence should be addressed to Fei Wang, wangfei36777@163.com

Received 23 October 2012; Accepted 5 November 2012

Academic Editor: Su Chen

Copyright © 2012 Qingguo Tang et al. This is an open access article distributed under the Creative Commons Attribution License, which permits unrestricted use, distribution, and reproduction in any medium, provided the original work is properly cited.

Theoretical research and specific surface area analysis of nitrogen adsorption indicated that a lot of structural micropores exist in sepiolite minerals fibers. However, the microporous size, existing form, and the distribution relationship between microporous structures were not proved yet. In this paper, the section TEM samples of nanofibers were prepared on the basis of the metal embedding and cutting technique, and the inner structure of sepiolite nanofibers was observed by TEM. The results showed that sepiolite fibers have multiplayer structure similar to concentric circles, and many micropores with the size of about 2–5 nm are normal and parallel to the *c*-axis. The reason for the previously mentioned phenomenon was explained by using BET analysis and X-ray diffraction analysis results.

1. Introduction

Sepiolite is a kind of fibrous silicate clay mineral rich of magnesium with a structure of layer and chain. The study on structure of sepiolite could be dated back from 1930s, and Longchanbon studied the structure of sepiolite. Until 1955, Nagy and Bradley [1] proposed the first structural model and theoretical structure: $\text{Si}_{12}\text{Mg}_9\text{O}_{30}(\text{OH})_6(\text{OH}_2)_4 \cdot 6\text{H}_2\text{O}$. Nagy believed that sepiolite crystal was amphibole chain composed of two pyroxene chains, with silicon-oxy tetrahedron on each side in standard spacing. Two layers of silicon-oxy tetrahedron parallel to *c0* axis had six silicon-oxy tetrahedron, separately. Structure units are connected to each other by four oxygen atoms on the apex angle, which formed channels with a sectional area of $0.38 \times 0.94 \text{ nm}$ parallel to the chain.

Brauner and Preisinger [2] proposed the structural model of two amphibole chains composed by three pyroxene chains, as shown in Figure 1. According to Brauner's model, the theoretical structure of sepiolite was $\text{Si}_{12}\text{Mg}_8\text{O}_{30}(\text{OH})_4(\text{OH}_2)_4 \cdot 8\text{H}_2\text{O}$, whose fibrous structures were composed of two layers of silicon-oxy tetrahedron

units connected by oxygen atoms and central magnesium octahedron layers. Silicon-oxy tetrahedron layers were continuous, and were inverted at intervals of six tetrahedron units, leading to the existence of channels of dimensions of $0.37 \text{ nm} \times 1.06 \text{ nm}$ running parallel to the length of the fibers. The two models mentioned previously were not different obviously in terms of the sizes of crystal, but they had eight and nine of octahedron cations in Brauner's and Nagy's model, separately. Moreover, they had four hydroxyl groups, eight zeolite water, and sectional area of 0.3572 nm^2 in Brauner's model; six hydroxyl groups, six zeolite water, and sectional area of 0.3816 nm^2 in Nagy's model, separately. There were many reports about microstructure feature, crystal structure and thermal stability; however, the study on inner surface, adsorption, and channel structure of sepiolite was mainly by BET analysis [3–7]. The tested size and distribution of pores were different significantly from theoretical results due to the limitation of testing methods and accuracy [8–11].

In this paper, the inner structure of sepiolite nanofibers was observed by TEM in order to study the forms of existence

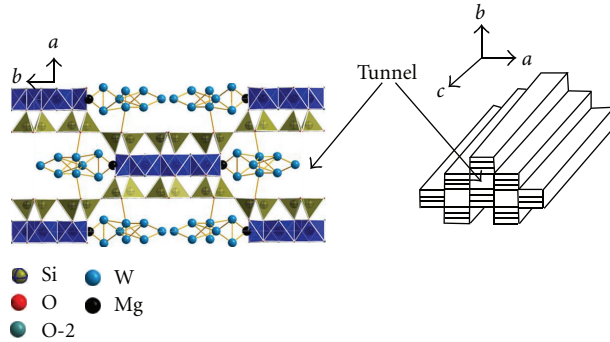


FIGURE 1: Crystal structure of sepiolite proposed by Brauner and Preisinger [2].

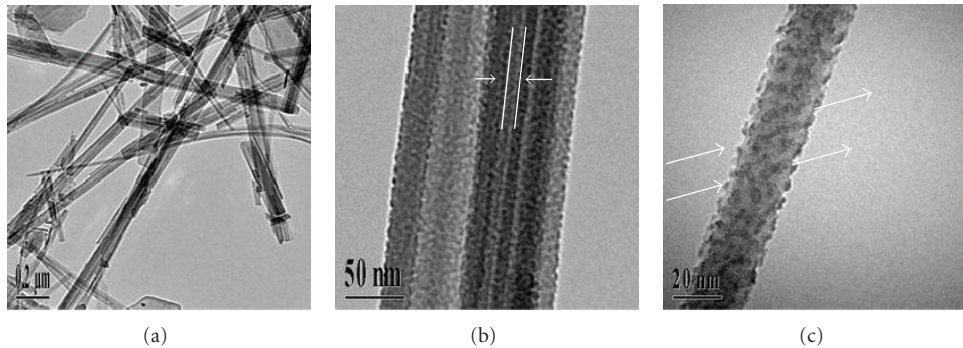


FIGURE 2: Microstructure of external surface of sepiolite samples.

and rules of distribution in sepiolite minerals fibers, which were further explained by using BET analysis and X-ray diffraction analysis results.

2. Experimental Details

Experimental details were as follows: hydrothermal sepiolite samples (Yi county, Hebei Province of China) were immersed in 0.1% of sodium pyrophosphate solution for 2 h in a reaction flask with stirring at a constant speed of 1500 rpm. Then the solutions were filtered and washed with distilled water until pH > 6.5. The samples were dried at 70°C for 8 h in the vacuum, and the purified samples were obtained. The process of TEM sample preparation is as follows [12]. A few sepiolite samples were placed on a polished metal strip, and the fine particles were encapsulated on the metal strip by the ion deposition technique. Then two surfaces of the encapsulated particle layer are polished until the fine particles are sufficiently exposed for the observation from both sides, and a micron-scaled thin film is obtained. Finally, the micron-scaled thin film is further reduced to a nanoscaled film penetrated by electron beams using ion beam thinner.

The microstructure of the samples was observed by scanning electron microscopy (Philips-XL30) at 25.0 kV and 30 μA and transmission electron microscopy (JEOL JEM-2100). The X-ray diffraction (XRD) analysis was performed on a Philips-DMAX-2500 with Cu K α radiation. The specific surface area, pore volume, and average pore diameter of sepiolite are determined by the instrument of ASAP 2020.

3. Results and Discussion

3.1. Microstructure of Sepiolite Minerals. Figure 2 shows the TEM of the sepiolite samples. From Figure 2(a), it can be seen that sepiolite samples with diameter of 60–100 nm are fibrous minerals materials. From Figure 2(b), it can be seen that the prismatic sizes of sepiolite samples with the form of uneven surface multiprism vary from 10 to 40 nm, and each surface of arris has enormous denticular microconvex without apparently regular distribution. From Figure 2(c), it can be seen that the prominent distance of microconvex mentioned previously with width of 2–5 nm and height of 1–2 nm is different, thus leading to many grooves with the tendency of spiral arrangement and distinct dislocation transform.

3.2. Specific Surface Area and Pore Character of Sepiolite Samples. The specific surface area of sepiolite samples is 160.77 m²/g with the *t*-Plot micropore area of 65.39 m²/g and *t*-Plot external surface area of 95.38 m²/g. The adsorptive cumulative volume is 0.189 cm³/g within the range from 1.70 to 300.0 nm, and the average pore diameter is 4.18445 nm. The pore diameter distribution curves and isotherm linear pot are shown in Figures 3 and 4. From Figure 3, it can be seen that the N₂ adsorption isotherm of sepiolite samples appearc hysteresis to a certain degree at 77 K. From Figure 4, it can be seen that sepiolite fibers exist more mesopores with large pore volume. When $P/P_0 = 0\text{--}0.5$, they have larger adsorptive capacity, indicating that sepiolite

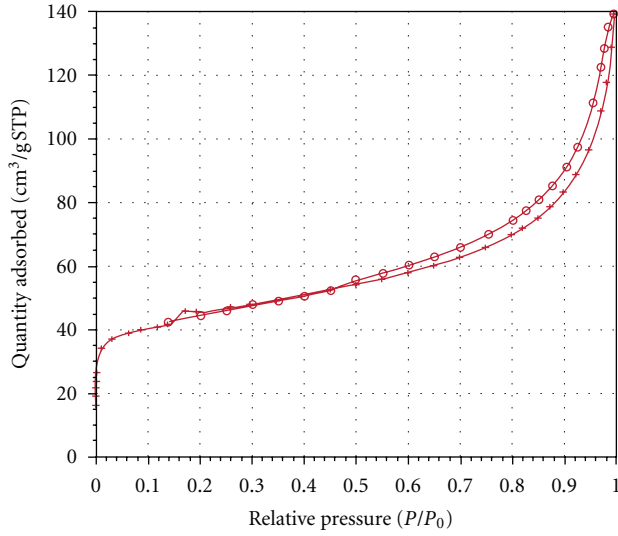


FIGURE 3: Absorption and desorption isotherm of sepiolite (“+” means absorption; “○” means desorption).

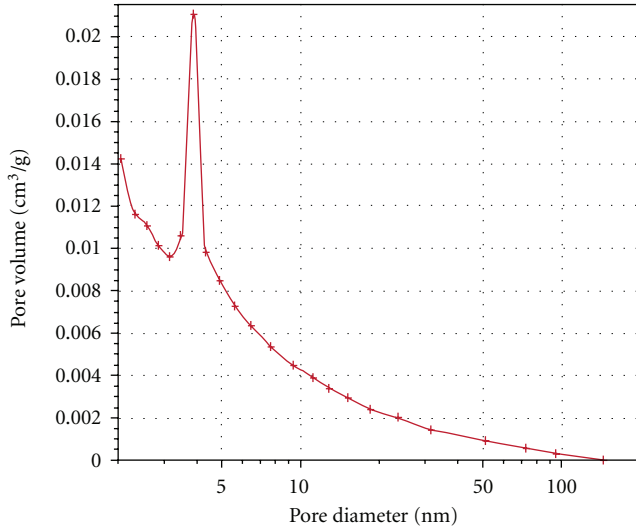


FIGURE 4: Pore diameter and pore volume distribution curve of sepiolite.

fibers contain considerable structural micropores with pore diameter <1.7 nm. The reason for the previously mentioned phenomenon is that adsorptive capacity increases along with the decrease of pore diameter, which proves the literature mentioned indirectly due to the limitation of BET method [1, 2]. As shown in Figure 4, the pore diameter of sepiolite is mainly between 1.7~5 nm, which proves that the adsorptive from is mainly mesopores adsorption. When $P/P_0 = 0.8 \sim 1$, the adsorption increases significantly, indicating the existence of micropores with diameter of 10~100 nm. The results show that pore volume of sepiolite fibers with diameter of 3.7~4.1 nm is 11.2%, and total area of sepiolite fibers with diameter of <4.9 nm is 59.2%, indicating that sepiolite fibers have part of larger channels.

3.3. Microstructure of the Section of Sepiolite Minerals. Figure 5 shows the section of sepiolite minerals. From Figure 5, it can be seen that part of dark area represents copper, and bright gray area represents the cross- and longitudinal-section of sepiolite fibers. Figure 5(b) is the partial enlarged detail of broken curve of Figure 5(a), which is likely to be a single fiber with diameter of 130 nm or multiple-strand fiber with diameter of 30~50 nm bundles. Many dark gray spots with diameter of 2~4 nm distribute regularly in the circle, which may be caused by the permeance of copper powders during the embedding. From Figure 5(a), it can be seen that gray area represents cross- and longitudinal-section of sepiolite fibers with irregular oval; the diameter of which is about 30~150 nm. Due to the natural bend and difference of section degree of fibers, light area forms irregular alteration. Figure 5(d) is the partial enlarged detail of broken curve of Figure 5(c). From Figure 5(d), it can be seen the area pointed by arrow shows discontinuous states, indicating that fiber has at least more than four level alterations. Especially the oval area pointed by arrow four indicates that sepiolite fibers contain layer structure. The light and shade alteration of sepiolite section in the broken curve oval area in Figure 5(d) indicates the existence of considerable channels perpendicular to the inner surface of the fibers.

3.4. Microstructure Certification Inner Sepiolite Fibers. Figure 6 shows the longitudinal-section of a single fiber with diameter of 250 nm or two strings fibres. From the bright and dark difference in continuous line rectangle, it can be seen that many parallel arrangement and even breadth grooves or swells exist parallel to the c -axis. The width of grooves is about 2~5 nm, and the smaller microswells (pointed by arrow) exists in larger grooves. The ribs of swells have many breakpoints, leading to the formation of channel. The ribs among breakpoint vary from 5 to 80 nm; many of which are

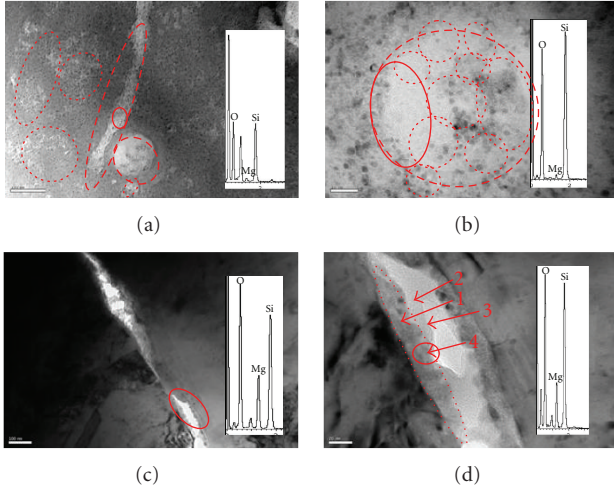


FIGURE 5: Microstructure of sepiolite section under HRTEM (a) cross and longitudinal section of sepiolite fibers; (b) cross section of sepiolite fiber bundles; (c) longitudinal section of sepiolite fibers; (d) partial enlarged detail of (c).

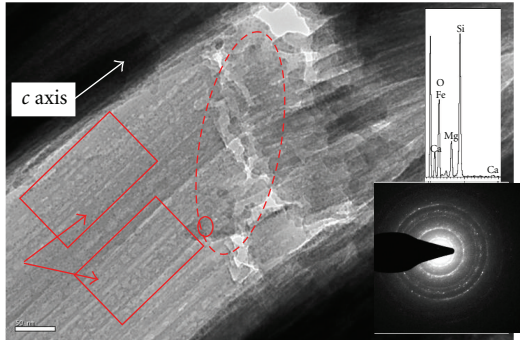


FIGURE 6: Diffraction spots and microstructure of sepiolite fibers.

10–25 nm. The diameter of channels parallel to the *c*-axis formed by breakpoints is mostly 3–5 nm (<10 nm), and the ribs of bigger grooves or swells form many channels with the diameter of 2–4 nm (dark spots). The broken curve oval is the region of fiber breakdown, which shows many sub circular structural micropores with the diameter of 2–5 nm (<10 nm). The diameters of micropores parallel to the *c*-axis are different significantly and are distributed irregularly, which in accordance with the results obtained by BET method. From diffraction spots in Figure 6, it can be seen that the diffraction spots are scattered and form obviously diffraction rings. The diffraction rings become wider caused by the irregularly distributed spots at the edge of inner diffraction rings, indicating the relative lower level of sepiolite minerals crystallization. And many breakpoints exist in diffraction rings, according to Bragg equation $2d \sin \theta = n\lambda$, only if wavelength of X-ray is *n* times as long as optical path difference between two crystal planes, diffraction appears. The existence of defect structure such as radial pores results in the discontinuation of crystal planes layered structure.

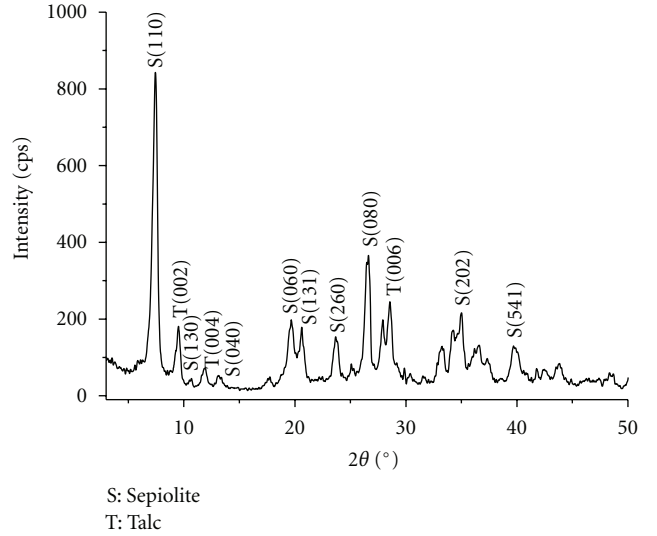


FIGURE 7: XRD patterns of sepiolite minerals fibers.

3.5. X-Ray Diffraction Analysis of Sepiolite Fiber. In sepiolite diffraction spectrum, near $2\theta = 7.42^\circ$, a strong diffraction peak appears (as shown in Figure 7), which is characteristic of layered two-dimensional lattice structure minerals, proving that sepiolite is a kind of layered fibrous structure mineral similar to concentric circles. According to Brauner's model and its theoretical crystal planes spacing should be about 1.26 nm, almost similar to the value tested by XRD (121 nm). The intensity of the diffraction peak of sepiolite crystal planes [110] is twice as high as other crystal planes, indicating that crystallization degree of sepiolite crystal planes [110] is significantly higher than that of other crystal planes, which becomes the foundation of sepiolite mineral crystal. Other crystals have many defects due to low crystallization degree, leading to uneven surfaces of fibers.

3.6. Reasons for Fibrous Structure, Uneven Surface, and Formation of Channels of Sepiolite. The interlayer spacing of sepiolite crystal planes is about 1.24 nm; in it there exist a lot of pore channels in different sizes perpendicular to the *c*-axis, and its pore channel area is about 10–16 nm² with 75 nm² as the largest [3], which is in accordance with results of the observation basically. In sepiolite mineral, silica tetrahedron net surfaces form layered crystal with half of magnesium oxygen octahedron through regular reversal, producing many longitudinal channels parallel to the *c*-axis, as shown in Figure 8.

From the view of Brauner's model, the lower density areas of atom appear in the reverse parts of silica tetrahedron nets surface, which is perhaps the key to forming a lot of channels perpendicular to the fiber axis. Although BET method is unlikely to detect related information of micropores with diameter smaller than 1.7 nm quantitatively, the observation in TEM can see a certain number of subprime structural micropores with the diameter less than 2.0 nm in structure layer. The XRD analysis shows that the interplanar distance of sepiolite mineral is only 1.2 nm and the width

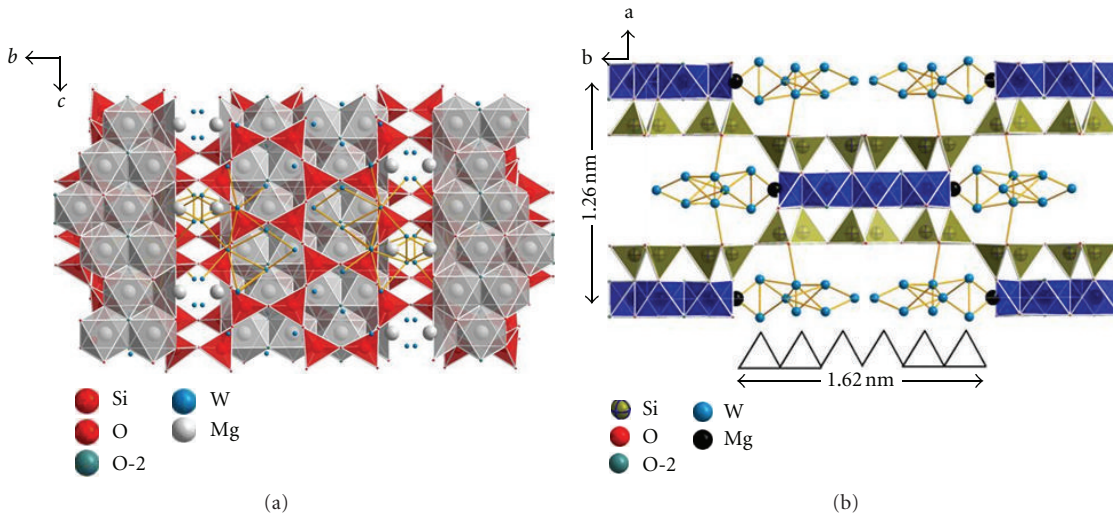


FIGURE 8: Diagram of crystal structure of sepiolite ((a) along *a*-axis direction; (b) along *c*-axis direction).

of the channel is only 0.63 nm after decreasing the space occupied by silica tetrahedron net surfaces and magnesium oxygen octahedron core layer. The length of the channel is 0.63×1.60 nm in condition of containing eight zeolite water, which cannot be measured quantitatively by BET method [13–15].

4. Conclusions

TEM observation of sepiolite fiber and section sample shows that sepiolite crystal not only contains a lot of structural micropores parallel to the fiber axis, but it also contains a large amount of short-range radial micropores perpendicular to the fiber axis. Radial micropores connect the micropores parallel to the fiber axis to each other, forming the three-dimensional internally connected channel network structure. The diameter of the micropores is mainly from 2 to 5 nm, in well accordance with the results of nitrogen adsorption BET analysis. TEM observation and XRD analysis prove that sepiolite crystal contains structural micropores parallel to the *c*-axis, but the real size and volume of these micropores cannot be detected quantitatively so far, and the formation mechanism of many microporous channels perpendicular to the *c*-axis in crystal needs further discussion.

Acknowledgments

This research was financially supported by the Application Foundation and Advanced Technology Research Program of Tianjin city (Grant no. 12JCQNJC02100), Application Foundation and Advanced Technology Research Program of Tianjin city (Grant no. 10JCZDJC22300), and Natural Science Foundation of Hebei province (Grant no. E2009000069).

References

- [1] B. S. Nagy and W. F. Bradley, "The structural scheme of sepiolite," *America Mineralogist*, vol. 40, pp. 885–892, 1955.
- [2] K. Brauner and A. Preisinger, "Struktur und entstehung des sepioliths," *Tschermaks Mineralogische und Petrographische Mitteilungen*, vol. 6, no. 1-2, pp. 120–140, 1956.
- [3] M. P. S. Krekeler and S. Guggenheim, "Defects in microstructure in palygorskite-sepiolite minerals: a transmission electron microscopy (TEM) study," *Applied Clay Science*, vol. 39, no. 1-2, pp. 98–105, 2008.
- [4] A. Miura, K. Nakazawa, T. Takei et al., "Acid-, base-, and heat-induced degradation behavior of Chinese sepiolite," *Ceramics International*, vol. 38, pp. 4677–4684, 2012.
- [5] S. Tunç, O. Duman, and A. Çetinkaya, "Electrokinetic and rheological properties of sepiolite suspensions in the presence of hexadecyltrimethylammonium bromide," *Colloids and Surfaces A*, vol. 377, no. 1–3, pp. 123–129, 2011.
- [6] H. X. Chen, H. Z. Lu, Y. Zhou, M. S. Zheng, C. M. Ke, and D. L. Zeng, "Study on thermal properties of polyurethane nanocomposites based on organo-sepiolite," *Polymer Degradation and Stability*, vol. 97, pp. 242–247, 2012.
- [7] E. İşçi and S. I. Turutoğlu, "Stabilization of the mixture of bentonite and sepiolite as a water based drilling fluid," *Journal of Petroleum Science and Engineering*, vol. 76, no. 1-2, pp. 1–5, 2011.
- [8] N. Volle, F. Giulieri, A. Burr, S. Pagnotta, and A. M. Chaze, "Controlled interactions between silanol groups at the surface of sepiolite and an acrylate matrix: consequences on the thermal and mechanical properties," *Materials Chemistry and Physics*, vol. 134, pp. 417–424, 2012.
- [9] A. S. Ozcan and O. Gok, "Structural characterization of dodecyltrimethylammonium (DTMA) bromide modified sepiolite and its adsorption isotherm studies," *Journal of Molecular Structure*, vol. 1007, pp. 36–44, 2012.
- [10] M. Suarez and E. Garcia-Romero, "Variability of the surface properties of sepiolite," *Applied Clay Science*, vol. 67–68, pp. 72–82, 2012.
- [11] Q. W. Zhu, Y. H. Zhang, F. Z. Lv, P. K. Chu, Z. F. Ye, and F. S. Zhou, "Cuprous oxide created on sepiolite: preparation, characterization, and photocatalytic activity in treatment of red water from 2,4,6-trinitrotoluene manufacturing," *Journal of Hazardous Materials*, vol. 217–218, pp. 11–18, 2012.
- [12] K. M. Fang, L. Zheng, K. Fang, and L. Huang, "Revealing microstructure of fine particles by TEM," *China Particuology*, vol. 1, pp. 88–90, 2003.

- [13] S. Inagaki, Y. Fukushima, H. Doi, and O. Kamigaito, "Pore size distribution and adsorption selectivity of sepiolite," *Clay Minerals*, vol. 25, no. 1, pp. 99–105, 1990.
- [14] A. A. Goktas, Z. Misirli, and T. Baykara, "Sintering behaviour of sepiolite," *Ceramics International*, vol. 23, no. 4, pp. 305–311, 1997.
- [15] H. Toshiyuki, T. Atsumu, Y. Atsushi, and O. Ryohei, "Model calculation of sepiolite surface areas," *Clays and Clay Minerals*, vol. 43, pp. 391–396, 1995.

Research Article

An Investigation of Electronic Structure and Aromaticity in Medium-Sized Nanoclusters of Gold-Doped Germanium

Xiao-Jun Li,^{1,2} Hong-Jiang Ren,² and Li-Ming Yang³

¹School of Natural and Applied Sciences, Northwestern Polytechnical University, Shaanxi, Xi'an 710072, China

²School of Chemistry and Chemical Engineering, Xi'an University of Arts and Science, Shaanxi, Xi'an 710072, China

³Center for Theoretical and Computational Chemistry (CTCC), Department of Chemistry, University of Oslo (UiO), P.O. Box 1033, Blindern, 0315 Oslo, Norway

Correspondence should be addressed to Xiao-Jun Li, lixiaojun0@yahoo.com.cn and Li-Ming Yang, lmyang.uit@gmail.com

Received 19 October 2012; Accepted 3 November 2012

Academic Editor: Su Chen

Copyright © 2012 Xiao-Jun Li et al. This is an open access article distributed under the Creative Commons Attribution License, which permits unrestricted use, distribution, and reproduction in any medium, provided the original work is properly cited.

The electronic property and aromaticity of endohedrally doped AuGe_{10}^- and AuGe_{12}^- clusters are investigated using the density-functional theory (DFT) within the hybrid B3LYP method. The calculated results reveal that the two clusters have high thermodynamic stability reflected by reaction energy. At the same time, it could be hoped that their high stability may arise from the closed-shell spherical aromaticity with eight π -electrons satisfying the $2(N_n + 1)^2$ counting rule with $N_\pi = 1$. A popular nucleus-independent chemical shifts (NICSs) calculation on basis of magnetic shieldings is also performed to confirm the aromaticity of the three-dimensional nanoclusters with largely negative NICS values. In addition, the electronic features and chemical bonding of the two clusters are analyzed with the help of the density of states (DOS) and electron localization function (ELF), and the majority of Ge–Ge bonds on the cage show more covalent characters.

1. Introduction

Semiconductor clusters, especially germanium, have been extensively investigated both experimentally and theoretically due to their potential applications in the microelectronics industry [1–6] and are of considerable scientific interest to explore the chemical structure and bonding as well as their thermodynamic stability and photoelectric effect. Unlike silicon, the effective masses of electron and hole in germanium are light; it can generate high carrier mobility and makes germanium attractive for high-performance field-effect logic transistors [7]. However, pure germanium clusters with medium or large size are chemically unstable and quite reactive because of the existence of abundant dangling bonds [5]. Interestingly, the encapsulation of different transition-metal (TM) atoms [8–10] in the medium-sized clusters can saturate the dangling bonds on the germanium cage surface and form sp^3 hybridization, and thereafter stabilize the germanium cages. Consequently, the metal-encapsulated germanium clusters exhibit many fascinating features such as nanostructures, for example, thermodynamic stability [11,

12], magnetic and superconducting behaviors [8, 13, 14], photoelectric effect [15, 16], and reduced energy gap between the highest occupied molecular orbital (HOMO) and the lowest unoccupied molecular orbital (LUMO) [9, 17, 18]. Some metal-encapsulated Ge clusters were also proposed as novel cluster-assembled materials due to the small HOMO-LUMO gap within about 2 eV, for example, AuGe_n ($n = 2$ –13) [18] and TM@Ge_{12} (TM = Zn, W, and Os) [19, 20]. In an experimental study, the bimetallic CoGe_{10}^- cluster in the mass spectrum was measured using laser vaporization technique [21], and its molecular structure was determined by the density-functional theory (DFT) calculations [22].

To our knowledge, there have been a number of interesting findings on the calculation of metal-encapsulated Ge clusters, for example, NiGe_n ($n = 1$ –13) [23], CrGe_n ($n = 1$ –13) [24], WGe_n ($n = 1$ –17) [25], TMGe_n (TM = Ti, Zr, Hf and Cu; $n = 1$ –20) [26, 27], and so on. A few outstanding predictions are medium-sized fullerene-like with 10 or 12 atoms. Kumar et al. [19, 28] reported a series of systematic investigations of TM@X_n ($X = \text{Si, Ge, Sn, and Pb}$; TM = Ni, Pd, Pt, Zn, and Cd; $n = 10$ and 12)

clusters using an ab initio ultrasoft pseudopotential method and generalized gradient approximation, and these clusters can be further stabilized by doping of an Ni or Pt atom, leading to some of the smallest metal-encapsulated clusters. King and coworkers [29, 30] explored the possible structures of M@Ge₁₀^z systems (M = Co and Be; z = -5 to +2) at the DFT-B3LYP/6-31G(d) level of theory and found that a singlet D_{5h} pentagonal prismatic structure is the global minimum for the trianionic Co@Ge₁₀³⁻ cluster, which is in accordance with the experimental result. Tang et al. [31] investigated the structure, stability, and optical property of TM@Ge₁₂ (TM = Sc–Ni) using the relativistic all-electron density functional theory. It was found that all the TM@Ge₁₂ clusters are perhaps partial metallic, and the ground-state geometry of them is probably pseudoicosahedron. Furthermore, eight π -electron natures make closed-shell spherical systems aromatic according to the $2(N_\pi + 1)^2$ [$N_\pi = 1$] rule proposed by Hirsch et al. [32]. In 2005, Chen and coworkers [33] also reported the nucleus-independent chemical shifts (NICSs) approach as an aromaticity criterion based on magnetic properties, which have been applied to characterize the all-metal aromatic/antiaromatic clusters [34].

In this paper, we report an investigation of electronic structure and aromaticity of the AuGe₁₀⁻ and AuGe₁₂⁻ nanoclusters using the hybrid DFT-B3LYP functional in conjunction with LanL2DZ basis set. The choice of endohedral gold atom is due to the fact that the bimetallic gold clusters have some fascinating physical and chemical properties and were experimentally observed using photoelectron spectroscopy [16, 35–37].

2. Theoretical Methods

The molecular structure, electronic property, and spherical aromaticity of AuGe₁₀⁻ and AuGe₁₂⁻ clusters were carried out using the hybrid DFT-B3LYP functional [38, 39] implemented in the Gaussian 09 package [40]. The standard double- ξ LanL2DZ basis set [41–43], which provides effective core potentials (ECPs) to consider the relativistic effects of transition metal atoms, was utilized here. Our previous calculations [18] also confirmed the credibility of the theoretical level, and the deviations within 1–6% are acceptable. To search for the most stable structures, a great number of structural isomers were considered for each size, on basis of a global search published previously [18, 44], and the local minima of all the stationary point geometries were determined by vibrational frequency analysis. The density of states (DOS) of the most stable AuGe₁₀⁻ and AuGe₁₂⁻ clusters was constructed using GaussSum 2.2 program [45] with the full width at half maximum (FWHM) of 0.3 eV, and the molecular orbitals were plotted with the isodensity surfaces (0.02 e/a.u.³). In addition, the nucleus-independent chemical shifts (NICS) were calculated by gauge-independent atomic orbital (GIAO) method [46, 47] at the B3LYP/LanL2DZ level of theory. In order to obtain more accurate NICS values, the correlation-consistent cc-pVTZ basis set [48] was also used for Ge atom, whereas the energy-adjusted small-core (19 valence electrons) pseudopotentials (PPs) [49] were used

for Au atom, labeled as cc-pVTZ-PP, and the single-point GIAO calculations at the B3LYP/cc-pVTZ-PP level of theory were performed based on the B3LYP/LanL2DZ-optimized geometries.

3. Results and Discussion

3.1. Geometry and Stability. Using the computation scheme described above, we have extensively explored a number of initial isomers formed from taking the previously reported structures of different TMGe₁₀ systems, or doping one Au dopant at all possible positions of the lower-lying Ge₁₀ isomers, or replacing one Ge atom of the lower-lying Ge₁₁ isomers with an Au atom to form new isomers. As a result, the most stable AuGe₁₀⁻ cluster is found to be an endohedrally Au-doped pentagonal prism (see Figure 1(a)). It is worth mentioning that, when an electron is added to the lowest-energy neutral AuGe₁₀ cluster in C_{2v} symmetry [18], the high D_{5h} -symmetric anionic AuGe₁₀⁻ cluster with a 1A_1 electronic state forms due to the equal electron distribution for each Ge atom [44], indicating that the neutral AuGe₁₀ cluster is an electron-deficient base. The geometry of the lowest-energy AuGe₁₀⁻ cluster in D_{5h} symmetry is also consistent with the neutral FeGe₁₀ cluster [9] as well as the trianionic Co@Ge₁₀³⁻ cluster [29]. In the structure, there are 10 equivalent Ge–Ge bond lengths on two five-numbered germanium rings, and 5 equivalent Ge–Ge bond lengths on side-jointed prism. At the B3LYP/LanL2DZ level of theory, the equilibrium Ge–Ge bond lengths of them are predicted to be 2.722, and 2.858 Å, respectively; and the equilibrium Au–Ge bond lengths in the pentagonal prism are calculated to be 2.721 Å, as shown in Table 1.

Analogous to the formation of AuGe₁₀⁻ cluster, all the possible isomers of AuGe₁₂⁻ cluster are considered. An Au-doped bicapped pentagonal prism is optimized to be the lowest-energy AuGe₁₂⁻ structure, which displays a 1A_1 electronic state in D_{2d} symmetry (see Figure 1(b)). By comparison, the icosahedral structure of ZnGe₁₂ [50] cluster is confirmed to be the global minima in the potential energy surface (PES), but the icosahedral AuGe₁₂⁻ structure is only a local minimum which is higher in energy than the lowest-energy structure by 0.32 eV [44]. In the bicapped pentagonal prism, the D_{2d} structure has two C_2 axes and two σ_d planes. As a result, four different Ge–Ge bond lengths are predicted to be 2.611, 2.644, 2.647 and 2.855 Å, respectively, whereas the two equilibrium Au–Ge bond lengths are calculated to be 2.814 and 2.942 Å.

As discussed above, the endohedrally doped AuGe₁₀⁻ and AuGe₁₂⁻ clusters are the most stable. Obviously, they do not obey the 18-electron counting rule (also known as the octet rule) [51] which may give rise to the high stability of cluster. In 2003, Sen and Mitas [52] also reported the limitation of the 18-electron rule and found that the filling of electron shell according to 18-electron rule is not the only factor in determining the structural stability, and the stability should depend on structural geometry, choice of metal atom, neutral or charged species, and so forth. In addition, one needs to calculate reaction energy to explain

TABLE 1: Optimized bond distances (in Å), NICS values (in ppm) at different positions^a, and electron configurations of the lowest-energy AuGe_{10}^- (D_{5h}) and AuGe_{12}^- (D_{2d}) clusters.

Cluster	$d_{\text{Ge}-\text{Ge}}$	$d_{\text{Ge}-\text{Au}}$	0.0 Å	0.5 Å	NICS ^b	1.0 Å	1.5 Å	2.0 Å	3.0 Å	Electron configuration
AuGe_{10}^-	2.722	2.721	-259.6	-183.7	-50.7	-25.2	-14.1	-8.5		$(1\text{a}_1')^2(1\text{e}_1')^4(1\text{a}_2'')^2(2\text{a}_1'')^2$
	2.858		(-236.1)	(-177.4)	(-47.3)	(-24.4)	(-15.7)	(-10.6)		$(2\text{e}_1')^4(2\text{a}_2'')^2(1\text{e}_1'')^4(1\text{e}_2')^4$
AuGe_{12}^-	2.611	2.814	-296.4	-199.0	-61.3	-36.3	-25.8	-18.0		$(3\text{a}_1')^2(2\text{e}_1')^2(4\text{a}_1)^2(4\text{e})^4$
	2.644	2.942	(-277.1)	(-196.4)	(-60.8)	(-37.7)	(-28.0)	(-19.4)		$(1\text{a}_2)^2(2\text{b}_1)^2(4\text{b}_2)^2(5\text{e})^4$
	2.647									$(5\text{a})^2(5\text{b}_2)^2(6\text{a}_1)^2(6\text{e})^4$
	2.855									$(6\text{b}_2)^2(7\text{e})^4(3\text{b}_1)^2(7\text{a}_1)^2$
										$(8\text{e})^4(2\text{a}_2)^2$

^a NICS values were computed at the GIAO-B3LYP/Lanl2DZ//B3LYP/Lanl2DZ level, based on the positions located on the radial L_{ab} connecting the center site (see Figure 1).^b NICS values in parentheses were obtained from the GIAO-B3LYP/cc-pVTZ-PP/B3LYP/Lanl2DZ calculations.

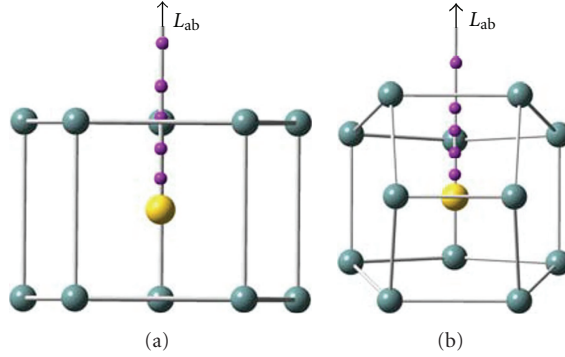


FIGURE 1: Equilibrium structures of the lowest-energy D_{5h} -symmetric AuGe_{10}^- (a) and D_{2d} -symmetric AuGe_{12}^- (b) clusters in [44]. The different NICS sites (purple balls) are indicated.

the thermodynamic stability of the cluster, and the reaction energy (E_r) can be computed according to the following equation:

$$E_r(\text{AuGe}_n^-) = \frac{[E(\text{AuGe}_n^-) - nE(\text{Ge}) - E(\text{Au}^-)]}{(n+1)}, \quad n = 10 \text{ or } 12, \quad (1)$$

where $E(\text{AuGe}_n^-)$, $E(\text{Ge})$, and $E(\text{Au}^-)$ represent the total energies of AuGe_n^- , Ge, and Au^- atoms, respectively. All the total energies include the correction of zero-point vibrational energy (ZPVE). According to our knowledge, the formations of AuGe_{10}^- and AuGe_{12}^- clusters are exothermic with the large negative E_r values, being -2.44 and -2.50 eV. Interestingly, their high thermodynamic stabilities are mainly associated with the geometry and the number of dangling bonds in the two clusters, as mentioned in previous study [18]. Our results also reveal that both of them can appear as stable species, and the two clusters could be synthesized through the exothermic reaction pathway.

3.2. Electronic Structure and Chemical Bonding. In order to explore the electronic features related to the stability of the clusters, we have performed a detailed analysis of the molecular orbitals by examining the partial density of states (PDOS) from the contribution of different orbital components (Au: s, p, d ; Ge: s, p) and the electron density of the HOMO and LUMO states. The plots of PDOS of the AuGe_{10}^- and AuGe_{12}^- clusters are shown in Figures 2(a) and 2(b), respectively.

As for a typical case, each Ge atom is expected to contribute its four valence electrons to the electron shell configuration of the molecular systems. The AuGe_{10}^- cluster with D_{5h} symmetry thus contains 42 valence electrons which are distributed in the following orbital configuration: $(1e_1'')^2 (1e_2')^4 (3a_1')^2 (2e_1'')^4 (2e_2')^4 (1e_2'')^4 (4a_1')^2 (5a_1')^2 (3e_2')^4 (3e_1')^4 (3a_2'')^2 (4e_1')^4 (2e_2'')^4$, as listed in Table 1. Due to the high D_{5h} symmetry, additionally, the molecular orbitals strongly resemble the spherical features. From the Figure 2(a), we clearly see that the electronic states at high-energy region of around -3.9 eV above come

mainly from p -Ge state; and the contribution from s -Ge state is very little. The difference is that the valence molecular orbitals at around -6.0 eV below mainly ascribe to the contribution of d -Au and s -Ge states; in particular, the E_2' -type valence orbital at -6.77 eV, holding a doubly degenerate state, is composed of d -Au state mixed with s -Ge state. Similar behavior is observed for the D_{2d} -symmetric AuGe_{12}^- cluster which contains 50 valence electrons with an orbital configuration of $[(3e)^4 (3a_1)^2 (3b_2)^2 (4a_1)^2 (4e)^4 (1a_2)^2 (2b_1)^2 (4b_2)^2 (5e)^4 (5a_1)^2 (5b_2)^2 (6a_1)^2 (6e)^4 (6b_2)^2 (7e)^4 (3b_1)^2 (7a_1)^2 (8e)^4 (2a_2)^2]$. The electron density (0.02 e/a.u. 3) of HOMO and LUMO states of the two clusters is represented in Figure 2. One can see that both the HOMO and LUMO states are mainly localized around germanium cage, while some electronic distributions around Au atom are also found in the LUMO. It is remarkable that the encapsulation of the Au dopant is responsible for the geometric rearrangement of pure germanium clusters and the reduction of the HOMO-LUMO gaps of pure Ge_{10} and Ge_{12} clusters. Especially for the AuGe_{12}^- cluster the HOMO and LUMO are nondegenerate and are slightly separated from the adjacent occupied and unoccupied orbitals, resulting in its quite small HOMO-LUMO gap of 1.63 eV. Thus, although the germanium is semiconductor element, the AuGe_{10}^- and AuGe_{12}^- clusters may be considered as novel cluster-assembled materials with partially metallic features [19, 44].

In 1994, Silvi and Savin [53] reported that the electron localization function (ELF) is currently used to describe the nature of bonding. According to their descriptions, the molecular space is divided into regions or basins of localized electron pairs or attractors. Typically, the existence of a high ELF isovalue (around 0.7 and above) in the bonding region between two atomic basins signifies a localized chemical bond in the region [44, 54]. For the D_{5h} -symmetric AuGe_{10}^- cluster, the ELF basins along Ge–Ge bond upon two five-number germanium rings merge at an isovalue of 0.71 (Figure 3(a)), revealing that these Ge–Ge bonds are covalent in nature, while the five Ge–Ge prismatic bonds have more metallic or less covalent character reflected by the slightly low ELF isovalue at 0.60 (Figure 3(b)). The ELF contour at a low isovalue of 0.32 (Figure 3(c)) shows two polarized basins

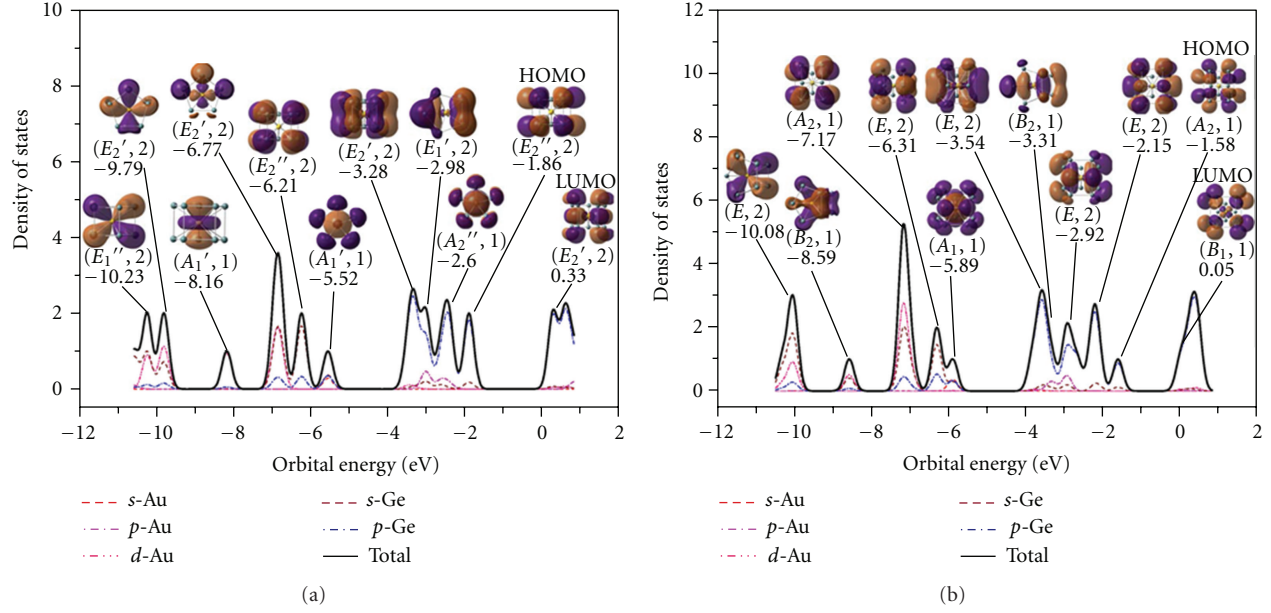


FIGURE 2: Density of states (DOS) of the lowest-energy AuGe_{10}^- (a) and AuGe_{12}^- (b) clusters computed at the B3LYP/LanL2DZ level of theory.

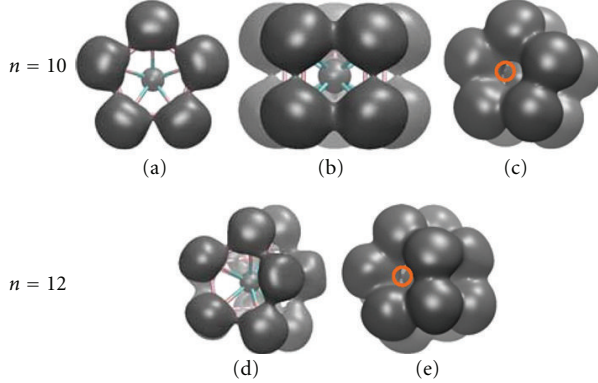


FIGURE 3: The ELF isosurfaces of the AuGe_{10}^- and AuGe_{12}^- clusters. Some different isovales are indicated: (a) 0.71, (b) 0.60, (c) 0.32, (d) 0.72, and (e) 0.29.

between Au and Ge atoms, so all the Au–Ge bonds are far from being covalent in nature but show an ionic character. The most stable AuGe_{12}^- cluster has a high (almost spherical) D_{2d} symmetry. The covalent bonding pattern between germanium atoms becomes more preferable because all atomic basins along the surface bonds in ELF contours almost merge at an isovalue of 0.72 (Figure 3(d)), whereas the Au–Ge bonds display a slightly increased ionic character confirmed by lower ELF isovalue (0.29, Figure 3(e)) and elongated Au–Ge bond lengths ($0.093\text{--}0.221\text{\AA}$), as discussed above.

3.3. The $2(N + 1)^2$ Rule. Aromaticity is well known as one of the important measures of compounds. Compared to

nonaromatic compounds, analogous aromatic compounds typically give enhanced chemical stability. In general, aromaticity of planar structure can be qualitatively explored using the $4N + 2$ Hückel rule [34]. Another electron counting rule, namely, $2(N + 1)^2$ rule proposed by Hirsch et al. [32], is proven as an effective aromaticity criterion for spherical species (I_h symmetry), as well as the extension of the treatment to inorganic cage molecules [55]. In the latter electron rule, the π -electron system of the species can be approximately considered as a spherical electron gas, which surrounds the surface of a sphere [56]. According to the Pauli principle, if the number of π electrons in a spherical structure satisfies the $2(N + 1)^2$ rule, the structure can show a spherical charge distribution and is therefore expected to be aromatic.

The molecular orbitals (MOs) of the AuGe_{10}^- and AuGe_{12}^- clusters are depicted in Figures 2(a) and 2(b), respectively. We see that the valence electron orbitals of them are divided into two different subsets occupied by σ or π electrons. In Figure 2(a), the D_{5h} -symmetric AuGe_{10}^- cluster contains eight valence π -electrons in four MOs, for example, $-5.52(A_1', 1)$, $-2.98(E_1', 2)$, and $-2.60(A_2'', 1)$, and these π -electrons satisfy the $2(N_\pi + 1)^2[N_\pi = 1]$ counting rule. Similarly, eight valence π -electrons are also found for the D_{2d} -symmetric AuGe_{12}^- cluster (Figure 2(b)) and occupy the $-5.89(A_1, 1)$, $-3.31(B_2, 1)$, and $-2.92(E, 2)$ orbitals. As a consequence, the two π -electron systems make the AuGe_{10}^- and AuGe_{12}^- clusters spherically aromatic. This aromatic feature can be regarded as one of the main reasons in the structural stabilization of endohedrally doped AuGe_{10}^- and AuGe_{12}^- clusters. However, it is noteworthy that the $2(N + 1)^2$ electron counting rule cannot be solely used to explain the aromaticity of compounds. For instance, the bianionic Si_{12}^{2-} cluster contains eight π electrons, but gives

an antiaromatic character [57]. Therefore, the aromaticity of both the AuGe_{10}^- and AuGe_{12}^- clusters needs to be further confirmed by NICS values given in next section.

3.4. NICS Values of Clusters. The aromaticity of a chemical compound can be usually discussed in terms of various criteria, but the criteria used to validate the aromaticity are sometimes controversial, likely Si_{12}^{2-} cluster. Herein, we performed a calculation of NICS proposed by Chen and coworkers [33], based on magnetic shieldings. Aromaticity is expected to be evaluated by a negative NICS value, and antiaromaticity by a positive NICS value. In general, a ghost atom is placed at the center of a spherical geometry to obtain NICS value. In order to get a reasonable value, however, we considered many different sites along central axis inside or outside the cage to test the variation of NICS value, as depicted in Figure 1. A radius (L_{ab}) from the center site of the cage to each ghost atom is also defined with $0 \leq L_{ab} \leq 3.0$.

Using the GIAO-B3LYP/LanL2DZ level of theory, we have calculated the NICS values of the AuGe_{10}^- and AuGe_{12}^- clusters. In order to give a proper description of magnetic and electronic properties, a large basis set (cc-pVTZ-PP) in our NICS calculations is also necessary with the same method. The NICS values of the two clusters are given in Table 1. We see that the NICS value at the center site is the largest one among all considered sites, being -259.6 and -296.4 ppm for AuGe_{10}^- and AuGe_{12}^- clusters, respectively. From Figure 4 we see that the NICS values of the AuGe_{10}^- cluster rapidly decreases to $L_{ab} = 1.5$ (-25.2 ppm) and then slowly decreases to $L_{ab} = 3.0$ (-8.5 ppm). Obviously, the NICS values close to the outer surface are relatively smaller than those inside the cage. Similar behavior is found for the AuGe_{12}^- cluster, and it gives a slightly larger NICS value than AuGe_{10}^- cluster. We also find that the NICS values with LanL2DZ basis set are in good agreement with the results with cc-pVTZ-PP basis set, except for the value at the center site that is relatively large with the deviation of about 20.0 ppm. Thus, the aromaticity of both the AuGe_{10}^- and AuGe_{12}^- clusters, characterized by the $2(N_\pi + 1)^2$ [$N_\pi = 1$] electron counting rule, is confirmed by largely negative NICS values. Moreover, the two clusters have very strong aromatic character at the center site, and the aromaticity will weaken outside the cage and vanish beyond.

4. Conclusions

Using the hybrid DFT-B3LYP functional, we have studied a large number of structural isomers for medium-sized AuGe_{10}^- and AuGe_{12}^- clusters. The endohedrally Au-doped pentagonal prism and bicapped pentagonal prism are found to be the most stable AuGe_{10}^- (D_{5h}) and AuGe_{12}^- (D_{2d}) structures, respectively. Analysis of reaction energy indicates that the endohedrally doped AuGe_{10}^- and AuGe_{12}^- clusters have the high thermodynamic stability. We see that the high-energy regions of molecular occupied orbitals of the two compounds come mainly from the contribution of p -Ge state by means of the partial density of states (PDOS). The electron localization functions (ELFs) are also considered

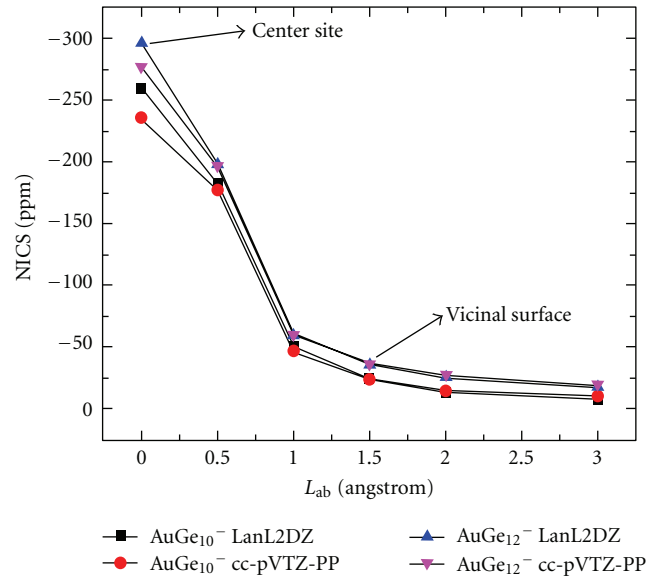


FIGURE 4: Comparison of NICS values of anionic AuGe_{10}^- , and AuGe_{12}^- clusters using two different LanL2DZ and cc-pVTZ-PP basis sets with the same B3LYP functional, based on the B3LYP/LanL2DZ geometries.

to explore the chemical bonding of the two clusters, and in some regions more metallic (or less covalent) character between germanium atoms becomes more preferable, for example, pentagonal prismatic bonds. In the AuGe_{10}^- and AuGe_{12}^- structures, eight valence π -electrons satisfy the $2(N_\pi + 1)^2$ [$N_\pi = 1$] counting rule and make the AuGe_{10}^- and AuGe_{12}^- clusters spherically aromatic. An NICS calculation on basis of magnetic shieldings is carried out to confirm the aromaticity of the three-dimensional clusters reflected by largely negative NICS values. Additionally, NICS is also relatively insensitive to the level of theory used in the study, for example, basis set.

References

- [1] G. R. Burton, C. Xu, C. C. Arnold, and D. M. Neumark, "Photoelectron spectroscopy and zero electron kinetic energy spectroscopy of germanium cluster anions," *The Journal of Chemical Physics*, vol. 104, no. 8, pp. 2757–2764, 1996.
- [2] M. Scheer, R. C. Bilodeau, C. A. Brodie, and H. K. Haugen, "Systematic study of the stable states of C^- , Si^- , Ge^- , and Sn^- via infrared laser spectroscopy," *Physical Review A*, vol. 58, no. 4, pp. 2844–2856, 1998.
- [3] Y. Negishi, H. Kawamata, T. Hayase et al., "Photoelectron spectroscopy of germanium-fluorine binary cluster anions: the HOMO-LUMO gap estimation of Ge_n clusters," *Chemical Physics Letters*, vol. 269, no. 3-4, pp. 199–207, 1997.
- [4] J. Thøgersen, L. D. Steele, M. Scheer, C. A. Brodie, and H. K. Haugen, "Electron affinities of Si, Ge, Sn and Pt by tunable laser photodetachment studies," *Journal of Physics B*, vol. 29, no. 7, pp. 1323–1330, 1996.
- [5] L.-Z. Zhao, W.-C. Lu, W. Qin, Q. J. Zang, C. Z. Wang, and K. M. Ho, "Fragmentation behavior of Ge_n clusters ($2 < n < 33$)," *Chemical Physics Letters*, vol. 455, no. 4–6, pp. 225–231, 2008.

- [6] D. Bandyopadhyay and P. Sen, "Density functional investigation of structure and stability of Ge_n and Ge_nNi ($n = 1 - 20$) clusters: validity of the electron counting rule," *Journal of Physical Chemistry A*, vol. 114, no. 4, pp. 1835–1842, 2010.
- [7] B. Yu, X. H. Sun, G. A. Calebotta, G. R. Dholakia, and M. Meyyappan, "One-dimensional germanium nanowires for future electronics," *Journal of Cluster Science*, vol. 17, no. 4, pp. 579–597, 2006.
- [8] W.-J. Zhao and Y.-X. Wang, "Geometries, stabilities, and magnetic properties of MnGe_n ($n = 2 - 16$) clusters: density-functional theory investigations," *Journal of Molecular Structure*, vol. 901, no. 1–3, pp. 18–23, 2009.
- [9] W.-J. Zhao and Y.-X. Wang, "Geometries, stabilities, and electronic properties of FeGe_n ($n = 9 - 16$) clusters: density-functional theory investigations," *Chemical Physics*, vol. 352, no. 1–3, pp. 291–296, 2008.
- [10] V. Kumar and Y. Kawazoe, "Metal-encapsulated caged clusters of germanium with large gaps and different growth behavior than silicon," *Physical Review Letters*, vol. 88, no. 23, Article ID 235504, 4 pages, 2002.
- [11] T. Van Hoof and M. Hou, "Structural and thermodynamic properties of Ag-Co nanoclusters," *Physical Review B*, vol. 72, no. 11, Article ID 115434, 12 pages, 2005.
- [12] E. E. Zhurkin and M. Hou, "Structural and thermodynamic properties of elemental and bimetallic nanoclusters: an atomic scale study," *Journal of Physics*, vol. 12, no. 30, pp. 6735–6754, 2000.
- [13] J. U. Reveles, P. Sen, K. Pradhan, D. R. Roy, and S. N. Khanna, "Effect of electronic and geometric shell closures on the stability of neutral and anionic TiNaN_n ($n = 1 - 13$) clusters," *Journal of Physical Chemistry C*, vol. 114, no. 24, pp. 10739–10744, 2010.
- [14] K. Meier, R. Cardoso-Gil, W. Schnelle, H. Rosner, U. Burkhardt, and U. Schwarz, "Thermal, magnetic, electronic, and superconducting properties of rare earth metal pentagermanides REGe_5 ($\text{RE} = \text{La}, \text{Nd}, \text{Sm}, \text{Gd}$) and synthesis of TbGe_5 ," *Zeitschrift für Anorganische und Allgemeine Chemie*, vol. 636, no. 8, pp. 1466–1473, 2010.
- [15] S. Furuse, K. Koyasu, J. Atobe et al., "Experimental and theoretical characterization of MSi_{16}^- , MGe_{16}^- , MSn_{16}^- and MPb_{16}^- ($M = \text{Ti}, \text{Zr}$, and Hf): the role of cage aromaticity," *The Journal of Chemical Physics*, vol. 129, no. 6, pp. 064311–064316, 2008.
- [16] X. Li and L.-S. Wang, "Experimental search and characterization of icosahedral clusters: Al_{12}X^- ($X = \text{C}, \text{Ge}, \text{Sn}, \text{Pb}$)," *Physical Review B*, vol. 65, no. 15, Article ID 153404, 4 pages, 2002.
- [17] J. Wang and J.-G. Han, "A computational investigation of copper-doped germanium and germanium clusters by the density-functional theory," *The Journal of Chemical Physics*, vol. 123, no. 24, Article ID 244303, 12 pages, 2005.
- [18] X.-J. Li and K.-H. Su, "Structure, stability and electronic property of the gold-doped germanium clusters: AuGe_n ($n = 2 - 13$)," *Theoretical Chemistry Accounts*, vol. 124, no. 5–6, pp. 345–354, 2009.
- [19] V. Kumar and Y. Kawazoe, "Metal-encapsulated icosahedral superatoms of germanium and tin with large gaps: ZnGe_{12} and CdSn_{12} ," *Applied Physics Letters*, vol. 80, no. 5, pp. 859–861, 2002.
- [20] J. Lu and S. Nagase, "Metal-doped germanium clusters MGe_n 's at the sizes of $n = 12$ and 10: divergence of growth patterns from the MSi_n clusters," *Chemical Physics Letters*, vol. 372, no. 3–4, pp. 394–398, 2003.
- [21] X. Zhang, G. Li, and Z. Gao, "Laser ablation of Co/Ge mixtures: a new type of endohedral structure, a semiconductor cage trapping a metal atom," *Rapid Communications in Mass Spectrometry*, vol. 15, no. 17, pp. 1573–1576, 2001.
- [22] Q. Jing, F.-Y. Tian, and Y.-X. Wang, "No quenching of magnetic moment for the Ge_nCo ($n = 1 - 13$) clusters: first-principles calculations," *The Journal of Chemical Physics*, vol. 128, no. 12, Article ID 124319, 5 pages, 2008.
- [23] J. Wang and J.-G. Han, "A theoretical study on growth patterns of Ni-doped germanium clusters," *Journal of Physical Chemistry B*, vol. 110, no. 15, pp. 7820–7827, 2006.
- [24] N. Kapila, I. Garg, V. K. Jindal et al., "First principle investigation into structural growth and magnetic properties in Ge_nCr clusters for $n = 1 - 13$," *Journal of Magnetism and Magnetic Materials*, vol. 324, no. 18, pp. 2885–2893, 2012.
- [25] J. Wang and J.-G. Han, "Geometries and electronic properties of the tungsten-doped germanium clusters: WGe_n ($n = 1 - 17$)," *Journal of Physical Chemistry A*, vol. 110, no. 46, pp. 12670–12677, 2006.
- [26] M. Kumar, N. Bhattacharyya, and D. Bandyopadhyay, "Architecture, electronic structure and stability of TM@Ge_n ($\text{TM} = \text{Ti}, \text{Zr}$ and Hf , $n = 1 - 20$) clusters: a density functional modeling," *Journal of Molecular Modeling*, vol. 18, no. 1, pp. 405–418, 2012.
- [27] D. Bandyopadhyay, "Architectures, electronic structures, and stabilities of Cu-doped Ge_n clusters: density functional modeling," *Journal of Molecular Modeling*, vol. 18, no. 8, pp. 3887–3902, 2012.
- [28] V. Kumar, A. K. Singh, and Y. Kawazoe, "Smallest magic caged clusters of Si, Ge, Sn, and Pb by encapsulation of transition metal atom," *Nano Letters*, vol. 4, no. 4, pp. 677–681, 2004.
- [29] M. M. Uță, D. Cioboc, and R. B. King, "Cobalt-centered ten-vertex germanium clusters: the pentagonal prism as an alternative to polyhedra predicted by the Wade-Mingos rules," *Inorganic Chemistry*, vol. 51, no. 6, pp. 3498–3504, 2012.
- [30] R. B. King, I. Silaghi-Dumitrescu, and M. M. Uță, "Endohedral beryllium atoms in ten-vertex germanium clusters: effect of a small interstitial atom on the cluster geometry," *Journal of Physical Chemistry A*, vol. 115, no. 13, pp. 2847–2852, 2011.
- [31] C. Tang, M. Liu, W. Zhu et al., "Probing the geometric, optical, and magnetic properties of 3d transition-metal endohedral Ge_{12}M ($\text{M} = \text{Sc} - \text{Ni}$) clusters," *Computational and Theoretical Chemistry*, vol. 969, no. 1–3, pp. 56–60, 2011.
- [32] A. Hirsch, Z. Chen, and H. Jiao, "Spherical aromaticity in I_h symmetrical fullerenes: the $2(N + 1)^2$ rule," *Angewandte Chemie*, vol. 39, no. 21, pp. 3915–3917, 2000.
- [33] Z. Chen, C. S. Wannere, C. Corminboeuf, R. Puchta, and P. von Ragué Schleyer, "Nucleus-independent chemical shifts (NICS) as an aromaticity criterion," *Chemical Reviews*, vol. 105, no. 10, pp. 3842–3888, 2005.
- [34] A. I. Boldyrev and L.-S. Wang, "All-metal aromaticity and antiaromaticity," *Chemical Reviews*, vol. 105, no. 10, pp. 3716–3757, 2005.
- [35] L.-M. Wang, S. Bulusu, W. Huang, R. Pal, L. S. Wang, and C. Z. Xiao, "Doping the golden cage Au_{16}^- with Si, Ge, and Sn," *Journal of the American Chemical Society*, vol. 129, no. 49, pp. 15136–15137, 2007.
- [36] R. Pal, L.-M. Wang, W. Huang, L. S. Wang, and X. C. Zeng, "Structural evolution of doped gold clusters: MAu_x^- ($\text{M} = \text{Si}, \text{Ge}, \text{Sn}; x = 5 - 8$)," *Journal of the American Chemical Society*, vol. 131, no. 9, pp. 3396–3404, 2009.
- [37] M. Akutsu, K. Koyasu, J. Atobe, K. Miyajima, M. Mitsui, and A. Nakajima, "Electronic properties of Si and Ge atoms doped

- in clusters: In_nSi_m and In_nGe_m ,” *Journal of Physical Chemistry A*, vol. 111, no. 4, pp. 573–577, 2007.
- [38] C. Lee, W. Yang, and R. G. Parr, “Development of the Colle-Salvetti correlation-energy formula into a functional of the electron density,” *Physical Review B*, vol. 37, no. 2, pp. 785–789, 1988.
- [39] A. D. Becke, “Density-functional exchange-energy approximation with correct asymptotic behavior,” *Physical Review A*, vol. 38, no. 6, pp. 3098–3100, 1988.
- [40] M. J. Frisch, G. W. Trucks, H. B. Schlegel et al., Gaussian 09, Revision A. 02, Gaussian, Inc., Wallingford, UK, 2009.
- [41] P. J. Hay and W. R. Wadt, “Ab initio effective core potentials for molecular calculations. Potentials for the transition metal atoms Sc to Hg,” *The Journal of Chemical Physics*, vol. 82, no. 1, pp. 270–283, 1985.
- [42] W. R. Wadt and P. J. Hay, “Ab initio effective core potentials for molecular calculations. Potentials for main group elements Na to Bi,” *The Journal of Chemical Physics*, vol. 82, no. 1, pp. 284–298, 1985.
- [43] P. J. Hay and W. R. Wadt, “Ab initio effective core potentials for molecular calculations. Potentials for K to Au including the outermost core orbitale,” *The Journal of Chemical Physics*, vol. 82, no. 1, pp. 299–310, 1985.
- [44] X.-J. Li, K.-H. Su, X.-H. Yang et al., “Size-selective effects of geometry and electronic property on bimetallic Au-Ge nanoclusters,” to appear in. *Computational and Theoretical Chemistry*.
- [45] N. M. O’Boyle, A. L. Tenderholt, and K. M. Langner, “Cclib: a library for package-independent computational chemistry algorithms,” *Journal of Computational Chemistry*, vol. 29, no. 5, pp. 839–845, 2008.
- [46] F. London, “Théorie quantique des courants interatomiques dans les combinaisons aromatiques,” *Journal de Physique et Le Radium*, vol. 8, no. 10, pp. 397–409, 1937.
- [47] G. Schreckenbach and T. Ziegler, “Density functional calculations of NMR chemical shifts and ESR g-tensors,” *Theoretical Chemistry Accounts*, vol. 99, no. 2, pp. 71–82, 1998.
- [48] A. K. Wilson, D. E. Woon, K. A. Peterson, and T. H. Dunning, “Gaussian basis sets for use in correlated molecular calculations. IX. The atoms gallium through krypton,” *The Journal of Chemical Physics*, vol. 110, no. 16, pp. 7667–7676, 1999.
- [49] D. Figgen, G. Rauhut, M. Dolg, and H. Stoll, “Energy-consistent pseudopotentials for group 11 and 12 atoms: adjustment to multi-configuration Dirac-Hartree-Fock data,” *Chemical Physics*, vol. 311, no. 1-2, pp. 227–244, 2005.
- [50] J. Wang and J. G. Han, “The growth behaviors of the Zn-doped different sized germanium clusters: a density functional investigation,” *Chemical Physics*, vol. 342, no. 1–3, pp. 253–259, 2007.
- [51] J. E. Huheey, E. A. Keiter, and R. L. Keiter, *Inorganic Chemistry: Principles of Structure and Reactivity*, Harper Collins College, New York, NY, USA, 4th edition, 2000.
- [52] P. Sen and L. Mitas, “Electronic structure and ground states of transition metals encapsulated in a Si_{12} hexagonal prism cage,” *Physical Review B*, vol. 68, no. 15, Article ID 155404, 4 pages, 2003.
- [53] B. Silvi and A. Savin, “Classification of chemical bonds based on topological analysis of electron localization functions,” *Nature*, vol. 371, no. 6499, pp. 683–686, 1994.
- [54] K. Joshi, D. G. Kanhere, and S. A. Blundell, “Abnormally high melting temperature of the Sn_{10} cluster,” *Physical Review B*, vol. 66, no. 15, Article ID 155329, 5 pages, 2002.
- [55] A. Hirsch, Z. Chen, and H. Jiao, “Spherical aromaticity of inorganic cage molecules,” *Angewandte Chemie*, vol. 40, no. 15, pp. 2834–2838, 2001.
- [56] T. B. Tai and M. T. Nguyen, “Lithium atom can be doped at the center of a germanium cage: the stable icosahedral $\text{Ge}_{12}\text{Li}^-$ cluster and derivatives,” *Chemical Physics Letters*, vol. 492, no. 4–6, pp. 290–296, 2010.
- [57] R. B. King, T. Heine, C. Corminboeuf, and P. V. R. Schleyer, “Antiaromaticity in bare deltahedral silicon clusters satisfying Wade’s and Hirsch’s rules: an apparent correlation of antiaromaticity with high symmetry,” *Journal of the American Chemical Society*, vol. 126, no. 2, pp. 430–431, 2004.

Research Article

Effective Red Compensation of $\text{Sr}_2\text{SiO}_4 : \text{Dy}^{3+}$ Phosphor by Codoping Mn^{2+} Ions and Its Energy Transfer

Le Zhang, Zhou Lu, Pengde Han, Lixi Wang, and Qitu Zhang

College of Materials Science and Engineering, Nanjing University of Technology, Jiangsu, Nanjing 210009, China

Correspondence should be addressed to Qitu Zhang, njutzl@126.com

Received 15 August 2012; Accepted 28 September 2012

Academic Editor: Su Chen

Copyright © 2012 Le Zhang et al. This is an open access article distributed under the Creative Commons Attribution License, which permits unrestricted use, distribution, and reproduction in any medium, provided the original work is properly cited.

Mn^{2+} ions codoped $\text{Sr}_2\text{SiO}_4 : \text{Dy}^{3+}$ phosphors were prepared by the solid-state reaction method using NH_4Cl as the flux. Their phase compositions, photoluminescence properties, and the energy transfer process were systematically investigated. All Mn/Dy codoped powders were α' - Sr_2SiO_4 . The codoping concentration range of Mn^{2+} was ≤ 4.0 mol% to keep the structure undamaged. The broad red emission of Mn^{2+} centered at 647 nm in $\text{Sr}_2\text{SiO}_4 : \text{Mn, Dy}$ powders, which effectively compensated the red emission of $\text{Sr}_2\text{SiO}_4 : \text{Dy}^{3+}$ phosphor. The CIE chromaticity coordinates dramatically changed from (0.310, 0.340) to (0.332, 0.326) due to the red enhancement via the energy transfer from Dy^{3+} to Mn^{2+} . This energy transfer is realized by the exchange interaction. But the luminescence quenching of $\text{Sr}_2\text{SiO}_4 : \text{Dy, Mn}$ phosphor was mainly caused by the electric multipoles interaction. The concentration optimized ($\text{Sr}_{0.96}, \text{Mn}_{0.02}, \text{Dy}_{0.02}$) SiO_4 phosphor with high and almost pure white emission has great potential to act as a single-matrix white phosphor for white LEDs.

1. Introduction

White light emitting diodes have attracted more attention due to their potential applications in extensive fields, such as device indicators, backlight, automobile headlights, and general illumination [1–4]. Current white LEDs are composed of blue-emitting GaN chip and yellow-emitting YAG:Ce phosphor. However, YAG:Ce has a deficient red emission, leading the white LEDs to have a low color rendering index ($\text{CRI} < 80$) [5]. To enrich the red emission, the phosphor blend of YAG:Ce and a red emitting phosphor is generally applied [6, 7]. Another technology is the combination of tri-color phosphors with an UV-LED chip. The above phosphor mixtures give fluorescence reabsorption and nonuniformity of luminescence properties, resulting in a loss of luminous efficiency and time-dependent shift of the color point. Therefore, a single-phase phosphor with direct white light emission is desirable [8–11].

At present, the most of this kind phosphors have at least two luminescent centers, such as $\text{Eu}^{2+}/\text{Mn}^{2+}$ [3, 12, 13], $\text{Ce}^{3+}/\text{Eu}^{2+}$ [8], or Eu^{2+} (in different lattice sites) [9]. As the natural white light emission ions, Dy^{3+} ions have two dominant emission bands of blue (485 nm, ${}^4\text{F}_{9/2} \rightarrow {}^6\text{H}_{15/2}$) and

yellow (570 nm, ${}^4\text{F}_{9/2} \rightarrow {}^6\text{H}_{13/2}$) [14, 15]. Recently, Dy^{3+} doped alkaline earth orthosilicates ($\text{Sr}_2\text{SiO}_4 : \text{Dy}^{3+}$) powders have attracted much attention due to its excellent emission characteristic, single luminescent center, and high absorption efficiency in the UV region [16–18]. This phosphor can emit white light with CIE chromaticity coordinates (0.310, 0.340). However, there is still a gap comparing with the pure white light (0.330, 0.330) due to the weak red emission at ~ 665 nm. Predictably, the compensation of red light will effectively reduce this gap and enhance the CRI and then obtain warm white light.

As known, Mn^{2+} ions can effectively absorb UV light and then emit different colors from green to deep red depending on the surrounding crystal field strength [19]. Red or white phosphors were successfully obtained by adjusting the concentration ratios of $\text{Mn}^{2+}/\text{Dy}^{3+}$ or $\text{Eu}^{2+}/\text{Dy}^{3+}$ [20–22]. Therefore, there is reason to believe that the $3d^5$ configured Mn^{2+} ions may effectively compensate the red emission of $\text{Sr}_2\text{SiO}_4 : \text{Dy}^{3+}$ phosphor as a red-emitting center with suitable doping concentration.

In this paper, Dy^{3+} and Mn^{2+} ions codoped Sr_2SiO_4 powders were prepared by the solid-state reaction method using

5 wt% NH₄Cl as the flux. The phase compositions and luminescence properties of prepared powders were systematically investigated as well as the energy transfer process from Dy³⁺ to Mn²⁺. It was found that the broad emission band of Mn²⁺ centered at 650 nm was observed from Sr₂SiO₄:Mn²⁺, Dy³⁺ powders. The energy transfer from Dy³⁺ to Mn²⁺ dramatically changed the CIE chromaticity coordinates from (0.310, 0.340) to (0.332, 0.326). Sr₂SiO₄:Dy³⁺, Mn²⁺ with high and almost pure white emission has great potential to act as single-matrix white phosphor for white LEDs.

2. Materials and Experimental Details

All powder samples were synthesized by the solid-state reaction method. High purity Dy₂O₃ (>99.99%, the others are analytical grade), SrCO₃, SiO₂, MnCO₃, Li₂CO₃ (the charge compensation agent), and NH₄Cl (5 wt%, the flux) were used as the starting materials. Stoichiometrical amounts of starting materials were mixed with ethanol and then ball milled using planetary milling machine for 8 h. The synthesis was performed at 1000°C for 4 h under the reducing atmosphere (5% H₂ + 95% N₂). Series of (Sr_{0.99-x}, Mn_x)₂SiO₄:Dy_{0.02} powders and (Sr_{0.98-x}, Dy_x)₂SiO₄:Mn_{0.04} ($x = 0.0\text{--}8.0$, mol%) were prepared.

The crystalline phases of the synthesized powders were determined by the X-ray diffraction (XRD, D/Max2500, Rigaku, Japan) using Cu K α radiation ($\lambda = 1.5406 \text{ \AA}$) in the range of 5° ~ 80° with a step size of 0.02°. The photoluminescence spectra of the phosphors were measured using a fluorescent spectrophotometer (FL3-221, HORIBA, Jobin Yvon, France) with a 450 W xenon lamp as the excitation source (the multiplication voltage: 700 V; the slit width: 2.5 nm). All measurements were carried out at room temperature.

3. Results and Discussion

3.1. Phase Compositions of (Sr, Mn, Dy)₂SiO₄ Powders. Figure 1 shows the XRD patterns of 1 mol% Dy \cdot xMn ($x = 0.0\text{--}8.0$ mol%) doped Sr₂SiO₄ powders. The overlap between the diffraction peaks of α' -Sr₂SiO₄ (JCPDS no. 39-1256) and β -Sr₂SiO₄ (no. 38-0271) was too much to index them precisely, especially at about 30–32°. Therefore, only the diffraction peaks with clear ownership were indexed. Obviously, the phase compositions of Dy/Mn codoped powders were almost pure α' -Sr₂SiO₄ when $x \leq 4.0$ mol%. The ionic radii of Sr²⁺, Mn²⁺, and Dy³⁺ are 1.12, 0.80, and 0.91 Å, respectively. Therefore, the diffraction peaks of all samples slightly shifted to the higher angle with increasing the substitution concentration of Mn²⁺ (Figure 1 (right)). However, minor SrSiO₃ and MnO₂ were found when the Mn concentration was increased to 8.0 mol%. In general, the substitution of Mn²⁺ with smaller ionic radius cannot change the crystal structure of host. However, the difference of ionic radii between Sr²⁺ and Mn²⁺ is 40.0% ((1.12–0.80)/0.80, much bigger than 15%) and the electronegativity of Mn²⁺ (1.55) is much bigger than that of Sr²⁺ (0.95), which make the excess Mn exist in “MnO₂” form [23].

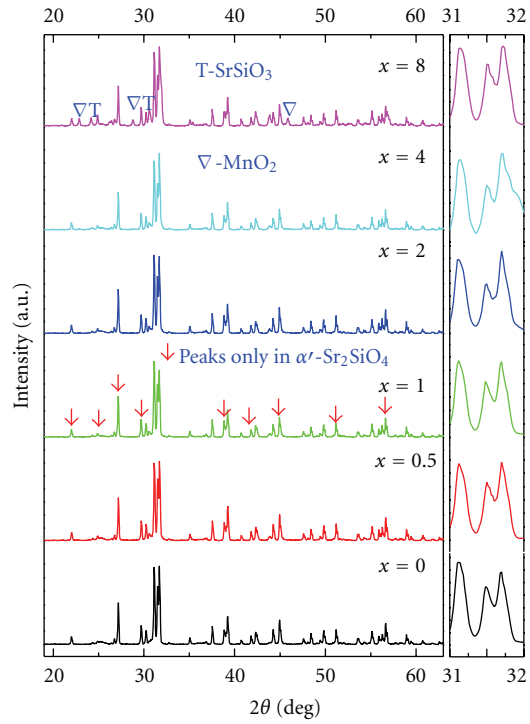


FIGURE 1: XRD patterns of (Sr_{0.99-x}, Mn_x)₂SiO₄:Dy_{0.02} (x , mol%) powders as a function of Mn²⁺ concentration.

When the Dy concentration was fixed at 1.0 mol%, the codoping concentration of Mn²⁺ for the maximum red emission was 2.0 mol% (see later part “3.2 Luminescence of (Sr, Mn, Dy)₂SiO₄ powders”). Thus, the samples (Sr_{0.98-x}, Dy_x)₂SiO₄:Mn_{0.04} ($x = 0.0\text{--}8.0$, mol%) as a function of Dy concentration were also synthesized to obtain the simultaneous maximum of the emission of Dy and Mn. Their XRD patterns are shown in Figure 2. All Mn/Dy codoped powders were also α' phase. All diffraction peaks slightly shifted to higher angle with increasing the substitution concentration of Dy³⁺. In fact, the phase compositions of all Mn/Dy codoped powders are consistent with the regularity suggested by our previous study [17]. Without any doping, the phase composition of host powders using 5.0 wt% NH₄Cl as the flux is almost pure β phase [16]. But the smaller ions (Dy³⁺/Mn²⁺) doped or codoped powders are α' -Sr₂SiO₄. The doping of smaller ions within certain concentration range is beneficial to the formation of α' phase. Here, the structure is still stable even though the codoping concentration of Dy³⁺ reaches 8.0 mol%. However, the codoping concentration range of Mn²⁺ to keep the structure undamaged is ≤ 4.0 mol% in our experiments due to the big difference of ionic radius between Mn²⁺ and Sr²⁺. Therefore, the codoped Mn²⁺ ions are considered to be effective to occupy the Sr²⁺ site in the range of 0.0~4.0 mol%.

3.2. Luminescence of (Sr, Mn, Dy)₂SiO₄ Powders. Figure 3(a) shows the excitation spectrum of Sr₂SiO₄:Dy³⁺ powders ($\lambda_{\text{em}} = 571 \text{ nm}$). The excitation peaks included 349, 364, 386, 452, and 466 nm corresponding to the transitions of

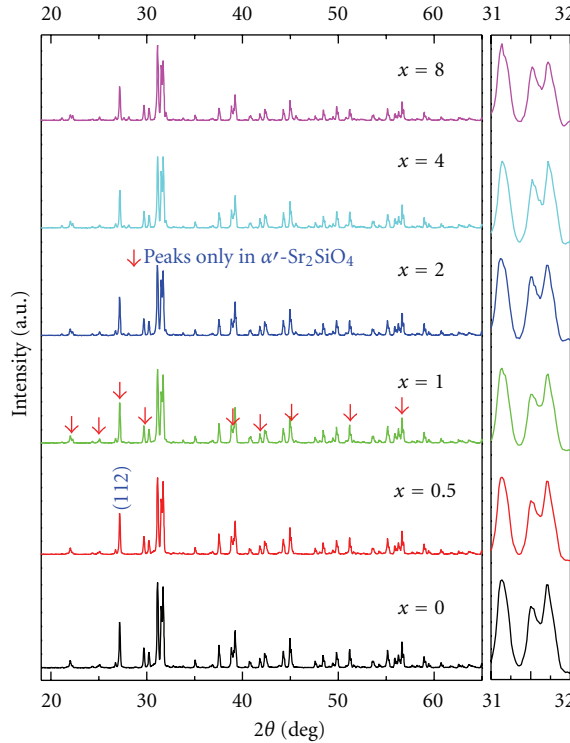


FIGURE 2: XRD patterns of $(\text{Sr}_{0.98-x}, \text{Dy}_x)_2\text{SiO}_4 : \text{Mn}_{0.04}$ (x , mol%) powders as a function of Dy^{3+} concentration.

$^6\text{H}_{15/2} \rightarrow ^4\text{D}_{7/2}$, $^6\text{P}_{7/2}$, $^4\text{F}_{21/2}$, $^4\text{I}_{15/2}$ and $^4\text{F}_{9/2}$, respectively. The strongest excitation peak was at 349 nm. Its corresponding emission spectrum (Figure 3(b)) exhibited the typical characteristics of Dy^{3+} ions, including two strong peaks centered at 477 nm and 571 nm and a weak emission at 665 nm. The integrated intensities of blue (477 nm) and yellow (571 nm) colors were almost equal. Figure 4(a) shows the excitation spectrum of $\text{Sr}_2\text{SiO}_4 : \text{Mn}^{2+}$ powders ($\lambda_{\text{em}} = 647$ nm). The main excitation peaks centered at 371, 416, and 543 nm, corresponding to the transitions from $^6\text{A}_1(^6\text{S})$ ground state of Mn^{2+} to its $^4\text{T}_2(^4\text{G}), ^4\text{E}(^4\text{G})$, and $^4\text{T}_1(^4\text{G})$ excited state, respectively. Under the excitation of 416 nm, a broad emission centered at 647 nm was observed (Figure 4(b)). This emission was caused by the transition of $^4\text{T}_1(^4\text{G})$ - $^6\text{A}_1(^6\text{S})$ and its Gauss fitting curves (dotted line) included two peaks at 645 nm and 719 nm, which maybe resulting from the two kinds of lattice environment of Sr^{2+} site (their coordination numbers were 9 and 10, resp.).

From Figure 5 (a, excitation spectrum of Mn^{2+}) and (b, emission spectrum of Dy^{3+}), it can be seen that the excitation of Mn^{2+} was overlapped by the emission of Dy^{3+} , which indicated that a potential energy transfer from Dy^{3+} to Mn^{2+} in Sr_2SiO_4 lattice might exist. Figure 5(c) shows the excitation spectrum of Dy/Mn codoped $(\text{Sr}_{0.97}\text{Mn}_{0.02})_2\text{SiO}_4 : \text{Dy}_{0.02}$ powders. The monitored wavelength was 647 nm for the emission of Mn^{2+} . However, the strong absorption of Dy^{3+} at 349 nm appeared which strongly indicated that the energy transfer of $\text{Dy}^{3+} \rightarrow \text{Mn}^{2+}$ happened. In addition, the characteristic emission of Mn^{2+} at ~ 650 nm was also clearly observed under the excitation of 349 nm (Figure 5(d)).

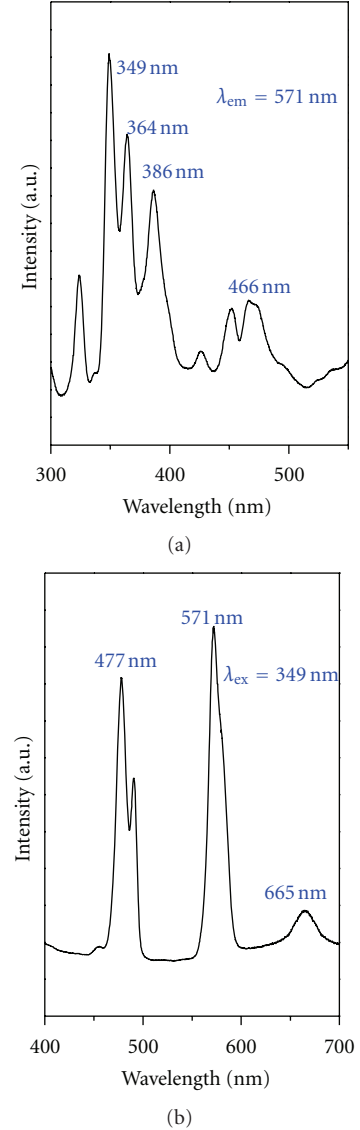


FIGURE 3: Excitation spectrum (a), ($\lambda_{\text{em}} = 571$ nm) and emission spectrum (b), ($\lambda_{\text{ex}} = 349$ nm) of Dy^{3+} in $(\text{Sr}_{0.99}, \text{Dy}_{0.01})_2\text{SiO}_4$.

Though the emission of $\text{Sr}_2\text{SiO}_4 : \text{Dy}$ also contained the peak at 665 nm, the luminescence enhancement of Mn^{2+} at ~ 650 nm further proved the energy transfer from Dy^{3+} to Mn^{2+} . The luminescence intensities of Mn^{2+} at 647 nm and Dy^{3+} at 571 nm asynchronously changed with their concentration variations shown in Figure 6 (only four concentration pairs with dramatic change are shown). The detailed change of the integrated intensities of 550–600 nm for Dy^{3+} and 635–700 nm for Mn^{2+} of all concentration-pairs is shown in Figure 7.

When the concentration of Dy^{3+} was fixed at 1.0 mol%, the emission intensity of Dy^{3+} gradually decreased with the increase of Mn^{2+} concentration (Figure 7(b)) and the emission intensity of Mn^{2+} firstly increased and then dropped down. The optimum concentration of Mn^{2+} for the maximum red-emission was 2.0 mol%. Therefore, the samples $(\text{Sr}_{0.98-x}, \text{Dy}_x)_2\text{SiO}_4 : \text{Mn}_{0.04}$ as a function of Dy^{3+} concentration were also synthesized to obtain the strong emissions

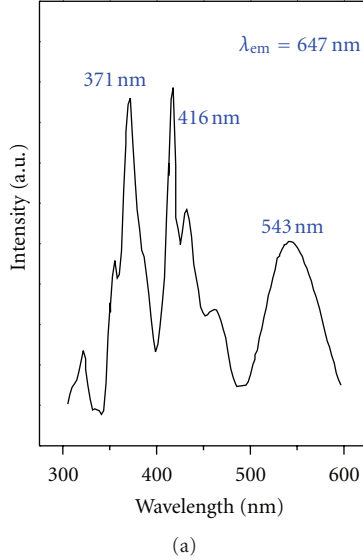


FIGURE 4: Excitation spectrum (a), ($\lambda_{\text{em}} = 647 \text{ nm}$) and emission spectrum (b), ($\lambda_{\text{ex}} = 416 \text{ nm}$) of Mn^{2+} in $(\text{Sr}_{0.98}, \text{Mn}_{0.02})_2\text{SiO}_4$.

of Dy^{3+} and Mn^{2+} simultaneously. The detailed emission change is shown in Figure 7(a). With the increase of the concentration of Dy^{3+} , the yellow emission intensity reached the maximum when the corresponding concentration of Dy^{3+} was 1.0 mol%. But when the red emission intensity of Mn^{2+} reached the maximum, the codoped concentration of Dy^{3+} was 2.0 mol%, and then the great decrease of the two emissions occurred due to the self-concentration quenching of Dy^{3+} ions. That is, the optimum concentration ranges of Dy^{3+} and Mn^{2+} to obtain the highest yellow and red emissions are 1.0~2.0 mol%. From the typical emission spectra of four concentration-pairs shown in Figure 6, it was noted that the peak location of red emission changed with the variation of the Dy/Mn concentrations. A red shift occurred from 651 nm to 659 nm with the increase of Mn concentration (b~d) and this may be due to the exchange interactions between Mn^{2+} ions [24].

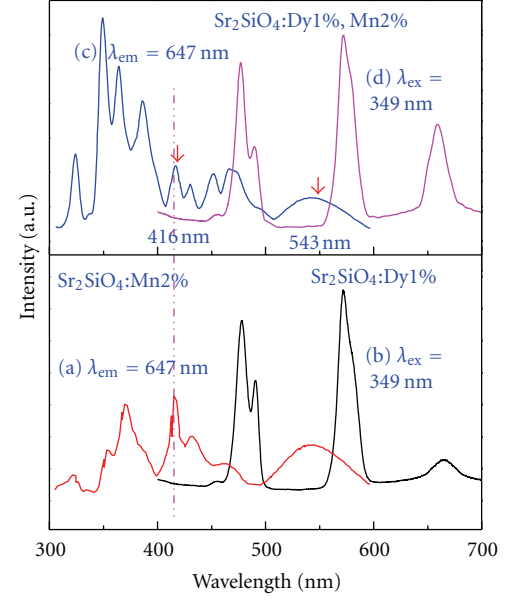


FIGURE 5: Excitation spectrum (a), ($\lambda_{\text{em}} = 647 \text{ nm}$) of Mn^{2+} in $(\text{Sr}_{0.98}, \text{Mn}_{0.02})_2\text{SiO}_4$ and emission spectrum (b), ($\lambda_{\text{ex}} = 349 \text{ nm}$) of Dy^{3+} in $(\text{Sr}_{0.99}, \text{Dy}_{0.01})_2\text{SiO}_4$. Excitation (c), ($\lambda_{\text{em}} = 647 \text{ nm}$) and emission (d), ($\lambda_{\text{ex}} = 349 \text{ nm}$) spectra of Mn^{2+} in $(\text{Sr}_{0.97}, \text{Mn}_{0.02}, \text{Dy}_{0.01})_2\text{SiO}_4$.

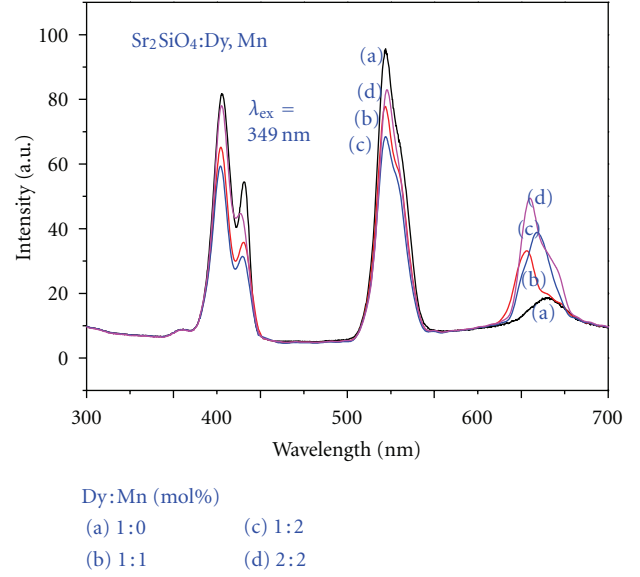


FIGURE 6: Emission spectra of $(\text{Sr}, \text{Dy}, \text{Mn})_2\text{SiO}_4$ with different concentration pairs of Dy and Mn ($\lambda_{\text{ex}} = 349 \text{ nm}$).

The CIE chromaticity coordinates of the four concentration-pair powders are shown in Figure 8. They were all in white light region. However, comparing with the point (a), points (b, c, and d) had the purer white color and their CIE coordinates were closer with the pure white point (0.330, 0.330; five stars). The optimized coordinates were (0.332, 0.326) with higher emission intensity when the codoping concentrations of Dy^{3+} and Mn^{2+} were 2.0 mol% and 2.0 mol%, respectively. That is, the red emission of

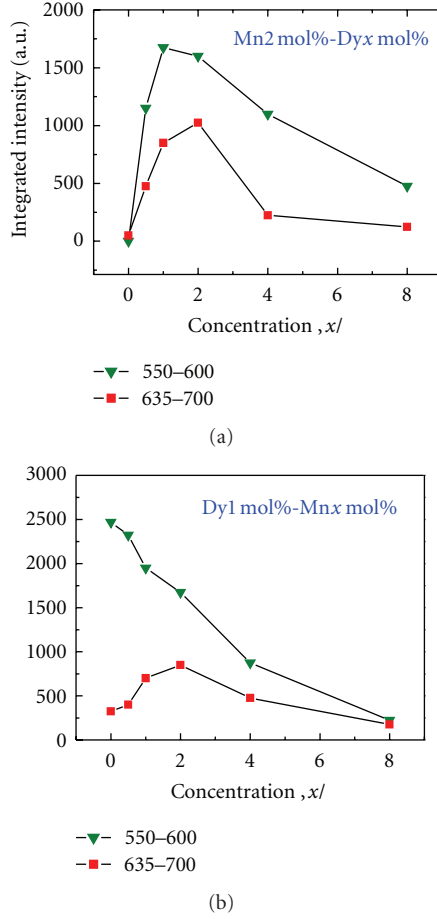


FIGURE 7: Variations of integrated intensity of 550–600 nm for Dy^{3+} and 635–700 nm for Mn^{2+} in $(\text{Sr}, \text{Dy}, \text{Mn})_2\text{SiO}_4$ ($\lambda_{\text{ex}} = 349 \text{ nm}$).

$\text{Sr}_2\text{SiO}_4 : \text{Dy}$ phosphor was effectively compensated by the codoping of Mn^{2+} ions, the concentration-optimizing of Dy/Mn , and the energy transfer from Dy^{3+} to Mn^{2+} .

3.3. Energy Transfer from Dy^{3+} to Mn^{2+} . Figure 9 shows the schematic diagram of energy transfer in $\text{Sr}_2\text{SiO}_4 : \text{Dy}, \text{Mn}$ powders. The excitation peaks of Mn^{2+} at 416 and 543 nm ($^6\text{A}_1(6\text{S}) \rightarrow ^4\text{T}_2(4\text{G})/ ^4\text{T}_1(4\text{G})$) were covered by the emission peaks of Dy^{3+} at 477 nm and 571 nm ($^4\text{F}_{9/2} \rightarrow ^4\text{H}_{15/2}/ ^6\text{H}_{13/2}$). This overlap indicates that the energy transfer mechanism is likely to be the radiative reabsorption or nonradiative cross relaxation. However, it could not be the radiative transfer because the oscillator strengths of $^6\text{A}_1(6\text{S}) \rightarrow ^4\text{T}_2(4\text{D})/ ^4\text{T}_1(4\text{G})$ are very weak and the resulted energy transfer will be much weaker. Therefore, the energy transfer is likely to be the non-radiative cross-relaxation (CR) between the $^4\text{F}_{9/2} \rightarrow ^4\text{H}_{15/2}, ^6\text{H}_{13/2}$ transitions of Dy^{3+} , and the $^6\text{A}_1(6\text{S}) \rightarrow ^4\text{T}_2(4\text{G}), ^4\text{T}_1(4\text{G})$ transitions of Mn^{2+} as shown in Figure 9.

In order to elucidate the type of the interaction involved in the energy transfer from the donor ions (Dy^{3+}) to the acceptor ions (Mn^{2+}), the luminescence intensities of Dy^{3+} and Mn^{2+} were integrated from the emission spectra

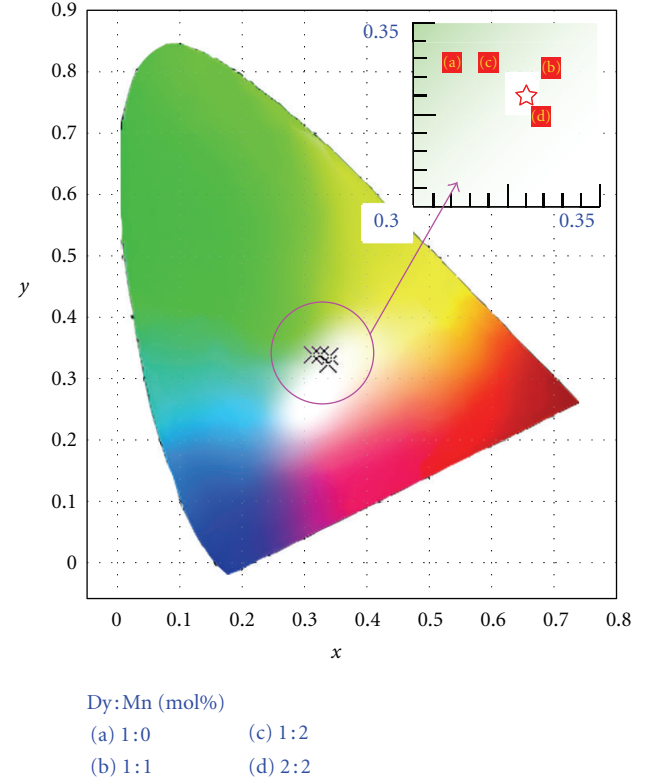


FIGURE 8: CIE chromaticity coordinates of $(\text{Sr}, \text{Dy}, \text{Mn})_2\text{SiO}_4$ with different concentration pairs ($\lambda_{\text{ex}} = 349 \text{ nm}$).

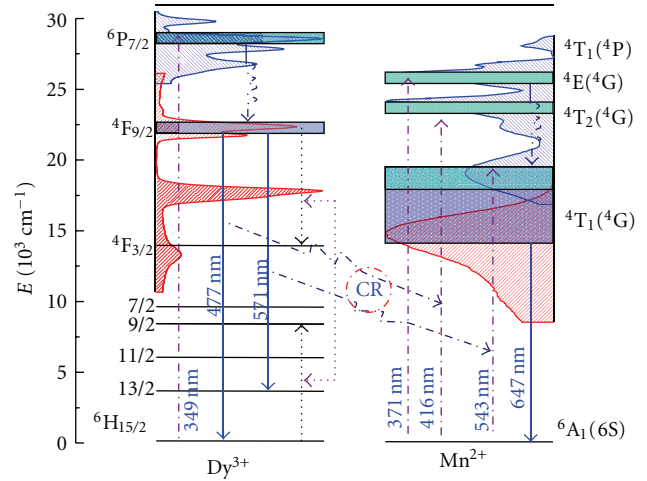


FIGURE 9: Energy transfer diagram of $\text{Dy}^{3+} \rightarrow \text{Mn}^{2+}$.

of Dy/Mn codoped powders according to the VanUitert's work [25–27]. The relationship between the luminescence intensity of the donor ions (Dy^{3+}) and the concentration of the acceptor ions (Mn^{2+}) satisfies the following formula [28]:

$$\frac{I}{I_0} = \left(1 + Ax^{\theta/3}\right)^{-1}, \quad (1)$$

I_0 and I are the luminescence intensity of donor ions (Dy^{3+}) without and with the appearance of acceptor ions (Mn^{2+}),

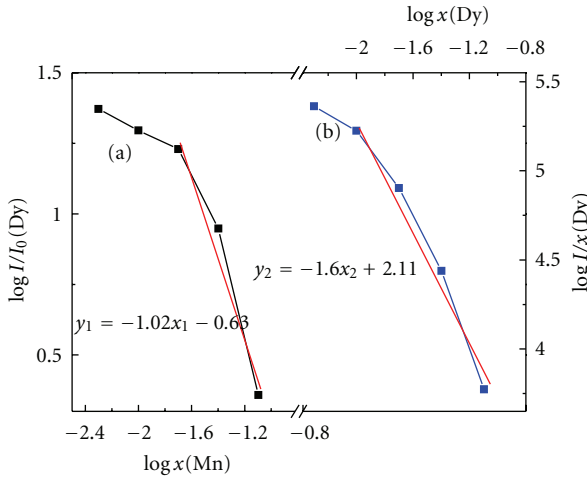


FIGURE 10: (a) $\log(I/I_0)$ of Dy^{3+} emission versus Mn^{2+} concentration in $(\text{Sr}_{0.99-x}, \text{Mn}_x)_2\text{SiO}_4 : \text{Dy}_{0.02}$; (b) $\log(I/x)$ of Dy^{3+} emission versus Dy^{3+} concentration in $(\text{Sr}_{0.98-x}, \text{Dy}_x)_2\text{SiO}_4 : \text{Mn}_{0.04}$.

respectively. A is a constant for one host. When the θ value is 3, 6, 8, and 10, the interaction type is the exchange interaction, dipoles-dipoles (d-d), dipoles-quadrupoles (d-q), and quadrupoles-quadrupoles (q-q), respectively. The relation curve between $\log(I/I_0(\text{Dy}))$ and $\log(x(\text{Mn}))$ is plotted in Figure 10(a). According to the slope of the fitted line y_1 for the curve (a), $\theta/3$ is 1.02 and θ is 3.06. As stated in VanUitert's theory [25], the energy transfer from Dy^{3+} to Mn^{2+} is realized by the exchange interaction.

In the meantime, in Huang's theory [28] for the interaction type among the donor ions (Dy^{3+}), the relationship between the luminescent intensity (I) and the concentration of activators (C) should be expressed as

$$I \propto a^{1-s/d} \Gamma \left(1 + \frac{s}{d} \right), \quad (2)$$

where $a = CT(1 - d/s)[X_0(1 + A)/\gamma]^{d/s}$, γ is the transition probability of the donor ions (Dy^{3+}), d is the sample dimension ($d = 3$), Γ is a concentration-independent function, and C is the concentration of the donor ions (Dy^{3+}). s is the electric multipoles index. When s value is 3, 6, 8 and 10, the interaction type is also exchange interaction, d-d, d-q, and q-q, respectively. After a mathematical operating,

$$I \propto KC^{1-s/d}, \quad (3)$$

K is a concentration-independent constant. Thus, the value of s could be obtained by the relation curve of $\log(I/C_{\text{Dy}}) \sim \log(C_{\text{Dy}})$ plotted in Figure 10(b). According to the slope of the fitted line y_2 for the curve (b), s is approximately equal to 4.80, which means that the d-d interaction ($s = 6$) as well as the exchange interaction ($s = 3$) are involved in the self-concentration quenching of the ${}^4\text{F}_{9/2} \rightarrow {}^6\text{H}_{13/2}$ transition of Dy^{3+} (571 nm). On the basis of a simple linear-algebraic calculation for the s value ($3m + 6(1 - m) = 4.80$), where the m value is the fraction of the exchange interaction, about 40% of the non-radiative energy transfer occurs via

the exchange interaction. Therefore, the d-d interaction is involved in a major way in the luminescence quenching of $\text{Sr}_2\text{SiO}_4 : \text{Dy}^{3+}, \text{Mn}^{2+}$ phosphor.

4. Conclusions

In this paper, Mn^{2+} ions codoped $\text{Sr}_2\text{SiO}_4 : \text{Dy}^{3+}$ phosphors were successfully prepared by the solid-state reaction method using NH_4Cl as the flux. All Mn/Dy codoped powders were $\alpha'\text{-Sr}_2\text{SiO}_4$ with the slight shift of the diffraction peaks to higher angle with the increase of the substitution concentrations of Mn/Dy. The codoping concentration range of Mn^{2+} is ≤ 4.0 mol% to keep the structure undamaged. The broad red emission of Mn^{2+} centered at ~ 650 nm was observed from $\text{Sr}_2\text{SiO}_4 : \text{Mn}$, Dy powders, which effectively compensated the red emission of $\text{Sr}_2\text{SiO}_4 : \text{Dy}^{3+}$ phosphor. The CIE chromaticity coordinates dramatically changed from (0.310, 0.340) to (0.332, 0.326) due to the red enhancement via the energy transfer from Dy^{3+} to Mn^{2+} . This energy transfer is realized through the exchange interaction. But the d-d interaction plays a major role in the luminescence quenching of $\text{Sr}_2\text{SiO}_4 : \text{Dy}^{3+}, \text{Mn}^{2+}$ phosphor. The concentration optimized $(\text{Sr}_{0.96}, \text{Mn}_{0.02}, \text{Dy}_{0.02})_2\text{SiO}_4$ phosphor with almost pure white emission has great potential to act as a single-matrix white phosphor for white LEDs.

Acknowledgments

The authors acknowledge the generous financial supports from the Natural Science Foundation of Jiangsu Province (BK2007724), National Natural Science Foundation of China (51202111), Priority Academic Program Development of Jiangsu Higher Education Institutions (PAPD), and Research and Innovation Program for College Graduates of Jiangsu Province (CXZZ12_0410).

References

- [1] R. V. Steele, "The story of a new light source," *Nature Photonics*, vol. 1, no. 1, pp. 25–26, 2007.
- [2] Y. Narukawa, J. Narita, T. Sakamoto et al., "Recent progress of high efficiency white LEDs," *Physica Status Solidi A*, vol. 204, no. 6, pp. 2087–2093, 2007.
- [3] J. S. Kim, P. E. Jeon, Y. H. Park et al., "White-light generation through ultraviolet-emitting diode and white-emitting phosphor," *Applied Physics Letters*, vol. 85, no. 17, pp. 3696–3698, 2004.
- [4] F. B. Wu, D. W. Zhang, S. Z. Shang, Y. M. Zhu, S. L. Zhuang, and J. Xu, "Developing quantum dot phosphor-based light-emitting diodes for aviation lighting applications," *Journal of Nanomaterials*, vol. 2012, Article ID 629157, 5 pages, 2012.
- [5] M. A. Greenwood, "Phosphor-coated LED converts blue light to white," *Photonics Spectra*, vol. 42, no. 6, article 100, 2008.
- [6] G. Liu, S. Zhang, X. Dong, and J. Wang, "Solvothermal synthesis of $\text{Gd}_2\text{O}_3 : \text{Eu}^{3+}$ luminescent nanowires," *Journal of Nanomaterials*, vol. 2010, Article ID 365079, 5 pages, 2010.
- [7] C. S. Ciobanu, S. L. Iconaru, F. Massuyeau, L. V. Constantin, A. Costescu, and D. Predoi, "Synthesis, structure, and luminescent properties of europium-doped hydroxyapatite

- nanocrystalline powders," *Journal of Nanomaterials*, vol. 2012, Article ID 942801, 9 pages, 2012.
- [8] C. K. Chang and T. M. Chen, "Sr₃B₂O₆: Ce³⁺, Eu²⁺: a potential single-phased white-emitting borate phosphor for ultraviolet light-emitting diodes," *Applied Physics Letters*, vol. 91, no. 8, Article ID 081902, 3 pages, 2007.
- [9] J. S. Kim, P. E. Jeonny, J. C. Choi, H. L. Park, S. I. Mho, and G. C. Kim, "Warm-white-light emitting diode utilizing a single-phase full-color Ba₃MgSi₂O₈:Eu²⁺, Mn²⁺ phosphor," *Applied Physics Letters*, vol. 84, no. 15, pp. 2931–2933, 2004.
- [10] Z. L. Wang, K. W. Cheah, H. L. Tam, and M. L. Gong, "Near-ultraviolet light excited deep blue-emitting phosphor for solid-state lighting," *Journal of Alloys and Compounds*, vol. 482, no. 1-2, pp. 437–439, 2009.
- [11] S. G. Johnson and J. A. Simmons, "Materials for solid state lighting," in *Proceedings of the Materials and Devices for Optoelectronics and Microphotronics*, pp. 53–64, San Francisco, Calif, USA, April 2002.
- [12] A. A. Setlur, J. J. Shiang, and U. Happék, "Eu²⁺–Mn²⁺ phosphor saturation in 5 mm light emitting diode lamps," *Applied Physics Letters*, vol. 92, no. 8, Article ID 081104, 2008.
- [13] S. H. Lee, J. H. Park, S. M. Son, J. S. Kim, and H. L. Park, "White-light-emitting phosphor: CaMgSi₂O₆:Eu²⁺, Mn²⁺ and its related properties with blending," *Applied Physics Letters*, vol. 89, no. 22, Article ID 221916, 3 pages, 2006.
- [14] E. Cavalli, M. Bettinelli, A. Belletti, and A. Speghini, "Optical spectra of yttrium phosphate and yttrium vanadate single crystals activated with Dy³⁺," *Journal of Alloys and Compounds*, vol. 341, no. 1-2, pp. 107–110, 2002.
- [15] G. S. Raghuvanshi, H. D. Bist, and H. C. Kandpal, "Luminescence characteristics of Dy³⁺ in different host matrices," *Journal of Physics and Chemistry of Solids*, vol. 43, no. 8, pp. 781–783, 1982.
- [16] L. Zhang, Z. Lu, H. Yang, P. Han, N. Xu, and Q. Zhang, "Preparation of Dy³⁺-activated strontium orthosilicate (Sr₂SiO₄:Dy³⁺) phosphors and its photoluminescent properties," *Journal of Alloys and Compounds*, vol. 512, no. 1, pp. 5–11, 2012.
- [17] L. Zhang, P. Han, Z. Lu et al., "Enhanced luminescence of Sr₂SiO₄:Dy³⁺ by sensitization (Ce³⁺/Bi³⁺) and its composition-induced phase transition," *Journal of Alloys and Compounds*, vol. 541, pp. 54–59, 2012.
- [18] L. Zhang, Z. Lu, P. Han, and Q. Zhang, "Action mechanism of NH₄Cl flux used to synthesize Sr₂SiO₄:Dy³⁺ phosphor by solid-state reaction method," *Journal of The American Ceramic Society*. In press.
- [19] T. Moon, G. Y. Hong, H. C. Lee et al., "Effects of Eu²⁺ co-doping on vuv photoluminescence properties of BaMgAl₁₀O₁₇: Mn²⁺ phosphors for plasma display panels," *Electrochemical and Solid-State Letters*, vol. 12, no. 7, pp. J61–J63, 2009.
- [20] L. Lin, M. Yin, C. Shi, and W. Zhang, "Luminescence properties of a new red long-lasting phosphor: Mg₂SiO₄:Dy³⁺, Mn²⁺," *Journal of Alloys and Compounds*, vol. 455, no. 1-2, pp. 327–330, 2008.
- [21] S. L. Yuan, Y. X. Yang, X. H. Zhang et al., "Eu²⁺ and Mn²⁺ codoped Ba₂Mg(BO₃)₂—new red phosphor for white LEDs," *Optics Letters*, vol. 33, no. 23, pp. 2865–2867, 2008.
- [22] J. S. Kim, K. T. Lim, Y. S. Jeong, P. E. Jeon, J. C. Choi, and H. L. Park, "Full-color Ba₃MgSi₂O₈:Eu²⁺, Mn²⁺ phosphors for white-light-emitting diodes," *Solid State Communications*, vol. 135, no. 1-2, pp. 21–24, 2005.
- [23] Q. Zhang, *Fundamentals of Inorganic Materials Science*, East China University of Science and Technology Press, Shanghai, China, 2006.
- [24] C. R. Ronda and T. Amrein, "Evidence for exchange-induced luminescence in Zn₂SiO₄: Mn," *Journal of Luminescence*, vol. 69, no. 5-6, pp. 245–248, 1996.
- [25] L. G. van Uitert and L. F. Johnson, "Energy transfer between rare-earth ions," *The Journal of Chemical Physics*, vol. 44, no. 9, pp. 3514–3522, 1966.
- [26] L. G. van Uitert, E. F. Dearborn, and H. M. Marcos, "Mechanisms of energy transfer involving trivalent Tb and Eu," *Applied Physics Letters*, vol. 9, no. 7, pp. 255–257, 1966.
- [27] L. G. V. Utter, "Characterization of energy transfer interactions between rare earth ions," *Journal of the Electrochemical Society*, vol. 114, no. 10, pp. 1048–1053, 1967.
- [28] S. Huang and L. Lou, "Concentration dependence of sensitizer fluorescence intensity in energy transfer," *Chinese Journal of Luminescence*, vol. 11, no. 1, pp. 1–7, 1990.